Probing quantum and classical noise in nano circuits

ARSALAN POURKABIRIAN

Probing quantum and classical noise in nano circuits
ARSALAN POURKABIRIAN
Department of Microtechnology and Nanoscience
Chalmers University of Technology, 2014

Abstract

This thesis presents measurements of classical and quantum noise in nano circuits. The first part of the thesis, covers extensive measurements on charge noise sources. Low-frequency charge noise with the power spectrum close to $1/f$ (where f is the frequency) has been observed in a variety of systems. Despite the large theoretical and experimental efforts during the past three decades, the origin of this noise is still unknown. One of the best platforms to study this noise is the single electron transistor (SET) which is extremely sensitive to charge. We have exploited this unique charge sensitivity to probe the charge noise sources.

We have measured the temperature and the bias dependence of the charge noise and concluded that the two-level fluctuators (TLFs) which cause the charge noise have a temperature which is closer to the temperature of the electrons on the SET rather than to the temperature of the phonos underneath the SET. This suggests that most probably the charge noise sources are in the vicinity of the SET and can thermalize with SET electrons through quantum tunneling which limits their distribution to within a few nanometers around the SET.

In another set of measurements, we have probed the TLFs when they are pushed out of equilibrium by an external electric field. The relaxation process of the TLFs causes a charge drift which we have measured using a SET over four decades of time. We found that this drift is logarithmic in time and by comparing it to theory we could extract the density of TLFs. Studying how the drift depends on temperature and electric field, we can also conclude that the switching of the TLFs is due to quantum tunneling and not due to thermal activation.

The second part of the thesis covers experiments related to vacuum fluctuations. Vacuum fluctuations are one of the most interesting predictions of the quantum mechanics. We have demonstrated the first observation of the dynamical Casimir effect, which is generation of real photons out of the vacuum by modulation of a mirror at relativistic speeds. We show broad band generation of photons and demonstrate two-mode squeezing of this radiation. In another experiment, we have measured the strength of these vacuum fluctuations by using an artificial atom in front of a mirror as our quantum probe. In the last part of the thesis, we present preliminary results for characterization of the system consisting of two artificial atoms in front of a mirror, a system which can potentially exploited for studying the interaction of artificial atoms through exchange of photons.

Keywords: charge noise, two-level fluctuator, SET, SQUID, transmon, vacuum fluctuations, circuit-QED, dynamical Casimir effect, artificial atom.

iv

List of Publications

This thesis is based on the work contained in the following papers:

I: Thermal properties of charge noise sources.
M.V. Gustafsson*, A. Pourkabirian*, G. Johansson, J. Clarke and P. Delsing.
Physical Review B **88**, 245410, 2013.
(* Joint first authorship)

II: Non-equilibrium probing of two-level charge fluctuators using the step response of a single electron transistor.
A. Pourkabirian, M.V. Gustafsson, G. Johansson, J. Clarke and P. Delsing.
In review (arXiv:1408.6496).

Non-equilibrium probing of two-level charge fluctuators using the step response of a single electron transistor: Supplemental Material.

III: Observation of the dynamical Casimir effect in a superconducting circuit.
C.M. Wilson, G. Johansson, A. Pourkabirian, M. Simoen, J.R. Johansson, T. Duty, F. Nori and P. Delsing.
Nature **479**, 376, 2011.

Observation of the dynamical Casimir effect in a superconducting circuit: Supplementary Information.

IV: Probing the quantum vacuum with an atom in front of a mirror.
I.-C Hoi, A.F. Kockum, L. Tornberg, A. Pourkabirian, G. Johansson, P. Delsing and C.M. Wilson.
In review (arXiv:1410.8840).

V: Scattering properties of two artificial atoms in front of a mirror.
A. Pourkabirian, S.R. Sathyamoorthy, G. Johansson, C.M. Wilson and P. Delsing.
Manuscript.

Contents

Chapter 1

Introduction

Robert Millikan performed the first measurement of the elementary electronic charge, e, in 1909 in his famous oil drop experiment and showed that electrical charge is quantized [1]. He received the Nobel prize in physics 14 years later for that but it took almost half a century before the single electron effects were observed in granular films [2, 3, 4, 5, 6]. In the 1980's the first electrical circuits which could deal with individual electrons were demonstrated [7]. Today, the electrical systems in which the discrete nature of the electrons is studied are known as the single electronics [8, 9, 10].

The working principle of these circuits are based on *quantum tunneling* through a very thin insulating layer sandwiched between two conductors, a structure which is known as a *tunnel junction* [11, 12].

Consider a very small metallic granule which is isolated from the environment by a tunnel junction. Electrons can only move in and out of the granule by tunneling through this junction. If the granule is uncharged in the beginning and then an electron tunnels in, it charges the granule with negative charge, $-e$. Now, if another electron wants to tunnel in, it should overcome the repelling Coulomb force between the negative electron charge and the negatively charged granule. If the granule is small enough, this repelling Coulomb force can be large so that, for the right circumstances, it prevents the extra electron to tunnel in. This effect is known as the *Coulomb blockade* and allows us to isolate exactly one extra electron on the metallic granule. If one compares electrical current, the flow of electrons through a conductor, to the water flowing in a pipe, then the tunnel junction acts as a dripping tap, letting the electrons to pass (tunnel) one at a time [9]. Today, exploiting the Coulomb blockade, more complex circuits and devices have been developed which allow us to control and manipulate the individual electrons.

Single electron devices, due to their working principle, are very charge sensitive. They detect charges as small as a fraction of an electron charge. This unique charge sensitivity, has led to several potential applications for these devices as electrometers. In practice, however, there is a problem to exploit these devices as reliable electrometers. They not only detect the charge changes in the system under study,

but also any other charge motion or charge reconfiguration in their vicinity will affect their output. From the early days of single electronics, many efforts have been made to improve the fabrication and measurement techniques in order to overcome this problem and isolate these devices from the external noise sources [13].

Even when one uses advanced measurement techniques and instruments to eliminate the external noise [14], there are still intrinsic charge movements at the atomic and molecular levels which disturb the performance of these devices. One of this noise processes is the low frequency charge noise with a power spectrum close to $1/f$, where f is the frequency. This type of noise has been observed in the variety of systems and has been studied for many decades, but its exact origin is still an open question [15].

The general belief is that, an ensemble of fluctuating charged particles in the vicinity of the devices cause the $1/f$ noise (Figure 1.1). Each of these charged particles fluctuates between two neighboring positions and are hence known as two-level fluctuators (TLFs). In principle, these fluctuations can be thermally activated (red arrows in Figure 1.1) or can be due to the quantum tunneling (green arrows in Figure 1.1).

In the first part of the thesis (experiments in Chapter 4, paper I-II), we discuss the experiments we have performed to probe these TLFs under different conditions. Using single electron transistors [16], we probe the ensembles of TLFs both when they are in equilibrium state and also when they are pushed far out of equilibrium by a strong external electric field. We draw several new conclusions about their microscopic description and their activation mechanisms.

In the second part of the thesis (experiments in Chapter 5, paper III-V), we study the noise processes which originate from a more fundamental phenomenon, namely *vacuum fluctuations*. Quantum fluctuations of the vacuum, are one of the surprising predictions of quantum mechanics: energetic particles (like photons) can temporarily appear out of the vacuum and then disappear. This briefly violates energy conservation as allowed by the uncertainty principle [11]. These fluctuations of the vacuum are referred to as quantum fluctuations or vacuum fluctuations and the particles which come and go are called *virtual particles*. For many years, the existence of these virtual particles was mainly considered as a theoretical curiosity.

Later, experiments showed that indeed these vacuum fluctuations have several real, measurable impacts. For example, spontaneous emission of atoms are governed by the vacuum fluctuations. It was also predicted that moving a perfect conducting plate (a mirror) in the vacuum at relativistic speeds, can push these virtual particles into existence, before they get annihilated and disappear [17, 18, 19]. This effect is known as the dynamical Casimir effect (DCE) [20]. In Chapter 5, we explain the first experimental observation of the DCE where we modulated the boundary condition of an electrical circuit instead of moving a real mirror. We observed microwave photons which were generated out of vacuum.

In recent years along with advances in quantum information experiments, several types of *quantum bits* (qubits) have been designed and realized as building blocks of the future quantum computers. A qubit is the quantum analogue of the classical bit,
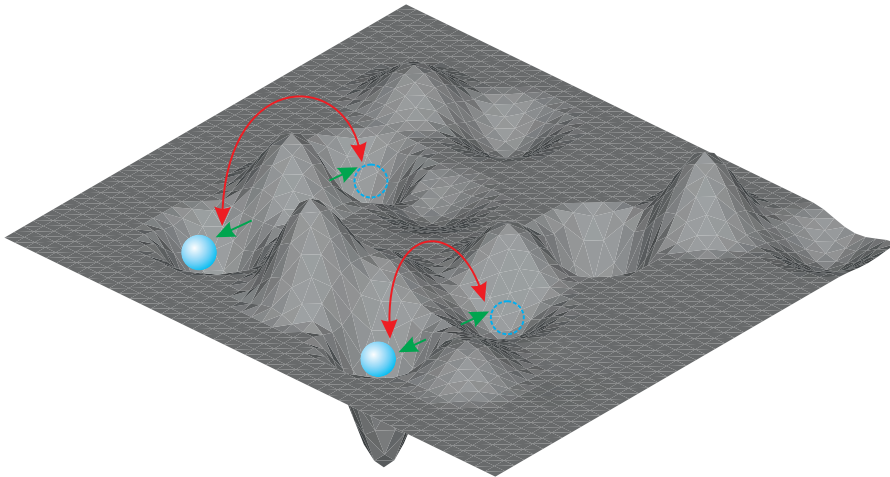
Figure 1.1: Schematic illustration of two-level fluctuators. Charged particles (cyan) can fluctuate between two different positions either by quantum tunneling (green arrows) or due to their thermal energy (red arrows).

a quantum two-level system which not only, similar to the classical bits, can be in one state or the other but also, can be in the quantum superposition of the two states [21].

One of the major obstacles to perform logical gates with solid state qubits is that they *decohere* relatively fast, *i.e.* they loose information to the environment which they are coupled to [22, 23]. One of the reasons for this process is the interactions of the qubits with vacuum fluctuations. As described by Lambrecht [24], preserving qubits in their excited states is like holding a sharp pencil upright on the end of your finger, any small perturbation will make the pencil fall down to a more stable equilibrium state. For qubits, similarly, interaction with vacuum fluctuations cause them to relax to their ground state.

In Chapter 5 we present another experiment, where we have probed the strength of the vacuum fluctuations by measuring the life time of the qubit. Placing a qubit at a distance from a mirror, we demonstrate that we can shape the vacuum fluctuations by creating regions in space where they are suppressed. In the most recent experiment we also probe the properties of two qubits in front of a mirror.

The outline of this thesis is as follows: Chapter 2 describes the theoretical background related to the experiments. That chapter covers a short introduction to single electronics, single electron transistors (SETs) and different noise processes in charge-sensitive devices. Later in Section 2.4, we discuss two-level charge fluctuators (TLFs) and how they can affect these devices. We also investigate the collective effects when an ensemble of these TLFs are active in the vicinity of an SET. Specifically, we derive equations for the response of this ensemble when it is pushed out of equilibrium by an external electric field. In Section 2.5, we explain the building

blocks of the circuit quantum electrodynamic (circuit QED) experiments and discuss vacuum fluctuations. In Chapter 3, we briefly describe the experimental techniques in fabrication of the samples and the working principle of our cryogenic and measurement systems. In Chapter 4, we discuss the experiments on probing the TLFs. The results of these experiments are presented in paper I and paper II. Finally, in Chapter 5 we describe the experiments on probing the vacuum fluctuations and their interaction with qubits. We explain the observation of the dynamical Casimir effect (paper III), and how the interaction of a qubit with vacuum fluctuations are modified by a mirror (paper IV). Finally, we describe characterization of a system which consists of two qubits in front of a mirror (paper V).

Chapter 2

Theoretical Background

In this Chapter the background theory related to the experimental results in Chapter 4 and Chapter 5 will be discussed. The first part of this Chapter from Section 2.1 to Section 2.4 will be a brief introduction to the field of single electronics, the working principle and noise mechanisms of single electron transistors (SET), and finally the description of different theories regarding noise sources in charge-sensitive devices. In the second part of this Chapter from Section 2.5 to Section 2.7, we first explain the building blocks of experiments in circuit quantum electrodynamic (circuit QED) and later we discuss how we use the circuit QED experiments to probe the vacuum fluctuations.

2.1   Single electronics

Electrical current is the flow of electrons in a conductor. Since all electrons have equal amount of charge (e, the elementary charge) one may expect that the electrical current should be quantized in multiples of the elementary charge, but why can we measure any arbitrary amount of current in our circuits?

The reason is that conduction electrons in a metal form an extended wave function which is not localized [8]. Displacement of this "electron cloud" causes conductivity and this displacement can be done by any arbitrarily small amount.

It is interesting to study circuits which pass electrons one by one [7, 8, 9]. These circuits not only enable us to study basic physics and quantum mechanics on a chip but also have a great potential to be used in technology.

The key component to realize such circuits is a sufficiently small tunnel junction, which is a device consists of a thin insulating layer ($\sim$1 nm) sandwiched between two conductors. Quantum mechanics predict that electrons can go through such a thin barrier by quantum tunneling [11, 12].

2.2   Single electron box (SEB)

Figure 2.1(a) shows the simplest device in the family of single electronics, the single electron box (SEB). It consists of a metallic island which is connected to an electrode via a tunnel junction with capacitance of, C_J, and a tunnel resistance of, R_J. It is also capacitively coupled to a gate voltage source, V_g, via capacitance C_g.

This device is controlled by the gate voltage. When $V_g = 0$, the system is neutral *i.e.* there are no excess electrons on the island. If we start to increase V_g, it induces charge $Q_g = C_g V_g \equiv n_g e$ on the island where n_g is the the normalized gate charge. To compensate this charge, electrons tunnel from the electrode (reservoir) to the island. After tunneling n electrons onto the island the net charge of the island changes from neutral to $Q_g - ne$. This corresponds to electrostatic energy of

$$E(n, n_g) = \frac{(Q_g - ne)^2}{2C_\Sigma} = E_C \, (n - n_g)^2 \tag{2.1}$$

where $C_\Sigma = C_g + C_J$ is the total capacitance and $E_C = e^2/2C_\Sigma$ is the *charging energy* of the island. To add an electron to the island one has to supply an energy which is larger than $E(n, n_g)$. If the capacitances are small enough, this energy can be so large that it prevents more electrons from tunneling. This phenomenon is known as the *Coulomb blockade*.

In order to observe the Coulomb blockade, the charging energy should be much larger than the thermal energy, $E_C \gg k_B T$ (k_B is the Boltzmann constant and T is the temperature), otherwise thermal fluctuations will smear the effect of the Coulomb blockade. Considering the tunnel junction as a simple parallel plate capacitor with dimensions of about 100 nm and dielectric thickness of ~ 2 nm will result in $C_J \approx 10^{-15}$ F and corresponding E_C of ~ 1 K. This limits the operation of devices based on Coulomb blockade to sub-Kelvin temperatures, unless the junctions are made even smaller.

Also the tunnel junctions should be resistive enough to localize the charge. In other words, on the time scale of $\tau \sim R_J C_J$, the uncertainty of energy in the junction, $\delta\epsilon$, due to Heisenberg's uncertainty relation for energy-time, should be much smaller than the charging energy, $\delta\epsilon \approx \hbar/\delta\tau \ll E_C$, which will result in a condition on the resistance $R_J > R_K = h/e^2 \sim 25$ kΩ. In practice, to observe the Coulomb blockade clearly, the resistance of each junction must be several times higher than this limit.

There exist many different devices which exploit Coulomb blockade as their working principle such as single electron transistor (SET) [16], electron pumps [25], quantum dots [26] and many others. Although these devices help us to have control over motion of individual electrons, their applications have been limited mainly to research and they have not been used in industrial and commercial applications yet.

One obvious problem, as mentioned before, is their operation temperature. To observe Coulomb blockade in higher temperatures one needs to fabricate devices with very high charging energy (very small capacitors). We can overcome this problem by using advanced fabrication techniques which enable us to make very small
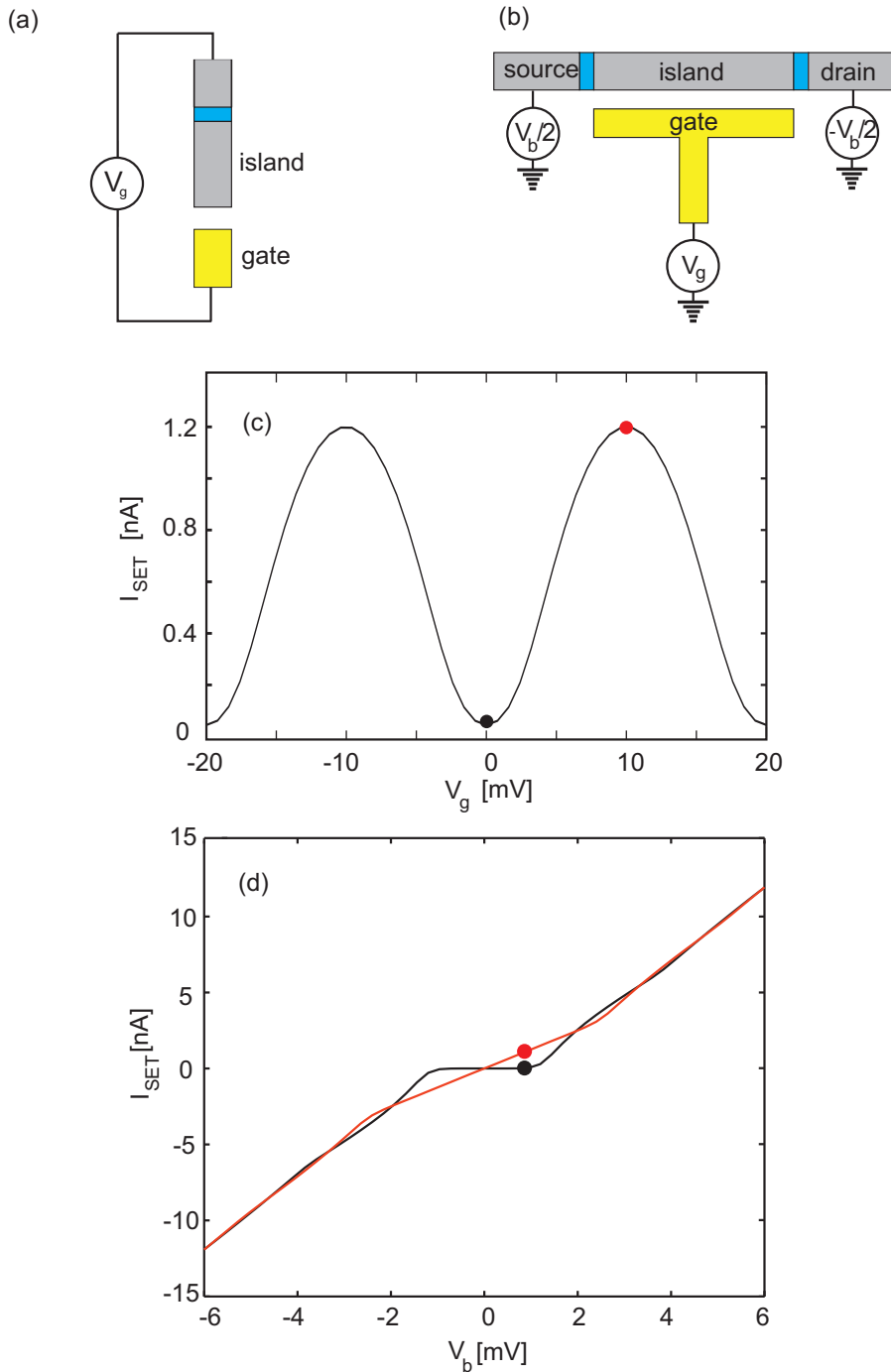
Figure 2.1: Single electronic devices: (a) Schematic of a single electron box (SEB). (b) Schematic of a single electron transistor (SET), where source and drain are biased symmetrically. The blue rectangles represents the tunnel junctions and the yellow electrode is the gate. (c) The transfer function: I_{SET} vs. V_g is periodic with period of e/C_g. The green and the red dot represent the closed and open state of the SET, respectively. (d) I_{SET} vs. V_b for open state (red) and closed state (black) of the SET.

devices. Several groups have already reported single electron devices working in higher and even room temperature [27]. The other problem to exploit such circuits is charge noise. Charge noise, as will be discussed later, limits the functionality of these devices.

2.3   Single electron transistor (SET)

One of the most studied devices in the field of single electronics is the single electron transistor (SET) [16]. A SET consists of three metallic electrodes; source, drain and gate. Two tunnel junctions connected in series between source and drain form an island. The gate electrode is capacitively coupled to this island [Figure 2.1(b)].

If we apply a bias voltage, V_b, to the SET electrodes, electrons will flow from source to drain by tunneling through the tunnel junctions. To travel from source to drain, electrons should overcome the charging energy of the island which can be large considering the small size of the junctions and island. The charging energy, similar to the SEB, is $E_C = e^2/2C_\Sigma$, where C_Σ is the total capacitance of the island to the environment including the gate capacitance, C_g, the sum of junction capacitance, $C_{J1} + C_{J2}$, and any other stray capacitance, C_0, which are usually negligible.

If a voltage V_g is applied to the gate electrode of the SET, it induces charge $Q_g = C_g V_g$ on the island. Then, the electrostatic energy of the island is given by Equation 2.1. By tuning V_g one can tune n_g and consequently $E(n, n_g)$.

The special case where $n_g = n + 0.5$, is called the degeneracy point. In this case, the island electrostatic energy for n and $n + 1$ extra electrons on the island is equal. This allows electron to tunnel into the island through one junction ($n \longrightarrow n + 1$) and then tunnels out (assuming a SET with symmetric junctions) through the other junction ($n + 1 \longrightarrow n$), causing a net flow of current through the SET even at very low bias voltage. By changing V_g, so that the above condition is satisfied (for any integer n) there will be a current, I_{SET}, through the device (open state) and otherwise when tunneling is not energetically favorable, the device is in Coulomb blockade state and no current will flow (closed state)[Figure 2.1(b)]. This causes a periodic I_{SET} as a function of V_g with period of e/C_g which is referred to as the charge-transfer function or simply the transfer function [Figure 2.1(c)].

A very small change in the island charge induced by the gate (or as we show in the next section, by any other source) will drastically change the current passing through the SET. This makes the SET a very charge sensitive device and indeed SETs are the most charge sensitive electrometers [28, 29].

If the bias voltage between source and drain is large enough, electrons can gain enough energy to overcome the Coulomb blockade by transferring from source to drain [Figure 2.1(b)]. In order to operate the device in a Coulomb blockade-sensitive region, the bias voltage should be lower than a threshold value, $V_{th} = E_C/e = e/2C_\Sigma$. Well above this value, the current will flow through the device according to Ohm's law, independent of V_g.

2.4 Noise in SETs

2.4.1 Random fluctuations and noise

The outcome of any electrical measurement is a signal together with some additional noise. Although the information regarding the outcome of the experiment is carried in the measured signal, measurements on the noise can also reveal useful information. Noise studies can give information regarding the noise sources, their location and their dynamics. Electrical noise is often a stochastic random process. This means that we can not predict noise as a function of time but we can study the noise statistics.

The mathematical tool to study to what extent a system is deterministic, is called the auto-correlation function. If a variable $x(t)$ changes with time randomly and generates noise, the auto-correlation function as a function of separation time, τ, indicates how much the value of x at time $t + \tau$ is related to value of x at time t. It is defined as

$$r_x(\tau) = \lim_{T \to \infty} \frac{1}{T} \int_{-T/2}^{T/2} x(t)x(t + \tau)dt. \tag{2.2}$$

In experiments, noise is measured by spectrum analyzers and reported as a power spectral density, S_x, (noise power per unit of bandwidth).

The Wiener-Khinchin theorem states that the power spectral density and the auto-correlation function are related to each other through the Fourier transform [30]:

$$S_x(\omega) = \int_0^\infty r_x(\tau)\exp(-i\omega\tau)d\tau, \tag{2.3}$$

and

$$r_x(\tau) = \frac{1}{2\pi} \int_0^\infty S_x(\omega)\exp(i\omega\tau)d\omega. \tag{2.4}$$

where ω is the angular frequency. There are many random processes which cause noise in electrical circuit measurements. These noise process can either be intrinsic or have an external source. The intrinsic noises in electrical circuits are thermal noise, shot noise and low-frequency charge noise.

2.4.2 Thermal noise

Thermal noise or Johnson-Nyquist noise are the thermal fluctuations of electrons in the circuit [31, 32]. The thermal motion of electrons leads to small fluctuations and according to the fluctuation-dissipation theorem, these fluctuations cause noise [32]. At low frequency where $f < k_B T/h$ (h is the Planck constant), the power spectral density of this noise is given by $4k_B T R$ where T is the temperature and R is the resistance.

This noise is white *i.e.* it is not frequency dependent and since it scales linearly with the temperature, for cryogenic measurements it is very small.
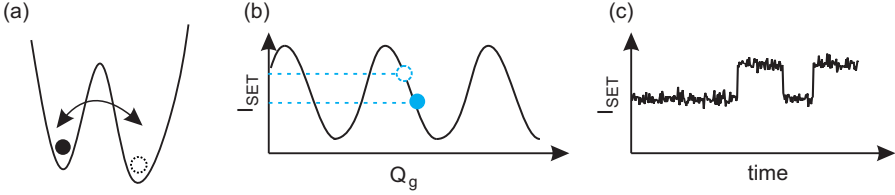
Figure 2.2: Two-level fluctuator (TLF) in the vicinity of the SET cause random telegraph noise (a) Schematic of a TLF: a charged particle fluctuates between two nearby positions. (b) Depending on its position, a TLF induce different charges on the SET island and consequently different currents pass the device. (c) Random telegraph noise is the signature of the TLFs in the vicinity of charge-sensitive devices.

2.4.3   Shot noise

The ultimate charge sensitivity limit of any device which pass electrical current is set by shot noise. Shot noise is the current fluctuations due to discreteness of charge carriers, *i.e.* electrons. If the tunneling events in the SET are uncorrelated (statistically independent) they follow Poisson statistics. In this case, the frequency-independent power spectrum of this noise is given by the Schottky formula [33]

$$S_{shot}(f) = 2\,e\,\langle I \rangle \tag{2.5}$$

where $\langle I \rangle$ is the average current through the device. Shot noise can be the limiting factor for the sensitivity of single electron devices, especially when they operate at higher frequencies like the radio-frequency SET (rf-SET) [34, 35].

Extensive measurements of shot noise in aluminium rf-SETs and devices based on nanowires have been performed previously in our group [36, 37]. The performance of charge-sensitive devices at lower frequencies is limited by the low-frequency charge noise rather than by the shot noise.

2.4.4   Low-frequency charge noise

At low frequencies, the extreme charge sensitivity of SETs and all other charge-sensitive devices is limited by the low-frequency charge noise. This noise, also known as $1/f$ noise, has a power spectrum $S_Q \propto 1/f^\alpha$ (f is frequency and $\alpha \sim 1$) and has been observed in all types of electrical circuits.

There have been extensive studies in the last three decades about $1/f$ noise in different systems including single electron devices [15, 38, 39, 40, 41, 42], nanowires [43] and even recently in graphene devices [44]. Despite all these studies, the exact origin and physics of this noise is still an open question.

The most accepted scenario is that this noise originates from an ensemble of two-level fluctuators (TLFs), which reside in the vicinity of the device. Typically a TLF consists of a charged particle which fluctuates between two nearby positions (potential wells)[Figure 2.2(a)].

If a TLF is active in the vicinity of a SET, it will cause a random telegraph noise in the signal. Random telegraph noise (or burst noise) is a noise process in which signal jumps back and forth randomly between two (or more) discrete levels [Figure 2.2(c)]. This type of noise can be observed very frequently while measuring with SETs and can be explained as follows; if a TLF is coupled to the SET island, depending on its state, it will induce different amounts of charge on the SET island and consequently change the current passing through the device [Figure 2.2(b)].

This extreme charge sensitivity of SETs is a ''double-edged sword''. Although due to this extreme charge sensitivity they have been used extensively in research, at the same time fluctuations of any small charged particle in the vicinity of them, can disturb their performance.

2.5   Ensembles of two-level fluctuators

As mentioned in the previous Section, each TLF is a charge particle fluctuating between two different positions. If the energy difference between the two states is ΔE and the TLF switches with rate $\omega_0 = 1/\tau_0$ (τ_0 is the characteristic time), this will induce a random telegraph noise on the SET which in the frequency domain will be translated to a Lorentzian spectrum with a knee-frequency of ω_0 [45],

$$S_{Q,i}(\omega) = (\delta q)^2 \cosh^{-2}(\frac{\Delta E}{2k_B T})\frac{\omega_0}{\omega_0^2 + \omega^2}. \tag{2.6}$$

where δq is the charge induced on the SET island and T is the temperature. As we can see, the spectrum of a single TLF can not explain the observed $1/f$ noise but the superposition of an ensemble of such TLFs with different switching rates will result in a $1/f$ noise power spectrum. Assuming an ensemble of N TLFs, we can find the total noise induced from this ensemble, by simply summing the power spectral density of individual TLFs since we assume that the switching events in different TLFs are independent,

$$S_Q(\omega) = \sum_{i=1}^{N} S_{Q,i} \tag{2.7}$$

and if N is large enough, this will lead to an integral as,

$$S_Q(\omega) = \int S_{Q,i}(\omega) D(\tau_0) d\tau_0 \tag{2.8}$$

where $D(\tau_0)$ is the probability density of characteristic times.

With the natural assumption that the energy differences, ΔE, between the two energy levels in the TLFs are uniformly distributed, the characteristic times will be logarithmically spaced in frequency which in turn results in the observed $S_Q(\omega) \propto 1/\omega$.

Here we should note that if one replaces $S_Q \propto 1/\omega$ into Eq. 2.4, the auto-correlation function integral would not converge. This is not a problem for physical

systems since any ensemble of TLFs will have a lower and upper limit for the characteristic times, *i.e.* $\tau_{min} \ll \tau_0 = 1/\omega_0 \ll \tau_{max}$, where τ_{min} and τ_{max} are the characteristic times for the fastest and the slowest TLFs in the ensemble respectively [46]. This physical assumption limits $1/f$ noise between $\omega_{min} = 1/\tau_{max}$ and $\omega_{max} = 1/\tau_{min}$ frequencies and for the rest of the thesis, we assume that TLFs transition frequencies are well within these limits. Although $1/f$ noise has been measured for more than 7 decades of frequencies [47], the exact values of ω_{min} and ω_{max} are not known.

2.5.1 Microscopic models for two-level fluctuators

Sofar we have discussed the general mathematical background for description of TLFs. In order to study the TLFs further, one needs to consider a microscopic model for them. Any microscopic model should address several open questions about TLFs; their microscopic origin (what are they), their distribution (where are they) and their densities (how many of them). Also one more important question is what is their activation mechanism *i.e.* does the charged particle fluctuate between two potentials due to thermal activation or quantum tunneling. Sofar, there is no generally accepted model which answer these questions about TLFs.

Regarding the location of TLFs, different experiments point in different directions. Zorin *et al.* have measured the correlation in noise between two nearby SETs and concluded that the TLFs most likely are distributed in the bulk of the substrate [48]. Song *et al.* suggest that most likely source of $1/f$ noise is the random motion of TLFs inside the tunnel junctions [49]. Zimmerman *et al.* conclude that charge noise originate from a cluster of TLFs and further since the switching rates depend on the gate voltages rather than the source-drain voltage they conclude that "unambiguously TLFs are not located in the tunnel barrier"[50].

Suspended SETs [51] and SETs on thin Si_3N_4 membranes were made [52] to check the role of the substrate but the observed charge noise level in both cases were within the range of the conventional SETs. In the case of the suspended SET, the authors suggest that the noise arises from the self-heating of the SET [51]. In another approach, SETs were fabricated in a stack design *i.e.* the SET island was made on one of the electrodes without direct contact to the substrate [42]. The reported charge noise level in this case was substantially lower than for ordinary SETs.

Kafanov *et al.* [53] and Brown [54] *et al.* proposed that the origin of TLFs can be the stray microscopic metallic grains which form during the fabrication of SETs (see Chapter 3 for fabrication methods). They propose that electrons can jump back and forth between the SET island and these grains, producing the charge noise.

2.5.2 Thermal properties of TLFs

Regardless of their location, TLFs are commonly modelled as a charged particle fluctuating in a double-well potential. An alternative model is a single well close to a metallic surface where charged particles can fluctuate between the metal and the potential well.

If the charge particle is thermally activated, then following the Boltzmann distribution,

$$\tau_0 = \frac{1}{\omega_{att}} \, e^{\epsilon/k_B \, T} \qquad (2.9)$$

where ω_{att} is the attempt frequency and ϵ is the activation energy (or barrier height) of the TLF. Dutta and Horn showed that for thermally activated *symmetric* TLFs with a uniform distribution of activation energies, D(ϵ), the charge noise will be $1/f$-like and will increase linearly with increasing the temperature, $S_Q \propto T/f$ [55].

We have shown in paper I that if the charged particle in the TLF fluctuates between the two positions by quantum tunneling rather than by the thermal activation, this process also leads to $S_Q \propto T/f$.

Kenyon *et al.* assumed an *asymmetric* model for the TLFs with two different activations energies which were uniformly distributed over the ensemble of TLFs [56]. Under these conditions, they found $S_Q \propto T^2/f$.

Thus measuring the temperature dependence of the charge noise gives important information about TLFs and help to verify the microscopic models. Previous temperature dependence measurements of charge noise show either T-dependence or T^2-dependence [56, 57]. In paper I, we have made a careful study and measured a linear temperature dependence for charge noise for more than 200 different temperature points.

2.5.3   TLFs in an external electric field

The majority of previous measurements on TLFs are preformed in thermal equilibrium. When TLFs are studied in thermal equilibrium, *e.g.* in noise measurements, there is no straightforward way to distinguish whether the charge in the TLF switches position due to thermal activation above the barrier or by quantum tunneling through the barrier (Figure 1.1). Given a flat distribution of barrier heights and energy level differences, both mechanisms gives rise to the same linear temperature dependence of the noise.

In paper II, we apply a step voltage to the gate electrode of the SET. This will push the TLF ensemble out of equilibrium. Measuring the relaxation of the TLF ensemble after the step, enable us to draw more firm conclusions regarding the microscopic model of TLFs and their activation mechanism.

2.5.4   Step response; single TLF

We start by finding the charge induced on the SET island by switching an individual TLF. When we apply a voltage to the gate electrode, an electric field, $\vec{E}_G(\vec{r})$, is generated between the gate and the other electrodes which we refer to as the gate field (solid lines in Figure 2.3). We can define the normalized gate field as $\vec{e}_G(\vec{r}) = \frac{\vec{E}_G(\vec{r})}{\Delta V}$. The voltage step of ΔV applied to the gate, shifts the potential of the TLF with displacement vector $\vec{d}$ [Figure 2.3(b)], by

(a)

(b)
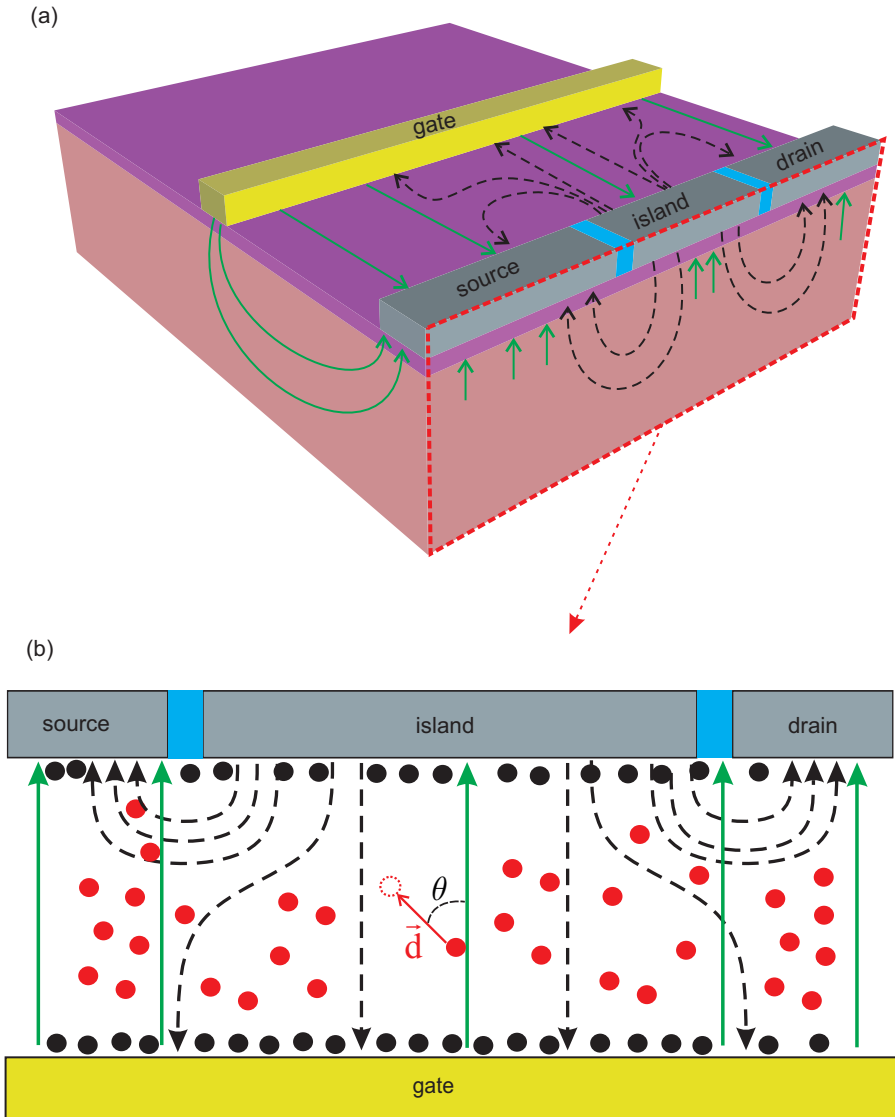
Figure 2.3: TLFs and field distributions in the dielectric surrounding a SET: (a) Schematic three dimensional image of the SET, gate and the field distributions. Solid green lines show the gate field, $\vec{E}_G(\vec{r})$, and the black dashed lines show the virtual field, $\vec{E}_V(\vec{r})$. (b) Simplified two dimensional geometry where the SET and the gate are considered in a parallel-plate capacitor model. An individual TLF with displacement vector $\vec{d}$ is shown in the center. The red and black circles represent the volume and surface distributions of TLFs, respectively.

$$\delta E(\vec{r}, \vec{d}) = e\vec{d} \cdot \vec{E}_G(\vec{r}) = ed\Delta V e_G(\vec{r}) \cos(\theta), \tag{2.10}$$

where θ is the angle between $\vec{e}_G(\vec{r})$ and $\vec{d}$.

Next we should calculate how much charge is induced on the SET island when the charged particle in the TLF moves between two positions. To do so we use the reciprocity method which is described in Refs. [58, 59]; we consider a *virtual* situation where the island is connected to a potential V_0 and all other electrodes are grounded. This will produce an electrical field, $\vec{E}_V(\vec{r})$, which we refer to as virtual field (dashed lines in Figure 2.3) and again we define the normalized field as $\vec{e}_V(\vec{r}) = \frac{\vec{E}_V(\vec{r})}{V_0}$. For an individual TLF at any point $\vec{r}$ in space, and displacement vector $\vec{d}$, the charged induced on the SET island is

$$\delta q(\vec{r}, \vec{d}) = e\vec{d} \cdot \vec{e}_V(\vec{r}, \vec{d}). \tag{2.11}$$

The spatial distribution of the gate field and virtual field for real geometries can be calculated using finite element method (FEM) software packages (see Supplemental Material of paper II).

2.5.5 Step response; ensemble of TLFs

We assume an ensemble of N TLFs with different displacement vectors, $\vec{d}$, initial energy differences, ΔE, and different switching times, τ. To find the total charge induced on the SET island, Q, we sum up the contribution from individual TLFs.

We note that the equilibrium population of the excited state of the TLF is given by the Fermi function $f(\Delta E)$, where ΔE is either the energy of the single well compared to the Fermi energy, or the (positive) energy difference between the two wells of the double well, then

$$Q(t) = \sum_{i=1}^{N} \delta q_i \left[f(\Delta E_i) - f(\Delta E_i + \delta E_i) \right] (1 - e^{-t/\tau_i}). \tag{2.12}$$

where subscript i denotes the individual values for each TLF. The factor $(1 - e^{-t/\tau_i})$, is the probability for a TLF with characteristic time τ_i to switch after time t. Following the derivation in the Supplemental Material of paper II, the summation can change to an integral assuming N is large enough,

$$Q(t) = \int n(\vec{r}, \vec{d}, \Delta E, \tau) \delta q(\vec{r}, \vec{d}) \left[f(\Delta E) - f(\Delta E + \delta E) \right] (1 - e^{-t/\tau_i}) \, \mathrm{d}\Delta E \mathrm{d}\vec{r} \, \mathrm{d}\vec{d} \mathrm{d}\tau. \tag{2.13}$$

where we have introduced $n(\vec{r}, \vec{d}, \Delta E, \tau)$, the density of TLFs. We can simplify the integral further if we assume the following physical assumptions:

- We assume that the initial energy differences, ΔE, has a flat distribution.

- We also assume that the logarithm of the switching times, $\log(\tau)$, has a flat distribution between minimum ($\tau_{\min}$) and maximum switching times ($\tau_{\max}$).

Then, for $\tau_{\min} \ll t \ll \tau_{\max}$ we find,

$$Q(t) = \frac{\ln(\omega_{\max} t) + \gamma}{\ln(10)} \int n(\vec{r}, \vec{d}) \, \delta q(\vec{r}, \vec{d}) \delta E(\vec{r}, \vec{d}) \, \mathrm{d}\vec{r} \, \mathrm{d}\vec{d}, \qquad (2.14)$$

where γ is Euler's gamma and $n(\vec{r}, \vec{d})$ is the TLF density per decade of frequency and per unit of energy difference. Here we have defined the density of TLFs, per decade of frequency and that is the reason to have the ln(10) term in the denominator.

The further evaluation of $Q(t)$ requires to know the density function of TLFs. We consider two special cases for the distribution of TLFs, (*i*) a homogeneous volume distribution [red dots in Figure 2.3(b)], with a volume density n_v, and (*ii*) a homogeneous surface distribution of TLFs [black dots in Figure 2.3(b)], with a surface density n_s. For the homogeneous volume distribution, we assume that TLFs are randomly oriented in the bulk of the substrate. We find,

$$Q_v(t) = \frac{1}{3} e^2 d^2 \Delta V n_v \frac{\ln(\omega_{\max} t) + \gamma}{\ln(10)} \int_V e_G(\vec{r}) \, e_V(\vec{r}) \cos\theta_V \mathrm{d}\vec{r}. \qquad (2.15)$$

For the homogeneous surface distribution, where electrons can tunnel between the fermi surface of the metallic electrodes and local surface states, we obtain

$$Q_s(t) = e^2 d^2 \Delta V n_s \frac{\ln(\omega_{\max} t) + \gamma}{\ln(10)} \int_S e_G(\vec{r}) \, e_V(\vec{r}) \cos\theta_V \mathrm{d}\vec{r}. \qquad (2.16)$$

This shows that measuring $Q(t)$ can give information regarding the distribution and densities of TLFs.

2.6 Circuit quantum electrodynamics (circuit QED)

Quantum electrodynamics (QED) is the quantum theory of light and matter interaction [60, 61]. It deals with relativistic quantum description of electromagnetic fields and their interaction with charged particles. QED has been one of the most successful theories to explain the light-matter interaction experiments so that, Richard Feynman as one of the pioneers of this field once mentioned : ''...sofar, we have found nothing wrong with the theory of quantum electrodynamics. It is, therefore, I would say the jewel of physics- our proudest possession''[61].

One of the most studied platforms to explore and test the QED predictions is the field of cavity QED [62, 63, 64, 65, 66]. In this field, ''Rydberg atoms'', which are real atoms with very large dipole moments, are prepared inside a cavity, a superconducting metallic box. When photons are sent through the cavity, they bounce back and forth between the cavity walls many time before they leak outside. There is a chance that these photons are absorbed by the atom and bring it to the excited state. An exited atom can go back to its ground state by spontaneously emitting a photon (a process which is known as spontaneous emission). This coherent exchange of a photon between the atom and the filed in the cavity is known as the vacuum Rabi oscillations. The regime where the rate of this atom-light interaction, *i.e.* the rate of absorbing and re-emitting of the photons by the atom, is much higher than the photon leakage rate out of the cavity and other dissipation mechanisms, is called the strong coupling regime of the cavity QED. The unique quantum behaviour of the atom-light systems (like vacuum Rabi oscillations) is revealed in this strong coupling regime. Although impressive results have already been obtained in the cavity QED experiments [67, 68, 69], it has always been very challenging to prepare and probe the real atoms inside a cavity.

In recent years, advances in nanofabrication and cryogenic microwave measurement techniques, have resulted in a new type of QED experiments, namely circuit QED [70, 71, 72]. In circuit QED, instead of real atoms, superconducting circuits with engineered energy spectra are used. These superconducting circuits act as ''artificial atoms'' and have dipole moments orders of magnitude larger than real atoms, which enhance the atom-light interaction significantly. Furthermore, in circuit QED the three dimensional cavity, is replaced by a superconducting microwave resonator, where photons are confined to travel in one dimension [73, 74].

The circuit QED setup has several advantages over cavity QED. Firstly, the artificial atoms are fixed in space. Secondly, the artificial atoms are orders of magnitude larger than the real atoms, and therefore have much larger dipole moments. Thirdly, we can engineer and tune their transition energies and their coupling to the environment.

Different types of artificial atoms (qubits) have been proposed and realized within the context of circuit QED [75], such as flux qubits [76, 77], phase qubits [78], and charge qubits [79, 80, 81, 82]. The charge qubit, the single Cooper pair box (SCB) [83, 84, 85], can be either capacitively or inductively shunted and are then called transmon [86] and fluxonium [87] respectively. The SCB and the transmon will be described in more details later. These qubits have different working principles but

the common key element in all of them is the Josephson junction.

2.6.1   Josephson junctions and SQUID

In 1911, Kamerlingh Onnes discovered that when certain materials are cooled down below a characteristic critical temperature, T_c, their electrical resistance abruptly drops to zero [88]. This phenomenon is known as superconductivity [89].

About 40 years later, Bardeen, Cooper, and Schrieffer presented the first microscopic theory of superconductivity (BCS theory) [90]. In a nutshell, they assumed that when a superconductor is cooled down below its critical temperature, T_c, an effective attraction force is formed between its electrons as a result of the coupling of electrons to the crystal lattice. This net attraction force causes electrons to overcome the Coulomb repulsion between them and form pairs which are known as the Cooper pairs [91]. These Cooper pairs show bosonic behaviour (in contrast to the electrons which are fermions) and can condense into a collective ground state which is described by a common macroscopic wave function since the phase of each Cooper pair is coherent with the rest.

Brian Josephson in 1962, predicted that when two superconductors are separated by a thin insulating barrier, still a current can flow between them due to the tunneling of Cooper pairs [92, 93]. Today, this effect is known as the Josephson effect and the weak link structures which exhibit this effect are known as the Josephson junctions [94].

According to Josephson, the supercurrent through the junction, I_s, depends on the phase difference across the junction, ϕ (the DC Josephson effect),

$$I_s = I_c \sin \phi, \tag{2.17}$$

where I_c is the critical current of the junction, the maximum current which can pass through the junction with zero voltage. Secondly, the voltage drop across the junction, V, is proportional to the time derivative of the phase difference (the AC Josephson effect),

$$V = \frac{\hbar}{2\,e} \frac{d\phi}{dt}. \tag{2.18}$$

Josephson junctions are characterized by two energy scales, the charging energy, E_C and the Josephson energy, E_J. As discussed in Section 2.2, the charging energy, is defined as $E_C = (2e)^2/2C_J$, where C_J is the capacitance of the junction. Note that the elementary charge is now the charge of the Cooper-pair, $2e$. The charging energy can be understood as the energy stored in the junction.

The Josephson energy is defined as $E_J = \int V I_s dt$ and can be interpreted as the energy of the tunneling Cooper pairs. It can easily be derived from the Josephson relations 2.17 and 2.18,

$$E_J(\phi) = \int V I_s dt = \int (\frac{\hbar}{2\,e} \frac{d\phi}{dt})(I_c \sin \phi) dt = E_{J_{max}}(1 - \cos(\phi)), \tag{2.19}$$
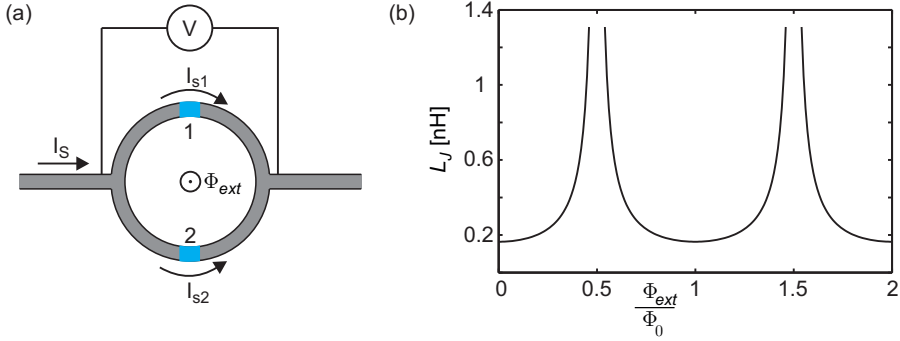
Figure 2.4: The superconducting quantum interference device (SQUID) as a tunable inductor. (a) Schematic illustration of the SQUID: two Josephson junctions (in blue) are situated in a superconducting loop. (b) The inductance of the SQUID changes with the external magnetic flux, Φ_{ext} applied through the SQUID loop. Here the inductance of a SQUID with symmetric junctions and $I_0 = 1\mu A$ is plotted as a function of the Φ_{ext}.

where $E_{J_{max}}$, the maximum Josephson energy, is defined as $E_{J_{max}} = \hbar I_c/2e$.

Combining the Josephson relations we find that a Josephson junction can be viewed as an inductor,

$$V = L_J \frac{dI_s}{dt}, \tag{2.20}$$

where $L_J = \Phi_0/(2\pi I_c \cos\phi)$, is defined as the *nonlinear* inductance of the Josephson junction. The nonlinearity of the Josephson junctions plays an important role in their application in circuit QED. It causes an unequal spacing between the energy levels of the artificial atoms, which allows us to address the energy levels separately [95].

Devices based on the Josephson effect, are widely used in circuit QED and quantum information [75, 96, 97]. One of these devices is the superconducting quantum interference device (SQUID) which consists of two Josephson junctions in parallel, forming a loop [Figure 2.4(a)][98]. For SQUIDs, the phase difference across the two junctions is a function of the external magnetic flux in the loop, Φ_{ext},

$$\phi_2 - \phi_1 = 2\pi \frac{\Phi_{ext}}{\Phi_0}, \tag{2.21}$$

where ϕ_1 and ϕ_2 are the phase differences across the individual junctions and Φ_0 is the magnetic flux quantum. Using Kirchhoff's circuit law we find,

$$I_s = I_{s1} + I_{s2} = I_{c1} \sin\phi_1 + I_{c2} \sin\phi_2, \tag{2.22}$$

where I_{c1} and I_{c2} are the critical current of individual junctions. For a SQUID with identical junctions ($I_{c1} = I_{c2} = I_0$), using Eq. 2.21 we obtain,

$$I_s = 2I_0 \left|\cos(\pi\Phi_{ext}/\Phi_0)\right| \sin\phi, \tag{2.23}$$

where $\phi = (\phi_1 + \phi_2)/2$. This is similar to Eq. 2.17 which allows us to treat the SQUID as a single Josephson junction with the tunable critical current of $I_c = 2I_0 \left|\cos(\pi\Phi_{ext}/\Phi_0)\right|$.

Further, similar to Eq. 2.20, we can find the effective nonlinear inductance of the SQUID as,

$$L_J(\Phi_{ext}) = \frac{\hbar}{4eI_0 \left|\cos(\pi\Phi_{ext}/\Phi_0)\right|}. \tag{2.24}$$

This shows that by changing the external flux inside the SQUID loop, we can exploit it as a tunable nonlinear inductor. Figure 2.4(b) shows the inductance of a SQUID with $I_0 = 1\mu A$, as a function of the Φ_{ext}. Similarly, the Josephson energy of the SQUID is also tunable with respect to Φ_{ext}. For a symmetric SQUID,

$$E_J(\Phi_{ext}) = E_{J_{max}} \left|\cos(\pi\Phi_{ext}/\Phi_0)\right|, \tag{2.25}$$

where $E_{J_{max}}$ here is the sum of the maximum Josephson energy of the individual junctions.

2.6.2   Artificial atoms

As mentioned earlier, different types of artificial atoms have been already studied in circuit QED experiments. Exploiting the unique properties of Josephson junctions, different systems manipulate the quantum states of artificial atoms in different ways [81, 75, 99, 100, 97, 96].

In this thesis, we focus on experiments which are performed with transmon qubits [86]. The transmon qubit, as will be explained later, can be viewed as a capacitively shunted Cooper pair box where the electric charge difference across the Josephson junctions is the primary knob to control the system [81, 85]. In the following sections, we describe the working principle of the Cooper-pair box and discuss its interaction with light, in this case, photons with microwave frequencies.

2.6.3   Single Cooper pair box (SCB)

The single electron box (SEB), is already discussed in Section 2.2. The superconducting version of the SEB is the single Cooper pair box (SCB) [83, 84, 85]. The single Cooper pair box was the first version of charge qubit, which was experimentally realized in 1999 [79]. It consists of an isolated metallic island connected via a tunnel junction to another electrode. Similar to the SEB, the potential of the island can be controlled by a gate electrode which is capacitively coupled to the island. Cooper pairs can tunnel in or out of the island through the tunnel junction.

The operation of the SCB is described by the charging energy, E_C, and the Josephson energy, E_J, of the junction. If we replace the SCB tunnel junction by

a SQUID, then as mentioned in previous section, we can tune its E_J by applying the external magnetic flux through the SQUID loop.

The general recipe in quantum mechanics to find the dynamics of a quantum systems is [11]:

- First, find the Hamiltonian of the system.

- Then, try to simplify the Hamiltonian if possible, by finding the conjugate variables.

- Finally, diagonalize the Hamiltonian which yields to different energy levels of the system.

Here, we take the same approach to find the dynamics of the SCB. If n Cooper pairs have tunneled into the island and the phase difference across the junction is, ϕ, then the Hamiltonian of the SCB with the junction capacitance, C_J and the gate capacitance, C_g is described by,

$$H = E_Q \, (\hat{n} - n_g)^2 - E_J \, \cos(\hat{\phi}),\qquad(2.26)$$

where $E_Q = 4E_C = (2e)^2/(2C_\Sigma)$ is the charging energy of the Cooper pairs. The total capacitance $C_\Sigma = C_g + C_J$ and $n_g = C_g \, V_g/(2e)$ is the normalized gate charge. We have omitted the terms in the Hamiltonian which are independent of n since they do not participate in the dynamics of the system. $\hat{n}$ and $\hat{\phi}$ are the Cooper pair number and phase difference operators respectively. They are conjugate operators are therefore related to each other in the following way,

$$\hat{n} = i \, \frac{\partial}{\partial \phi},\qquad(2.27)$$

and

$$\hat{\phi} = -i \, \frac{\partial}{\partial n}.\qquad(2.28)$$

Consequently, n and ϕ are conjugate variables which means they are related to each other through Heisenberg's uncertainty relation [11]. This allows us to express one of them in terms of the other. Rewriting the Hamiltonian in the charge basis, $|n\rangle$, results in,

$$H = \sum_{n=-\infty}^{\infty} E_Q(\hat{n} - n_g)^2 \, |n\rangle \, \langle n| - \frac{E_J}{2}(|n\rangle \, \langle n+1| + |n+1\rangle \, \langle n|).\qquad(2.29)$$

Now we can diagonalize this Hamiltonian and find the energy levels of the system as a function of n_g, our control knob in the system. If we limit the operation of the SCB to the two lowest energy levels, $|0\rangle$ and $|1\rangle$, and the gate charge to $0 < n_g < 1$, then the Hamiltonian simplifies to,
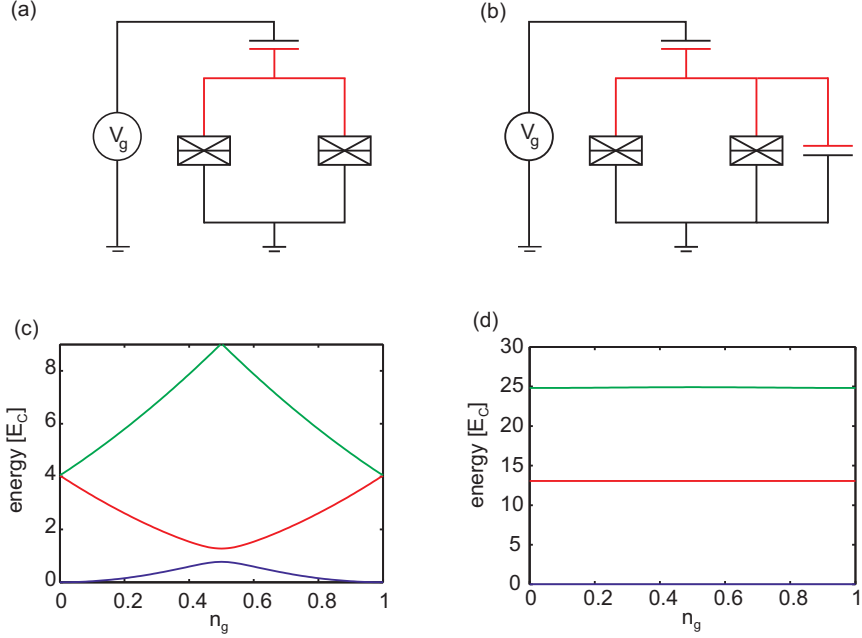
Figure 2.5: (a) The Single Cooper par Box (SCB) and the transmon. (a) Schematic of the SCB when the Josephson junction is replaced by a SQUID. (b) Schematic of the transmon. An extra shunted capacitor reduces the charging energy of the island. (c) The lowest three energy bands of a SCB versus the normalized gate voltage, n_g, for $E_J/E_C = 0.5$. (d) Similar to (c) but for $E_J/E_C = 25$.

$$H = \frac{1}{2} E_Q (2n_g - 1)\sigma_z - \frac{E_J}{2}\sigma_x. \qquad (2.30)$$

where σ_z and σ_x are the Pauli spin matrices [21]. The eigenvalues of this Hamiltonian (energy levels of the system) are,

$$E_{g,e} = \mp \frac{1}{2} \sqrt{E_Q^2(1 - 2n_g)^2 + E_J^2}. \qquad (2.31)$$

Using these two lowest energy levels allows us to exploit the SCB as a qubit with energy levels which is given by Eq. 2.31 and the energy difference between the two levels which varies as function of n_g.

2.6.4   Decoherence in a qubit

There are different noise sources in the environment which affect the performance of the SCB. Noise causes the qubit to decohere after some time. This means that after this time, the coherent superposition state will evolve to one of the $|0\rangle$ or $|1\rangle$ states.

The effect of the environment on the qubit is characterized by the decoherence time T_2 (or equivalently decoherence rate, $\gamma = 1/T_2$)

$$\gamma = \frac{1}{T_2} = \frac{\Gamma_1}{2} + \Gamma_\phi, \tag{2.32}$$

where Γ_1 is the relaxation rate (or equivalently $T_1 = 1/\Gamma_1$ is the relaxation time) and Γ_ϕ is the pure dephasing rate. Γ_1 is the rate at which qubit relaxes from its excited state to its ground state. It depends on the fluctuations of the electromagnetic fields which are coupled to the qubit at frequencies close to the qubit transition frequency. Γ_ϕ on the other hand, originates from fluctuations in the energy difference between the two states. For a charge qubit the dominant source of this pure dephasing is charge noise. Koch *et al.* suggested a modified version of the SCB, the transmon, which has a substantial lower charge sensitivity and subsequently has much less pure dephasing [86].

2.6.5 Transmon

The transmon qubit (short for "transmission line shunted plasma oscillation") is based on the SCB [86]. The difference is that the charging energy of transmon has been substantially decreased by shunting it with an additional capacitor, C_S, resulting in a higher E_J/E_C ratio. Figure 2.5 shows the lowest energy bands of the SCB for two different values of E_J/E_C ratio. By increasing the E_J/E_C ratio the energy bands become flatter. This makes the energy difference between the $|0\rangle$ and $|1\rangle$ states (transition frequency) less sensitive to charge and as a result more immune to the charge noise. We refer to the regime with $E_J/E_C > 20$ as the transmon regime.

In the transmon regime, the eigenenergy of the n'th energy level can be approximated as [86],

$$E_n \simeq -E_J + \sqrt{8E_C\,E_J}(n + \frac{1}{2}) - E_C(6n^2 + 6n + 3), \tag{2.33}$$

which results in

$$E_{01} \simeq \sqrt{8E_C\,E_J} - E_C, \tag{2.34}$$

for the lowest energy levels.

2.6.6 Atom-light interaction

Now that we have introduced our artificial atom, we can study its interaction with light. We consider a simple geometry, a transmon qubit embedded in an one dimensional open transmission line. Resonant propagating photons through the transmission line excite the qubit. As discussed earlier, the qubit will relax to its ground state by emitting a photon. The interference between the incident field and the radiated photon will be destructive in forward direction which gives rise to the extinction of the forward propagating photons.
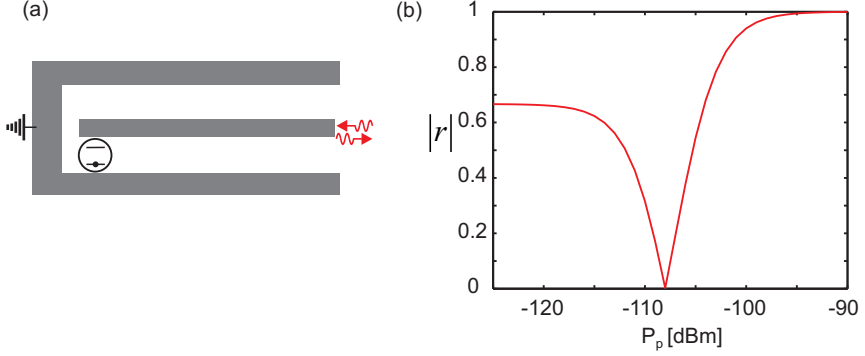
Figure 2.6: Transmon at the end of a single-ended transmission line. (a) Schematic illustration of the transmission line, ground planes and the transmon. The incident field will be reflected by the mirror or due to interaction with the atom. (b) Reflection coefficient versus power for a resonant field according to Eq. 2.35 and assuming $\Gamma_1/2\pi = 20$ MHz and $\Gamma_\phi/2\pi = 2$ MHz. In low power regime, the photons are reflected by the atom and in higher powers they are reflected by the mirror (see text).

Astafiev *et al.* and Peropadre *et al.* have studied such a system theoretically by finding the Hamiltonian of the quantum circuit model. Thanks to the relatively simple geometry of the device, they have derived analytical expressions for the scattering properties of the system *i.e.* the transmission coefficient, t, and the reflection coefficient, r of the incident field [101, 102].

Both Astafiev *et al.* [102] and Hoi *et al.* [103] have measured such a system and found the perfect agreement between the measurements and the theoretical predictions. They have used this platform to study several well-known quantum optic effects including the Mollow triplet and the Autler-Townes splitting. Hoi *et al.* have demonstrated that this system can be used to realize quantum devices like a single-photon router and a photon-number filter [103, 104, 105, 106].

A modified version of this system is when the transmon is embedded at the end of a single-ended transmission line (Figure 2.6). This system is interesting since it confines the emitted photons to propagate in one direction. The open or shorted end of the transmission line where qubit is situated, is always at a voltage antinode. If we probe the system with a strong resonant field, photons will reflect from the mirror without interacting with the qubit. This results in $|r| = 1$. For a weak resonant incident field, the reflection coefficient is simplified to [101]

$$r = 1 - \frac{2}{1 + 2\Gamma_\phi/\Gamma_1}. \tag{2.35}$$

We note that according to Eq. 2.34 if the atom-filed coupling is strong enough ($\Gamma_1 \gg \Gamma_\phi$), this also leads to $r = 1$. The difference is that in low power regime, the photons are reflected by the atom but with a π-phase shift, similar to the previous case.

As the power of the incident field increases, Eq. 2.34 does not hold anymore. For a resonant field with power P_p, the reflection coefficient is expressed as

$$r = 1 - \frac{2}{1 + 2\Gamma_\phi/\Gamma_1 + 2(\Omega_p/\Gamma_1)^2}, \tag{2.36}$$

where $\Omega_p = \sqrt{2\Gamma_1 P_p/\hbar\omega_a}$ is the Rabi frequency and $\omega_a/2\pi$ is the transition frequency of the atom. Figure 2.6 shows the reflection coefficient as a function of the incident power according to Eq. 2.35 for a resonant field. As explained before, in lower power regime, the photons are reflected due to the interaction with the qubit where as in higher power regime they get reflected by the mirror. As power increases, at some point there will be a perfect destructive interference between the filed reflected from the mirror and the field emitted by the atom. This results in $r = 0$ (Figure 2.6) and happens when $\Omega_p = \sqrt{\Gamma_1^2 - \Gamma_1\gamma}$. At this power, all the coherent incident field is absorbed by the atom and emitted incoherently with a random phase.

In Chapter 5 we describe an experiment where we characterize the scattering properties of two transmons at the end of an open transmission line. We can control each transmon individually and study them when they are far detuned or when they are both in resonance with the incident field.

2.7   Vacuum fluctuations

Vacuum is usually considered as the absence of anything. The classical physics recipe to reach the vacuum is simple : empty a container from all the particles and you have vacuum. This classical picture of the vacuum also agrees with the conservation of energy.

In quantum physics, however, vacuum is not a simple concept anymore [107]. According to the Heisenberg energy-time uncertainty relation, $\Delta E \, \Delta t \geq \hbar/2$, where $\hbar$ is Planck's constant divided by 2π. The consequence of this relation is that, the actual value of any observable (for example the electromagnetic field) at a specific time, fluctuates around a constant value. This is also valid for the vacuum *i.e.* even in the absence of any external electromagnetic field and at absolute zero temperature, there exist fluctuations known as vacuum fluctuations. Although these fluctuations are so small that for any classical measurement they can be averaged out, they lead to some interesting measurable effects such as the Lamb shift [108, 109, 110, 111], spontaneous emission from atoms [110, 111] and the Casimir effect [112].

The Lamb shift is the discrepancy between the experimentally observed energy and the Schrodinger equation solution of the energy levels of the hydrogen electron [108, 109]. The theory predicts that the $2S_{1/2}$ state and the $2P_{1/2}$ state should have the same energy but Lamb showed that the $2S_{1/2}$ has slightly higher energy level than the $2P_{1/2}$ [108]. This difference was explained by Bethe as a result of the interaction between the electron and the vacuum fluctuations [109]. Fragner *et al.* resolved the vacuum fluctuations in a transmission-line resonator by measuring the Lamb shift of a transmon qubit [113].

Spontaneous emission of atoms, as mentioned before, is a more familiar effect since it generates most of the visible light around us in the form of thermal radiation [110, 111]. If an atom is in its exited state, interactions with vacuum fluctuations will cause the atom to go to its ground state and spontaneously emit a quanta of energy, a photon.

2.8   Dynamical Casimir effect

In 1948, Hendrik Casimir predicted that if two uncharged conductor plates (mirrors) are brought very close to each other in vacuum, surprisingly they experience an attractive force between them [112]. Today, this effect is called the Casimir effect (or more precisely the static Casimir effect) and the force between the plates is known as the Casimir force [114].

This effect is due to the quantum mechanical nature of the electromagnetic fields in the vacuum. More virtual photons are present in the space outside of the plates than between them, in other words, the electromagnetic mode density is different inside and outside the plates [Figure 2.6(a)]. This results in a radiation pressure from the vacuum fluctuations which pushes the plates together. This static Casimir effect has been extensively measured by different groups [115, 116].
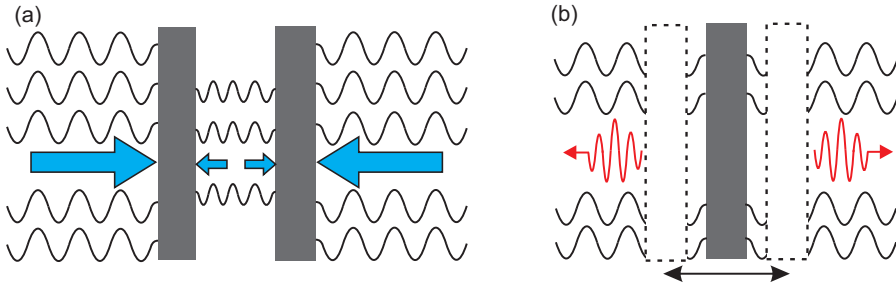
Figure 2.7: Schematic illustration of the Casimir effect. (a) Static Casimir effect: the difference between the electromagnetic field density in vacuum inside and outside the plates, produces different radiation pressures which pushes them towards each other. (b) Dynamical Casimir effect: the interaction of the vacuum fluctuations with a time-dependent boundary condition generates photons. A moving conducting plate acts aa the time-dependent boundary condition for the vacuum field.

A simple experiment can demonstrate the classical water-wave analog of the Casimir effect [117]. If two parallel plates are submerged into the bath of water which contains an ultrasonic sonicator, the plates attract each other once the sonicator is turned on. Here, the force between the plates arises from the water waves rather than from the vacuum fluctuations and the plates are pushed towards each other since fewer waves are formed in the space between the plates compared to the outside.

In 1970, Gerald Moore predicted that oscillating the mirrors of a cavity generates real photons [18]. This effect is known as the dynamical Casimir effect (DCE) [118, 20], and originates from the interaction of the vacuum fluctuations with the time-dependent boundary condition of the field. Later, it was shown that a nonuniform acceleration of a single mirror in vacuum is enough to generate photon radiation [17, 19]. All of these early predictions of the DCE [18, 19, 17], were published in mathematical physics journals which indicates that they were considered as abstract thoughts rather than the measurable physical properties.

A simple way to interpret the DCE is to explain the photon emission in analogy with optical parametric processes [119]. The mechanical oscillation with frequency of Ω will be transformed into two photons of frequency ω and ω' which add up to the oscillation frequency ($\Omega = \omega + \omega'$). This implies that the DCE radiation is always generated in the form of a pair of correlated photons which is one of the most important signatures of the DCE. It also explains why the DCE does not violate the conservation of the energy, since the energy of radiated photons is supplied by the moving mirror.

Lambrecht *et al.* calculated the spectrum of the generated DCE photons, $n(\omega)$, for an oscillating mirror with oscillation amplitude of, a and found [120],

$$n(\omega) \propto (\frac{a}{c})^2 \, \omega(\Omega - \omega) \tag{2.37}$$

which is a parabolic shape between zero frequency and the oscillation frequency, Ω, with a maximum at $\omega = \Omega/2$. This parabolic spectrum is a characteristic feature of motion induced radiation, and is considered as another important signature of the DCE.

Furthermore, Lambrecht *et al.* showed that N, the number of emitted photons per period T is proportional to the square of the ratio of the mirror maximum velocity, v_{max}, to the speed of light, c,

$$\frac{N}{T} = \frac{\Omega}{3\pi} \left(\frac{v_{max}}{c}\right)^2 \tag{2.38}$$

where $v_{max} = a\Omega$ is the maximum velocity for a mirror with the oscillation frequency of Ω. This expression shows that to achieve a considerable photon generation rate the mirror should move with relativistic velocities, *i.e.* velocities close to the speed of light.

This expression shows why the experimental realization of this effect is very challenging. It is not feasible to move any massive object with relativistic velocities. For example, moving a nano sized plate in a nano mechanical oscillators with an amplitude of 1 nm and frequency of 1 GHz yields to the photon production rate of 10^{-9} photons per second (corresponds to approximately 3 photons per century) which is too low to detect experimentally. There have been several theory proposals to instead change the boundary conditions of the field by some effective motion rather than by moving a massive mirror [121, 122, 123, 124].

In 2009, Johansson *et al.* proposed that the DCE can be observed experimentally in the context of the circuit QED [125, 126]. They proposed a simple system which is a coplanar waveguide coupled to the SQUID (Figure 2.7). Their idea was to apply an oscillating magnetic flux to the SQUID, which would modulate the effective length of the optical waveguide analogous to moving the mirror in the original conception of the dynamical Casimir effect.

They consider a superconducting transmission line with a characteristic capacitance, C_0, and a characteristic inductance, L_0, per unit length. In this case, the photon propagation velocity in the transmission line will be $v = 1/\sqrt{C_0 L_0}$. The transmission line is terminated at one end by the SQUID loop.

We already showed in Sec. 2.5.1 that the inductance, L_J (Eq. 2.24), and the Josephson energy, E_J (Eq. 2.25) of the SQUID can be tuned by changing the external magnetic flux inside the SQUID loop. Here, by exploiting these properties of the SQUID, they find the effective electrical length of the transmission line, L_{eff},

$$L_{eff}(\Phi_{ext}) = \frac{L_J(\Phi_{ext})}{L_0} \tag{2.39}$$

where $L_J(\Phi_{ext})$ is defined as Eq. 2.24. This shows that the effective length of the transmission line can be changed by changing the Φ_{ext}. In order to generate the DCE radiation, L_{eff} should change with a nonuniform acceleration for example a sinusoidal function. For a small-amplitude sinusoidal drive, the effective length modulation is also harmonic, $L_{eff}(t) = L_0 + \delta L_{eff} \cos(\Omega t)$, where δL_{eff} is the amplitude of the effective length modulation.
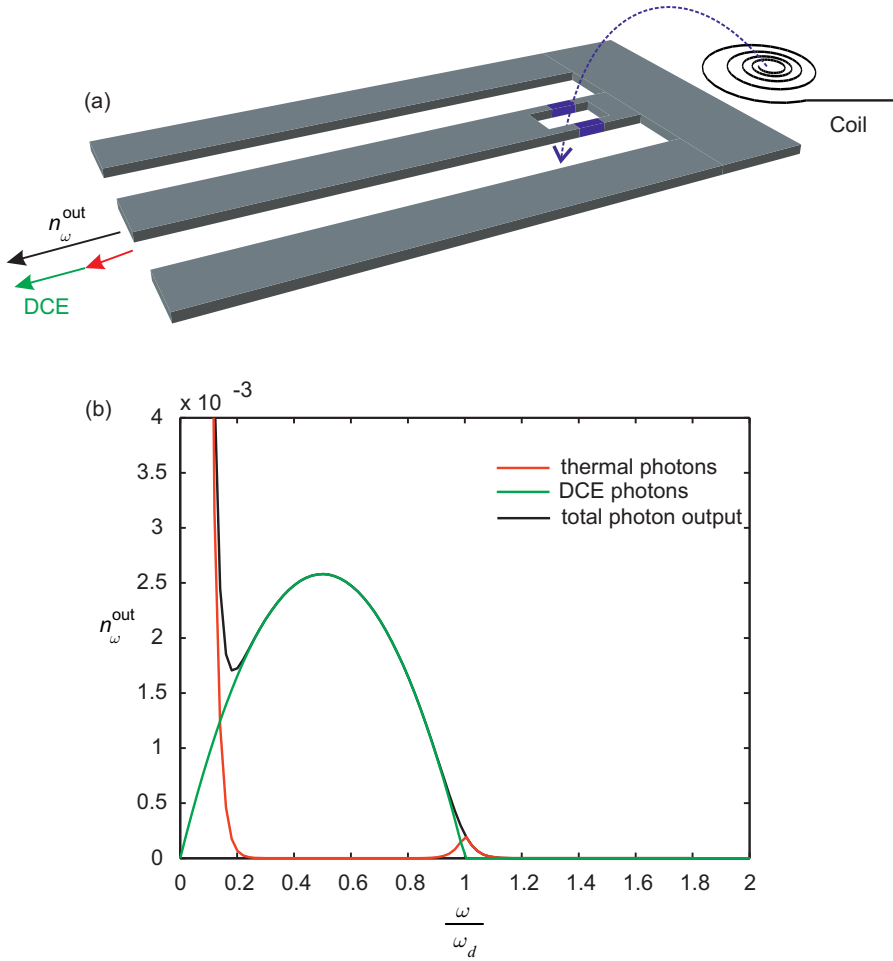
Figure 2.8: DCE in circuit QED: (a) Schematic illustration of the proposed set up to observe DCE photons in a transmission line coupled to a SQUID. (b) Output photon-flux density for the setup in (a) predicted by the theory where we have assumed temperature of 10 mK and $\delta L_{eff} = 0.1 L_{eff}$. Even in the presence of the input thermal photons, the DCE parabola is visible. This indicates that it is possible to detect the DCE photons in realistic conditions.

By assuming a small-amplitude sinusoidal drive signal, at frequency Ω, they can calculate the output photon-flux density, n_ω^{out},

$$n_\omega^{out} = n_\omega^{in} + \frac{(\delta L_{eff})^2}{v^2}\omega\,|\Omega - \omega|\,n_{|\Omega-\omega|}^{in} + \frac{(\delta L_{eff})^2}{v^2}\omega(\Omega - \omega)\Theta(\Omega - \omega) \quad (2.40)$$

where Θ is the Heaviside step function and n_ω^{in} is the input thermal photons density at temperature T,

$$n_\omega^{in} = \frac{1}{\exp(\hbar\omega/k_B T) - 1} \quad (2.41)$$

Here, the first term in Eq. 2.35 is the elastic reflection of the input thermal photons from the end of the transmission line. The second term is the up-converted thermal photons. These two first term represent purely classical effects and are zero at zero temperature. The third term is the photon-flux density of the DCE photons. Figure 2.7 shows n_ω^{out} for the realistic experimental parameters (see Figure caption). The parabola (green), as mentioned before is a signature of the DCE photons.

Another important signature of the DCE radiation, as mentioned earlier, is that the photons are generated in pairs. This effect manifests itself as correlations between photons at symmetric frequencies around half of the driving frequency *i.e.* correlations between photons generated at $\Omega/2 + \delta\omega$ and $\Omega/2 - \delta\omega$ where $\delta\omega < \Omega/2$.

In principle these correlations can be measured in a coincide-count experiment. The normalized second-order correlation function, $g^{(2)}$, is a direct measurement of the intensity-intensity correlations and defined as,

$$g^{(2)}(\tau) = \frac{G^{(2)}(\tau)}{G^{(1)}(0)G^{(1)}(\tau)} \quad (2.42)$$

where $G^{(2)}(\tau)$ is the probability to have two photons after delay time τ and $G^{(1)}(0)$ ($G^{(1)}(\tau)$) it he probability to have one photon at zero time delay (after delay time τ). If the generation of two photons is not correlated, *i.e.* the generation of two photons are independent events, then $G^{(2)}(\tau) = G^{(1)}(0)\,G^{(1)}(\tau)$ and the $g^{(2)}(\tau)$=1. For zero time delay, the $g^{(2)}(0)$ can be simplified to

$$g^{(2)}(0) = 2 + \frac{1}{\epsilon^2} \quad (2.43)$$

where $\epsilon = \delta L_{eff}\Omega/2v$. This implies that for zero delay time, we should observe $g^{(2)}(0) > 2$, which is known as the superbunching of photons.

Direct measurement of the correlation functions is very challenging in the microwave regime since firstly, sofar there is no reliable single photon detector in the microwave regime and secondly, amplifiers add a substantial amount of noise, which smears the statistics. However, it is shown that instead in the microwave regime $g^{(2)}$ function can be measured by averaging the output power of the linear amplifiers for long periods of time [127].
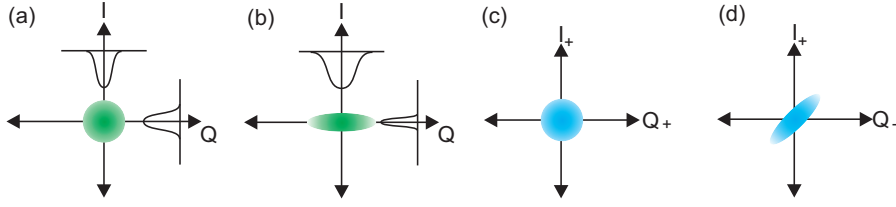
Figure 2.9: Squeezing of light: (a) Schematic illustration of the Gaussian error circle for an unsqueezed state. (b) By suppressing the noise in one quadrature, we produce a so called squeezed state. The error in the other quadrature subsequently increases. (c,d) In two-photon processes the quadratures of each individual mode remains unsqueezed (c), but the are cross-correlations between quadratures of different modes producing two-mode squeezed states (d).

Another way to probe the correlations is to look at the squeezing of quadratures. In general, if one measures for example the voltage, there will be uncertainties both in the measured magnitude and phase. These uncertainties manifests in the form of Gaussian noise around a certain average value. If we now plot these errors in magnitude and phase versus each other we get a circle [Figure 2.8 (a)]. According to quantum mechanics, conjugate variables are related to each other through the Heisenberg uncertainty relation. These means that it is possible to suppress (squeeze) the error in one observable below the standard quantum limit (where $\delta I = \delta Q$) at the cost of increasing it in the other observable. In this case, the field is in a squeezed state and the error circle changes to an ellipse [Figure 2.8 (b)].

If one measure the quadratures of the field, as we do in practice (see Chapter 3), the the squeezing of a single mode is defined as,

$$\sigma_1 = \frac{\langle I^2 \rangle - \langle Q^2 \rangle}{\langle I^2 \rangle + \langle Q^2 \rangle} \qquad (2.44)$$

where $\langle ... \rangle$ denotes the time average. In a two photons process like the DCE, it is natural to express the correlations of squeezing between two modes which is known as two-mode squeezing (TMS). Experimentally we measure four quadratures of the upper(I_+ and Q_+) and lower sidebands (I_- and Q_-) of the carrier frequency. TMS is the voltage-voltage correlations of the output fields and can be defined in terms of the quadratures as,

$$\sigma_2 = \frac{\langle I_+ I_- \rangle - \langle Q_+ Q_- \rangle}{P_{avg}} \qquad (2.45)$$

where P_{avg} is the total average power. TMS is a natural way to explore correlations in two photon processes. Theory predicts that if you measure the σ_1 of the lower or the upper sidebands, they are not squeezed, but if you look at cross-correlations between the lower and upper sidebands then, $\langle I_+ I_- \rangle = -\langle Q_+ Q_- \rangle$ if we choose the phase between the two modes such that $\langle I_+ Q_- \rangle = \langle I_- Q_+ \rangle$.

In Chapter 5, we discuss the experimental observation of the DCE and verify the signatures discussed here in the output radiations.

Chapter 3

Experimental Techniques

Microfabrication and measurement techniques have improved rapidly during the last decades. This has enabled us to build circuites with elements as small as few nanometers and study them in temperatures close to absolute zero, *i.e.* under conditions where they reveal quantum properties.

In this chapter, I briefly describe the main steps in fabrication of the samples and the working principle of our cryogenic and measurement systems. The detailed fabrication recipe can be found in Appendix I. The samples were fabricated in the Nanofabrication laboratory at Chalmers University of Technology.

3.1   Fabrication

The fabrication steps are similar but slightly different between SETs (samples in papers I-II) and SQUIDs and qubits (samples in papers III-IV-V). The common major steps include photolithography (for larger structures) and electron-beam lithography (for smaller structures).

The first step to write the larger structures with photolithography is to cover the wafer surface with a thin layer of photo-sensitive polymer (photo resist) [Figure 3.1(a)]. The next step is to expose the resist to UV light through a photomask which is a piece of glass covered with the desired pattern in chromium metal [Figure 3.1(b)]. The parts of the resist which are exposed to UV light will undergo chemical reactions and will be dissolved when emerged in a bath of the proper developer [Figure 3.1(c)]. Later, thin films of metal (trilayer of Ti,Au,Pd) will be deposited on these developed patterns using metal evaporators [Figure 3.1(e)].

In practice, we use two layers of photo resist on top of each other. The top layer resist as explained, is sensitive to UV light but the bottom layer is a liftoff layer which is not sensitive to UV but will nevertheless dissolve during the development, this creates an undercut profile [Figure 3.1(d)], which improves the liftoff process [Figure 3.1(f)].

The working principle of the e-beam lithography (EBL) is similar to the photolithography. The difference is that the special resist which is used is sensitive to
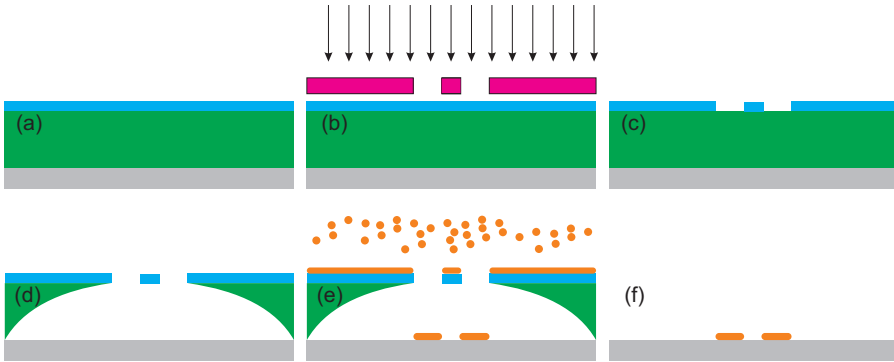
Figure 3.1: Different steps in photolithography : (a) The wafer is covered with resist layers. (b) Through a photomask, the resist layers will be exposed to UV light. (c) Development of the top layer in a proper developer reveals the pattern. (d) Developing the bottom layer produces an undercut profile. (e) Thin layers of metal are evaporated through the resist mask. (f) The final step is to remove the excess resist in a liftoff process.

electrons rather than to UV light. For EBL, the pattern will be written directly on the wafer and there is no photomask.

In the EBL machine, electrons are accelerated to energies as high as 100 keV before reaching the sample. These high energy electrons can partially back-scatter from the substrate and expose areas which are not parts of the pattern. This effect is called the *proximity effect* and limits the final resolution of the finest structures. To compensate for this, different parts of the patterns should receive different doses of the exposure. The small and isolated structures should receive higher doses whereas dense and large structures should receive lower dose. These adjustments are performed using a dose calculation software package (in our case ''PROXECO") for each individual pattern.

Another issue to take into account is the charging effect of the substrate. Since electrons are negatively charged, e-beam irradiation will charge the substrate. For relatively conductive substrates, like silicon this is not a problem since the accumulated charge will dissipate into ground through the wafer.

For insulating substrates, like sapphire, charge can accumulate in the substrate and deflect the e-beam resulting in pattern distortion. To overcome this problem, a thin layer of aluminium can be evaporated on top of the resist layer to dissipate the charge. This layer will be etched away after the e-beam and before the resist development. As an alternative, one can use commercial charge dissipation liquids which contain a conductive polymer on top of the resist (for example Espacer 300 Z is available in our cleanroom).

This charging effect can potentially cause another problem for fabricating charge-sensitive devices like SETs. The clusters of charge can form in the bulk of the insulating substrates. SETs are very charge sensitive and these charge clusters may affect
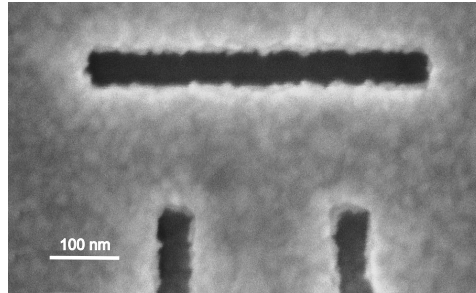
Figure 3.2: SEM image of the top layer resist after developing the bottom layer, without using Ge layer as hard mask. Here, 2 nm of gold is evaporated on the resist to make a conducting layer for taking the SEM image. The edge of the structures are not sharp and this will affect the final resolution.

their performance. We have studied this effect systematically as a master project (supervised by the author) [128], and found that in general, this effect is not pronounced for the usual doses we use for writing the SETs ($\sim 350\,\mu$C/cm^2) but when the dose has increased significantly ($\sim 3500\,\mu$C/cm^2), we could see an increase in the charge noise level measured by SETs. Due to statistical scattering in the results more measurements are required to draw any firm conclusions regarding this effect on fabrication of SETs and other charge-sensitive devices.

Although the EBL machine in our cleanroom (JEOL JBX-9300FS) can write patterns with dimensions down to ~ 10 nm, the final structure resolution is limited by other factors. One of these factors is that in the two layer resist system, the top layer will become wider while developing the bottom layer to make the undercut for the liftoff process (Figure 3.2). The solution for this problem will be to *transfer* the top layer pattern to another layer which is not sensitive to development before developing the bottom layer or to use fully selective developers. Another factor is the grain size of the aluminium [129].

We have used the former method and evaporated a thin layer of germanium ($\sim$ 20 nm) between the e-beam sensitive resist and the liftoff resist (in the case of an insulating substrate, this germanium layer acts as charge dissipation layer as well). After the trilayer system has been exposed to e-beam it will be developed. The only layer which is sensitive to e-beam irradiation is the top layer and the pattern will appear in this layer after the development. After that, this pattern will be transferred to the germanium layer by plasma etching (in this case we use CF$_4$ gas for etching). This means that, during the etching process, the uncovered parts on the top layer (the pattern) will be etched away. The key point here is that the etching rate of the top layer should be much slower than for the germanium layer. After etching, the development of the bottom layer can be done without degrading the resolution, since the pattern has already transferred to the germanium layer which is chemically
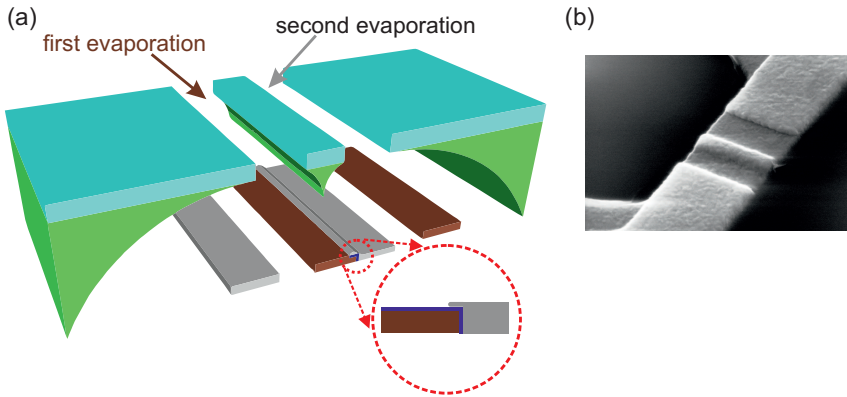
Figure 3.3: Two-angle evaporation method for fabrication of tunnel junctions : (a) The first layer of aluminium is evaporated at an angle, then without breaking the vacuum, a thin aluminium oxide layer will be formed on the surface of this layer by letting oxygen into the chamber. Finally, the second layer of aluminium is evaporated at an opposite angle (b) An SEM image of a tunnel junction made by this method

stable. This method is known as hard mask lithography and can result in very high resolution structures. We have used hard mask lithography for fabricating all the SETs measured in paper I and paper II. For SETs it is crucial to achieve the smallest junction size to increase their charging energy as explained in Chapter 2.

For fabrication of all of the samples presented in this thesis, we have used the double-angle evaporation method which was developed by Dolan in 1977 (Figure 3.3) [130]. First, the desired pattern is written by EBL using either a two or a three layer resist system. The first layer of metal (aluminium) is evaporated through the resist mask at an angle. The next step is to oxidize the surface of aluminium by letting oxygen into the chamber without breaking the vacuum. A thin layer of aluminium oxide will form and act as the insulating layer of the tunnel junctions. The thickness of this layer can be adjusted by tuning the oxidation pressure and time [131, 132]. The second layer of metal will be evaporated at an opposite angle. Finally, the last step will be to remove all the excess metal by liftoff. This is done simply by immersing the sample in a proper solvent which dissolves the bottom layer resist.

3.2   Cryogenics

Today many different cryogenic systems are commercially available and widely used in research labs. These systems exploit different methods and reach different base temperatures ranging from several K down to several μK. The measurements presented in this thesis are performed in ^{4}He/^{3}He dilution refrigerators.

The working principle of a dilution refrigerator relies on the fact that if a mixture of ^{4}He/^{3}He is cooled down to temperatures below ~ 800 mK it undergoes a phase

separation. Since ^{3}He atoms are lighter than ^{4}He, the ^{3}He rich phase stays on top (similar to phase separation in a mixture of oil and water). The key point is that the ^{4}He rich phase always contains 6.6% of ^{3}He even at the lowest temperatures.

If we start to pump on the ^{4}He rich phase, the lighter ^{3}He atoms evaporate first and disrupt the equilibrium. To compensate that, ^{3}He atoms migrate from the top to the bottom phase. This process is endothermic and if repeated in a continues cycle can effectively cool down the system to approximately 10 mK.

Figure 3.4 shows the picture from the two dilution refrigerators used in our measurements. The cooling insert and the sample will be placed inside a vacuum chamber. This vacuum chamber is called the inner vacuum chamber (IVC) and will be submerged in a ^{4}He bath. The ^{4}He bath will effectively cool down the system to 4.2 K and also together with a layer of a special thermal insulator ("super insulation") protect the IVC form room temperature thermal radiation.

In order to condense the mixture, it will pass through another stage, the 1 K pot. Here, by pumping on a small volume of ^{4}He which is drawn from the bath, the temperature of $\sim$1.5 K will be achieved which is enough for condensing the mixture. The condensed mixture will be accumulated in the mixing chamber where the phase separation happens. The ^{4}He rich phase of the mixture will extend through a tube to another chamber (the still). By heating on the still, ^{3}He atoms will be evaporated and pumped out and then injected to the system again to close the cooling cycle.

All the measurements in papers I-II were performed in a dilution refrigerator model TLE 200 from Oxford instruments ("Mr. Freeze") with a base temperature of $\sim$ 15 mK [Figure 3.4(a)]. Mr. Freeze is a top-loading refrigerator which means that the samples can be exchanged and mounted directly on the mixing chamber stage using a mounting stick, while the refrigerator is cold. This enables to exchange the samples without warming up the refrigerator to room temperature.

A 5-Tesla superconducting magnet is mounted on this refrigerator which applies a homogeneous magnetic field perpendicular to the surface of the sample substrate. Superconducting magnets (a coil with superconducting wire) are widely used in cryogenic systems since they do not dissipate heat. We have used this magnet to quench superconductivity in aluminium SETs measured in paper I-II. A resistor mounted on the mixing chamber acts as a heater while passing the current through it. This is used in paper I, during uniform temperature sweeps.

The measurements in papers III-V were performed in another dilution refrigerator from Oxford instruments model Kelvinox-400-HA with the base temperature of $\sim$ 30 mK ("Juliana"). This cryostat had a 2-T superconducting magnet and was equipped for microwave (MW) reflectometry measurements [Figure 3.4(b)].

Coaxial cables (with SMA connectors, specified from DC to 18 GHz) were used to transfer the MW signals via different temperature stages to the sample holder which was mounted on the mixing chamber. Careful choice of the cables for different temperature stages is crucial to reach the minimum base temperature of the cryostat and reduce the helium consumption. For example, it is useful (but expensive) to use superconducting cables (like niobium or niobium-titanium) reaching the stages with the lowest temperature (mixing chamber), since superconductors have very low
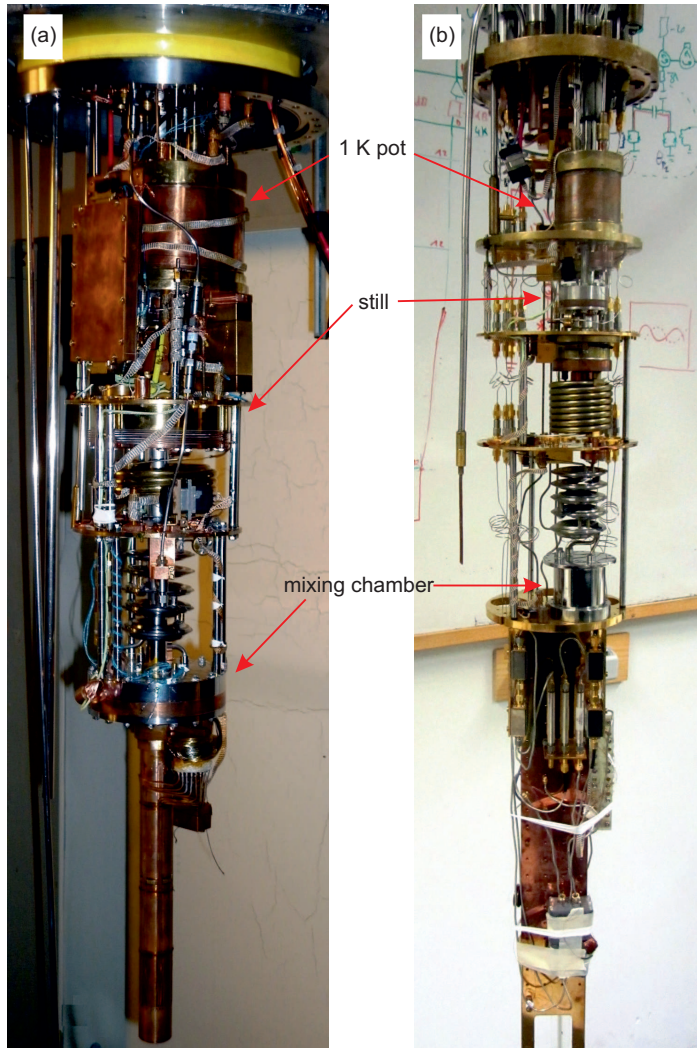
Figure 3.4:   Dilution refrigerator used in different measurements in this thesis: (a)
The refrigerator which was used in low-frequency measurements (Mr. Freeze). (b)
The refrigerator which was equipped with microwave setup and used for measure-
ment in paper III-V (Juliana)

losses and low thermal conductivity which can prevent the thermal leaks from higher temperature stages.

At each stage, the outer conductor of the cables were thermalized using feed throughs or signal attenuators. Substantial attenuation of the incoming signal to the sample reduces the thermal noise at different temperature stages (typically 60 dB in total). Also all the MW components used in the measurement setup were heat sunk to a proper temperature stage using copper wires, since it has a high thermal conductivity. Considering all these precautions, enables us to send MW signals which are generated from instruments in room temperature to the temperatures close to absolute zero and study their interactions with artificial atoms.

3.2.1 Low-frequency measurements setup

The low-frequency measurements in papers I-II were performed in Mr. Freeze [Figure 3.4 (a)]. The sample was mounted into the mixing chamber in a sample holder with spring-loaded pogo pins (Figure 3.6). This refrigerator is situated in an electromagnetic interference (EMI) shielded room and is heavily filtered with low-pas filters and powder filters [133, 134] in different stages making it an ideal choice for sensitive low-frequency measurements. In addition, to cancel out external noise, the measurement lines in the refrigerator were twisted in pairs.

Figure 3.5 shows the low-frequency measurement setup. All the measurements with SETs were performed in voltage-biased configuration. The SETs were biased symmetrically with respect to the ground through two home-built transimpededance amplifiers (TIAs) [135]. The current through the SETs were measured and amplified by these amplifiers differentially and a low-noise preamplifier (SIM-911) configured in differential mode was used to sum and post-amplify the output of TIAs. In order to reduce the external noise we used batteries to power the voltage sources and TIAs. Afterwards, the output signal was measured either by a data-acquisition card (National Instruments PXI-6259) or by a spectrum analyzer (Stanford Research Systems SR785) for noise measurements and by a digital voltmeter (Keithley-2001) for current-voltage characterizations.

3.2.2 Microwave reflectometry setup

The microwave reflectometry measurements in papers III-V were performed in Juliana. Here, the samples were wire bonded to a gold plated microwave printed circuit board (PCB) (Figure 3.6). We used gold bonding wires to have a high thermal conductivity in cryogenic temperatures between the chip and the sample holder which was mounted on the mixing chamber.

The basic requirements for MW reflectometry measurements are the MW source and the MW receiver. The source produces a signal which is sent towards the Device Under Test (DUT) and the response is received and analyzed by the receiver. Here I briefly discuss the general concepts in MW measurements. The MW measurement setups are slightly different and modified in different experiments and hence are described separately for each experiment in Chapter 5.
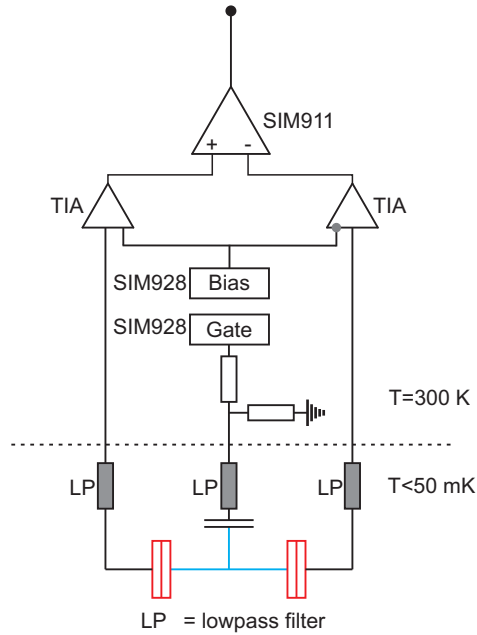
Figure 3.5: Simplified low-frequency measurements setup. The sample is mounted at the lowest temperature of the fridge and is connected to measurement instruments in room temperature with twisted pairs wires. The battery operated voltage sources, were used as gate and voltage bias sources. The current through the SET were measured differentially by two TIA and then another amplifier (SIM911) was used to sum and amplify the signal.

Vector network analyzer (VNA)

Microwave characterization measurements were performed using a vector network analyzer (VNA). The VNA is a complex and expensive piece of radio frequency test equipment. It is a two-port instrument consisting of a microwave source and a receiver which measures the magnitude and phase of the reflected or transmitted signal for DUT by measuring the scattering parameters (S-parameters) of the electrical network [74].

The source, generates the sinusoidal signal which is applied to the DUT. The response signal coming from the DUT, with different magnitude and phase, is measured by the receiver. The amplitude ratio of the reflected and the incident waves gives the magnitude of the S-parameters and the phase of the S-parameters is given by the phase difference between the wave quantities.

We have used a VNA model E8364B from Agilent Technologies in our measurements which had a measurement band from 10 MHz to 50 GHz.
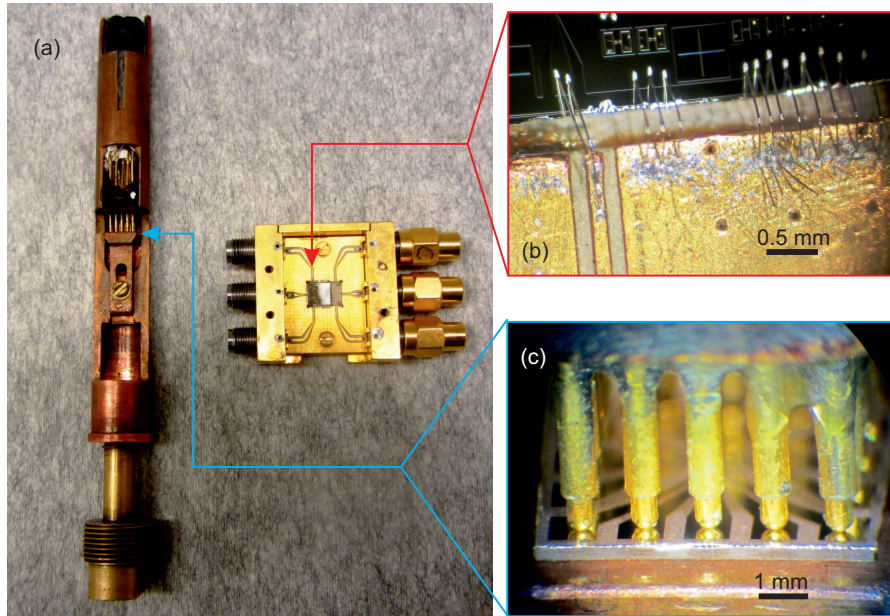
Figure 3.6: Sample holders and connections to chips : (a) Different kinds of sample holders were used for mounting samples in "Mr. Freeze" and "Juliana" cryostat. The left sample holder use pogo pin contacts to connect the measurement lines to the gold pads on the chip (b) and in the right sample holder which was used for microwave measurements, bonding wires were connecting the chip to a PCB.

MW sources and receivers

Another way to generate and measure the MW signals is to use separate instruments as source and receiver. In our case, MW frequency signals were generated either by using a MG3695B signal generator from Anritsu or by using the signal generator modules 3025 from Aeroflex. In both cases, phase coherent continuous waveforms were generated for spectroscopic measurements.

The transmitted or reflected signals coming from the sample, after several stages of amplification, were down converted and digitized by a digitizer module 3035 (or 3036) from Aeroflex. The physical sampling rate of MW digitizers are normally limited to 200 MS/s. This limits the bandwidth of these digitizers to frequencies much below the measurement band of our interest (4-8 GHz). The standard solution for measuring the signals with higher frequencies is to down-convert the incoming signal. The main working principle is to use a mixer (a nonlinear element which multiplies two incoming signals and creates signals with lower and higher frequencies) and mix (multiply) the incoming signal with frequency of $\omega_s/2\pi$, with a signal coming from a local oscillator (LO) with a known oscillation frequency $\omega_{LO}/2\pi$. Using the basic trigonometry we find,

$$\underbrace{A\cos(\omega_s t + \phi)}_{\text{incoming signal}} \times A\underbrace{\cos(\omega_{LO})}_{\text{LO signal}} = \frac{1}{2}A[\cos([\omega_s - \omega_{LO}]t + \phi) + \cos([\omega_s + \omega_{LO}]t + \phi].$$

$$(3.1)$$

The case where $\omega_{LO} = \omega_s$ is referred to as homodyne detection and the cases which $\omega_{LO} \neq \omega_s$ is referred to as heterodyne detection. The digitizers we used to down convert the signal were working in a heterodyne detection scheme. They also use a special type of mixers known as IQ-mixers which allow them to detect the signal decomposed in its quadratures.

I-Q **Quadrature**

An effective way to transfer information in telecommunications is to modulate the frequency (FM) or amplitude (AM) of a sinusoidal waveform (carrier signal). For a carrier signal with amplitude, A, frequency, f, and phase, ϕ, using simple trigonometry we find,

$$A\cos(2\pi ft + \phi) = A\cos(\phi)\cos(2\pi ft) - A\sin(\phi)\sin(2\pi ft). \qquad (3.2)$$

Now if we define $I = A\cos(\phi)$ and $Q = A\sin(\phi)$, we can alternatively express the signal in terms of these I and Q quadratures (I-Q representation). Amplitude and phase of the carrier signal can be recovered by measuring the I and Q quadratures as,

$$A = \sqrt{I^2 + Q^2} \qquad \text{and} \qquad \phi = tan^{-1}\left(\frac{I}{Q}\right). \qquad (3.3)$$

Amplitude-phase representation and the I-Q representation of the waveform carry the same information and can be interpreted as the transformation from the polar coordinate system (amplitude-phase) to the Cartesian coordinate system (I-Q).

Noise temperature

The quantum properties of atom-light interaction are revealed at power levels corresponding to one or a few single photons per interaction time. For microwave photons, this requires heavy attenuation of the incoming field before reaching the sample. Subsequently, the response signal from the device (reflected or transmitted) is very weak and needs to be amplified in different stages with a chain of amplifiers before reaching the receivers at room temperaturer.

It is very crucial to characterize the noise properties of the system for such low power measurements. The important measure, is the signal-to-noise ratio (SNR) which compares the level of signal to the level of noise and depends on the total noise temperature of the system, $T_n = P_n/k_B\,RBW$, where P_n is the noise power in units of Watts and RBW is the resolution bandwidth (the smallest frequency that can be resolved in the measurement). The most reliable technique to determine T_n

is to use shot noise thermometry [136]. We have characterized a measurement setup very similar to ours using shot noise thermometry and found $T_n \simeq 7K$ [105].

When a chain of amplifiers are used to amplify the signal, then the total noise temperature is

$$T_n = T_{amp,1} + T_{amp,2}/G_1 + T_{amp,3}/G_1 \, G_2 + ...,\qquad(3.4)$$

where $T_{amp,i}$ and G_i are the noise temperature and gain of the i'th amplifier respectively. This implies that T_n is mainly governed by the noise temperature of the first amplifier. In our measurement setup the first amplification stage is a low-noise amplifier (LNA) from Low Noise Factory (model LNF-LNC4-8A) mounted at 4 K stage with the noise temperature of ~4 K (and ~2 K for a newer version) for a bandwidth of 4-8 GHz.

Chapter 4

Results: Probing Two-Level Fluctuators

General properties of SETs and their noise sources are discussed in Chapter 2. In order to investigate the properties of low-frequency charge noise and TLFs we have performed extensive measurements with SETs. The experiments presented in this chapter are performed in collaboration with another PhD student Martin Gustafsson. In our experiments, we have used SETs as sensitive electrometers to study the properties of TLFs.

In the first section of this Chapter, we describe experiments where TLFs are studied under equilibrium conditions. We study the charge noise measured by the SETs under different bias conditions and temperatures. Assuming that this noise is generated from an ensemble of TLFs, we can draw conclusions regarding the activation mechanisms and thermal properties of the TLFs ensemble. The results of the experiments discussed in this Section are published in paper I.

In the second Section, we describe experiments where we push the TLFs out of equilibrium by application of a strong external electric field and study their relaxation process using SETs. The results of these experiments are presented in paper II.

4.1 Equilibrium properties of TLFs: Temperature dependence of noise

Bias and temperature dependence of the charge noise have been already measured by different groups [49, 56, 57, 41, 137]. Although the general conclusions are that charge noise is increasing with increasing bias voltage and temperature, generally it has been difficult to draw firm conclusions due to the scattering in the data points. In paper I, we have measured the charge noise with SETs with relatively high charging energies at many different bias points and at many different temperatures.

The aluminium SETs were made on silicon substrates covered with 400 nm of SiO_2 using the standard double-angle evaporation method explained in Chapter 3.

The samples were cooled down in a dilution refrigerator to $\sim$ 20 mK and the superconductivity in aluminium devices was quenched by applying a 1 T (or 600 mT in some of the measurements) magnetic field.

The SETs were voltage biased in a measurement setup similar to the setup which is explained in Section 3.2.1. The current noise in these measurements is acquired with a spectrum analyzer (SR785) for frequencies from 1 Hz to 401 Hz. Each spectrum was averaged 250 times in the spectrum analyzer and the final averaged trace was transferred to a control computer for post-processing. A "pilot" signal at a frequency of $f_p = 377$ Hz was applied to the gate together with the DC gate voltage. The amplitude of this pilot signal was a known fraction of the gate period which is equivalent of one electron charge induced on the island. The measured current noise spectrum was translated to the equivalent charge noise spectrum, by normalizing to this pilot signal level. We report a single value, $\tilde{S}_Q$, as the charge noise level of each spectrum by averaging the charge noise spectrum between 381 Hz to 401 Hz.

In the first set of measurements, we measured the charge noise of the SETs continuously, while increasing the cryostat temperature T_0 gradually using a resistor heater mounted close to the mixing chamber of the cryostat. Each temperature sweep from 20 mK to 4 K took about 20 hours. As the temperature increases the thermal energy of electrons become large enough to overcome the Coulomb blockade (see Section 2). This decreases the difference in current between the open and the close state of the SET *i.e.* the modulation of the charge transfer function. Thus, for these measurements the SETs were biased in such way that the charge transfer function modulation was maximum at the base temperature (this optimal bias point is the threshold bias voltage to observe Coulomb blockade in the device) [blue dot in Figure 4.1(a)].

The measured charge noise level strongly depends on the charge sensitivity of the SET, dI/dQ_g [138]. For I_{max} [red dot in the inset of Figure 4.1(a)] and I_{min} [blue dot in the inset of Figure 4.1(a)], the charge sensitivity is minimum and for the highest slope of the transfer function [cross in the inset of Figure 4.1(a)] the charge sensitivity is maximum, which is the optimal point to exploit the SET as the electrometer. In practice, during this experiment for each temperature point we did a gate sweep over several periods to find I_{max} and I_{min} and then tuned the gate voltage to have the optimal current, I_{opt}, as the average of I_{max} and I_{min}.

Figure 4.2 shows the temperature dependence of the charge noise measured for two different samples (S1 with E_c/k_B = 10.6 K and S2 with E_c/k_B = 6.0 K). Here, we have measured the charge noise for about 200 different temperature points (in comparison with all the previous reports which had maximum $\sim$ 15 temperature points). We found that for higher temperatures, the charge noise increases linearly with the cryostat temperature. This result is in sharp contrast with some of the previous reports of T^2-dependence of the charge noise [57, 56]. Similar to other reports, we also found that at lower temperatures, around 300 mK, charge noise saturates and become temperature independent [41, 49, 137, 51, 56, 40, 57].

This saturation can not be explained by the "standard model" which assumes charge noise originates from the thermally activated TLFs with uniform distribution of barrier heights. In this case, as temperature decreases the thermally activated
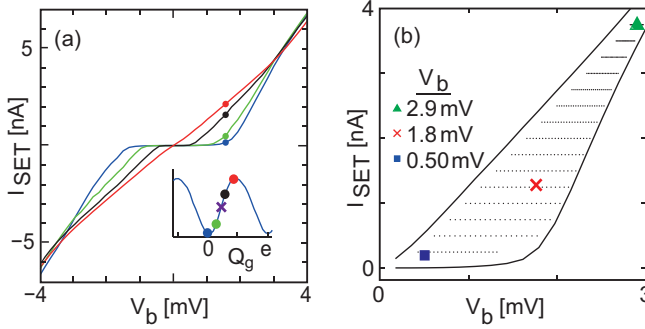
Figure 4.1:   Characterisations of a SET measured in paper I (device S1). (a) *I-V* characteristics for different gate voltages. The inset shows the charge-transfer function of the SET *i.e.* I_{SET} as a function of Q_g. The blue and the red dot represent the situations where the minimum and the maximum current pass through the SET respectively and the cross shows the optimal working point, where the charge sensitivity of the SET is maximum. (b) Solid lines : *I-V* characteristics of device S1 for blockade and open state of the SET. The dots represents about 300 points with different values of V_b and I_{SET} which were used to measure the charge noise as a function of the power dissipated in the SET. The square, triangle and the cross are the different bias points which were used to measure the bias dependence of the saturation temperature (see text).

TLFs will ''freeze out". This means that, assuming the charged particle in the TLF is in thermal equilibrium with the environment, at lower temperatures it can not gain enough thermal energy to fluctuate between TLF states. For a uniform distribution of barrier heights, this reduces the number of effective TLFs at lower temperatures and subsequently the charge noise should approach zero at zero temperature.

The origin of this saturation in charge noise is not completely known although different mechanisms have been suggested:

- The first scenario assumes that noise is generated by TLFs residing in or close to the tunnel junctions. In this case, the transport electrons flowing through the junctions with energy of eV_b, are assumed to inelastically scatter the TLFs and activate them [56].

- The second possibility is that the current passing through the SET, generates heat which will dissipate in the island electron gas and the substrate. If the SET bias voltage is V_b, then the power dissipated in the device is $P_{SET} = V_b I_{SET}/2$. This process is known as the self-heating of the SET and results in the elevated temperature of the SET, even at the base temperature of the cryostat [139].

We performed a second experiment to check if the saturation temperature depends on the bias voltage. In this experiment, we repeated the temperature sweep for
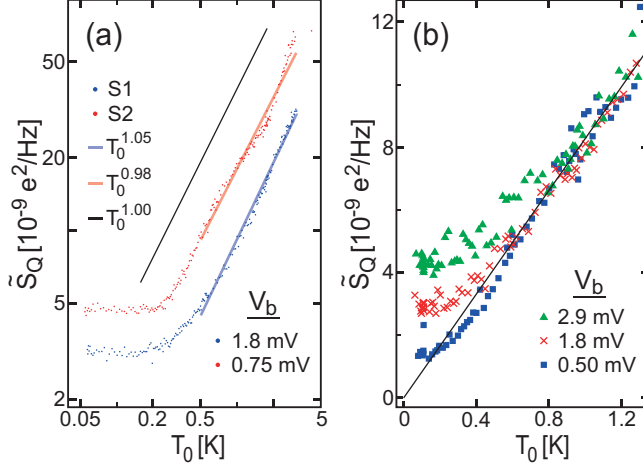
Figure 4.2: Temperature dependence of the charge noise : (a) Measurements of $\tilde{S}_Q$ for device S1 (blue dots) and S2 (red dots), as a function of the cryostat temperature, T_0, and in a fixed bias voltage. The solid blue and red lines are the linear fits in the logarithmic plot for $T_0 > 0.5$ K for S1 and S2 respectively and the solid black line is showing the linear temperature dependence. (b) Temperature dependence of the charge noise for device S1 while alternating the bias point between 3 different values. The bias point symbols corresponds to those in Figure 4.1(b). The black solid line is a linear fit for $T_0 > 1$ K constrained to pass through the zero.

device S1 while alternating the bias point between three different bias values. These bias values are marked in Figure 4.1(b) as square, cross and triangle. Figure 4.2(b) shows the result of this experiment. It is clear that at higher temperatures, the charge noise scales linearly as $\tilde{S}_Q = \beta T_0$, independent of the bias point. At lower temperatures, $\tilde{S}_Q$, saturates to a level which strongly depends on the bias value. We refer to this saturation temperature (intersect of the horizontal line through the saturation level of the noise and $\tilde{S}_Q = \beta T_0$), as T_{TLF}, the temperature of the TLF ensemble. At higher temperatures, the noise level is higher because the TLF ensemble is warmer and consequently more active but when the cryostat gets colder, the noise level stops decreasing at T_{TLF}, because the TLFs remain at temperature T_{TLF} and do not get colder.

The fact that the bias dependence is valid only to temperatures around 600 mK suggests that the inelastic scattering of transport electrons can not explain the noise saturation. Transport electrons with energy of eV_b, activate more TLFs as V_b increases, but we see that this bias dependence disappears at the temperatures much lower than $eV_b/k_B \sim 11$ K [Figure 4.2(b)]. Thus, our data speaks against the first scenario and agrees more with the self-heating scenario.

To investigate this bias dependence further, we performed the third experiment. Here, for sample S1 we measured the charge noise at base temperature for ~ 300 bias points with different values of V_b and I_{SET}. These points are shown with small dots
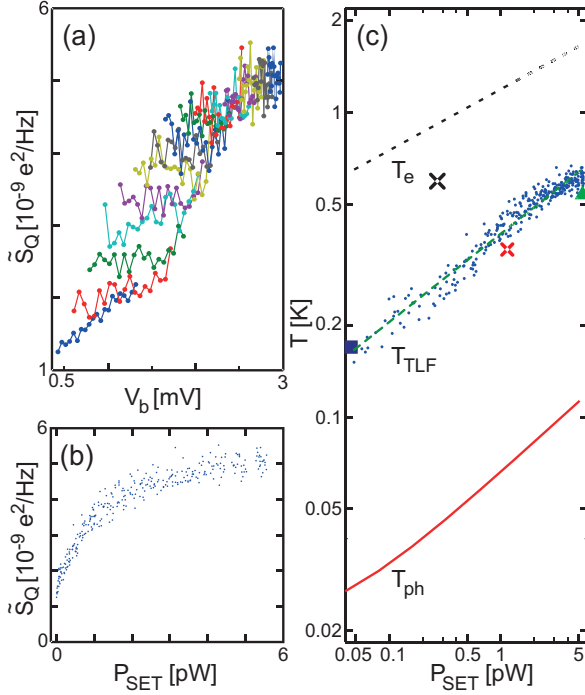
Figure 4.3: Bias and power dependence of the charge noise for device S1 at cryostat base temperature. (a) Measurements of $\tilde{S}_Q$ for different points in Figure 4.1(b). Here, the bias points with equal I_{SET} are connected together with solid lines. Charge noise increases with increasing the bias voltage and the current passing through the SET. (b) The same data in (a) plotted as a function of the power dissipated in the SET, $P_{SET} = V_b I_{SET}/2$. (c) Blue points show the extracted TLFs temperature as a function of the P_{SET} and the green dashed line is the fit to the logarithmic plot. Square, cross and triangle are the saturation temperatures extracted from Figure 4.2(b). Solid red line represents phonon temperatures underneath the SET, obtained from the finite element calculations. The black dashed line is the calculated SET electron gas temperature from the electron-phonon thermalization theory and the black cross shows the electron temperature extracted from the temperature dependence of the I_{min} and I_{max} (see text).

in Figure 4.1(b). The total measurement took about 13 hours and the result is shown in Figure 4.3(a). Data points with the same I_{SET} are connected to each other with solid lines. It is clear that the charge noise increases with increasing both the bias value and the current through the SET. In Figure 4.3(b) we have plotted the charge noise for each individual measurement point as a function of the power dissipated in the SET, P_{SET}. We see that the charge noise, increases with increasing the dissipated power in the SET. Figure 4.3(c) shows the extracted saturation temperatures,

T_{TLF}, for each individual point as a function of the power dissipated in the SET on a logarithmic scale where we used the β obtained from the previous measurement. The square, cross and triangle are corresponding T_{TLF} extracted from Figure 4.3(b).

The next step was to calculate the temperature of the electron gas in the SET, T_e, and compare it with T_{TLF}. The power dissipation in the SETs and similar devices is well studied by other groups [140, 141, 142, 143, 144]. If the power P_{SET} uniformly dissipates in the SET in a volume of Ω then, electrons reach a steady-state temperature T_e,

$$T_e = (\frac{P_{SET}}{\Sigma \, \Omega} + T_{ph}^5)^{1/5} \tag{4.1}$$

where Σ is a parameter involving the electron-phonon coupling and T_{ph} is the phonon temperature underneath the SET [144]. The black dashed line in Figure 4.3(c) shows the calculated T_e as a function of the dissipated power assuming $T_{ph} \simeq T_0$. The parameter Σ depends on the material properties and we have used $\Sigma = 0.4 \times 10^9 \, \mathrm{W \, K^{-5} \, m^{-3}}$ as suggested for aluminium [141].

We can extract T_e in another way as well to compare it with the theoretical values. As explained before, both values of I_{max} and I_{min} depends on the electron temperature. The standard theory model for SETs (orthodox theory) predicts this temperature dependence [145]. By fitting the theory model to the measured values of I_{min} and I_{max} at different temperatures (see Figure 5 in paper I), we find that as the cryostat temperature decreases, I_{min} saturates to a value I_{sat}, which is much higher than the values predicted from the theory. This can be interpreted as a higher temperature of the electrons due to the self heating. We extract the electron temperature of $T_e \sim 0.59$ K from the crossover of the theory and the experimental I_{min} curve (Figure 5.(b) in paper I). This data point is shown with a cross in Figure 4.3(c) for the corresponding power of $P_{SET} = V_b \, I_{sat}/2$. The two methods, predict the electron temperature rather close to each other and the difference between them stems from the uncertainties in the parameters of the theoretical model.

Sofar we have assumed that $T_{ph} \simeq T_0$, which is due to the weak electron-phonon coupling at cryogenic temperatures [142, 143, 144]. However, using finite element method we can estimate the phonon temperature underneath the SET island and compare it with T_{TLF}. In our finite element model, we approximate the SET with a disk with the same as the real device and assume that the dissipated power, is emitted as phonos from the aluminium electrode to the SiO_2 layer underneath (for the details of the model see [146]). The calculated phonon temperature underneath the SET island is plotted as the red solid line in Figure 4.3(c), where we have assumed T_0 = 20 mK and used the reported values in the literature for the thermal conductivity of Si and SiO_2 [147, 148]. The calculated T_{ph} is 5-6 times lower than the electron temperature on the island, confirming the weak electron-phonon coupling.

By comparing T_{TLF} with T_e and T_{ph} in Figure 4.3(c), we find that, phonons temperature underneath the island is 5-6 times lower than the T_{TLF}, where as the electron temperature is 2-3 times higher than T_{TLF}. This suggests that the phonon temperature is too low to explain the elevated temperature of the TLFs and that the TLFs are in stronger thermal contact with the electrons rather than with the phonons.

Relating this result to the microscopic models suggested for the TLFs, we can argue that the TLFs with double-well potential residing in the bulk of the substrate cannot thermalize with the electrons on the SET island [48]. On the other hand, models which assume tunneling of the electrons between the SET island and the local states agree well with the thermal properties of TLFs and result in a T_{TLF} slightly lower than the electron temperature since electrons tunnel back and forth between the hot island and the colder localized state.

As mentioned in Chapter 2, different models suggest the TLFs location as local states within tunneling distance from the SET island. For example they can be stray aluminium grains which form during the fabrication of the SETs [53, 54]. Another possibility is the localized metal-induced gap states (MIGS) [149, 150]. Localized MIGS, in the interface of the metal and the substrate, have already been suggested for the origin of the flux noise in the flux-sensitive devices like SQUIDs [151].

4.2 Non-equilibrium probing of TLFs: Step response

In paper II, we have measured the response of the TLF ensemble to a large external electric field. The measurement protocol is rather simple; first we let the system reaches its equilibrium condition. We allow around 24 hours waiting time between two consecutive measurements. Then, we apply a voltage step to the gate electrode abruptly, and measure the following charge drift caused by the relaxation of the TLFs, exploiting the unique charge sensitivity of the SET.

If one applies a voltage step of ΔV, to the SET gate, the response of an SET residing on an ideal dielectric (by ideal we mean in the absence of a TLF ensemble) will be that the initial working point of the SET will be shifted by $\Delta V/(e/C_g)$ periods, since (as explained in Section 2.2) each period of the charge-transfer function is equal to e/C_g [Figure 4.4(a)]. In reality, there is also another effect on top of this ideal response. The gate voltage step will change the potential landscape of the TLFs [Figure 4.4(b)]. Charged particles in the TLFs will decay to their new ground state after some characteristic time and cause a charge drift, $Q(t)$, in the nearby SET [Figure 4.4(c)]. Measuring $Q(t)$ can give information regarding the densities and the distribution of the ensemble of TLFs causing the drift. This information can not be obtained from the equilibrium measurements of the TLFs.

We have shown in Section 2.4.4, that by starting from the charge induced on the SET island due to the switching of an individual TLF [Eq. (2.11)], we can find $Q(t)$, the total charge drift from an ensemble of TLFs, by adding the effects from the individual TLFs [Eq. (2.14)]. In this section, we present experimental measurements of $Q(t)$ and compare it with the theory.

For these measurements, aluminium SETs with nominally identical design (and similar to the SET design used in previous experiments) were fabricated on different substrate materials ; silicon covered with $\sim$400 nm of SiO$_2$ (refered to as silicon substrate), 500 μm thick borosilicate Pyrex-glass (refered to as glass substrate) and single crystal, R-oriented, 330 μm thick sapphire (refered to as sapphire substrate).

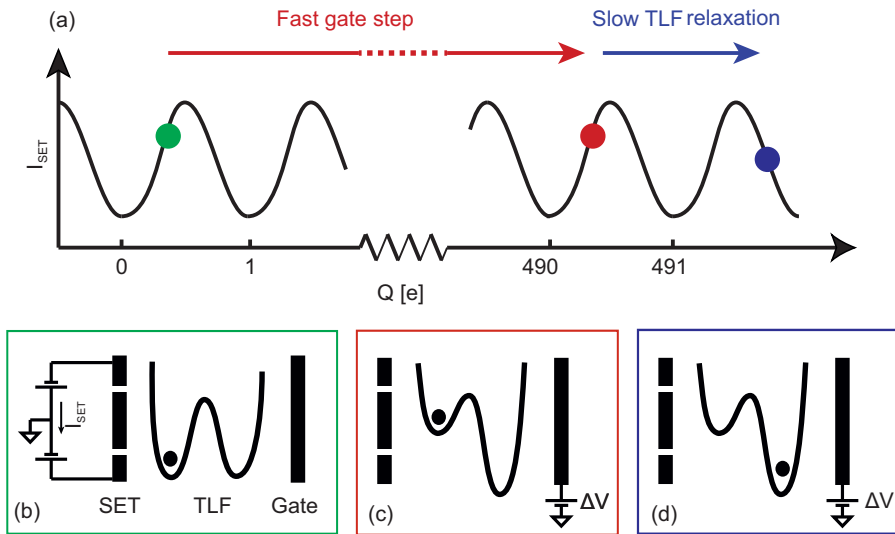Figure 4.4: Schematic protocol of the measurements. (a,b) First we let the system to reach the equilibrium state (green). Then, applying a sudden voltage step of ΔV to the gate electrode, pushes the TLFs far out of equilibrium (red). After the step, the TLF ensemble relax to a new ground state. This charge reconfiguration, causes a background charge drift which we measure using a SET (blue).

In the first batch of measurements we use a similar measurement set up as in previous Section. Here, we tune the gate voltage to the optimal operation point and sample the SET current, I_{SET}, continuously with sampling frequency of $f_s = 2$ kS/s. At a specific time (which we define as $t = 0$), we apply a sudden voltage step to the gate electrode. Consequently, the operation point moves by hundreds of periods abruptly. We can not capture these fast oscillations (response of the dielectric) with our measurement set up, but we can measure the additional slow response of the TLFs. Figure 4.5 shows $I_{SET}(t)$ after a voltage step of $\Delta V = 9.8V$ for a sample on silicon substrate (device #1 in paper II) at 30 mK. From this data, we can extract $Q(t)$, by counting the number of the oscillations in the transfer function, since each of them corresponds to one electron charge induced on the SET island. Figure 4.5(b) shows the extracted $Q(t)$ and the inset represents the same data using a logarithmic x-axis. It is clear that the drift increases logarithmically in time over several decades of time.

In the second batch of the measurements, we used a PID (proportional-integral-derivative) regulator to measure the $Q(t)$ directly rather than from counting the oscillations of I_{SET}. The PID was connected to the gate and set to maintain an optimal I_{SET}. The error signal was digitized and measured using a data-acquisition card. This error signal is equal to $Q(t)$ when normalized to the gate period. Figure 4.6 shows an example of such a measurement of $Q(t)$ for $\Delta V = 9$ V, for a SET on silicon substrate for $\sim$20 hours. The inset shows the first 10 seconds after the voltage step is applied. These high resolution measurements of $Q(t)$ enable us to study the drift on different time scales. On one hand, we can extract the logarithmic increase of $Q(t)$ by observing the $Q(t)$ trend for many hours and on the other hand, we can resolve the step-like behaviour of the drift on much shorter time scales (Figure 4.6 inset), which can be attributed to the individual switching events of TLFs.

We repeated this measurement for different devices made on different substrates and for different values of ΔV and observed the logarithmic increase of drift in all of them (Figure 3 in paper II). From measurements of $Q(t)$, we extract the parameter H which is the logarithmic slope of the charge drift normalized to the voltage step, ΔV,

$$H = \frac{1}{\Delta V} \frac{\Delta Q(t)}{\Delta \log t}. \tag{4.2}$$

Studying this logarithmic slope H, rather than $Q(t)$, is a better way to monitor the drift, since the PID regulator is perturbed after the step, and we cannot capture the first few seconds of the drift. Table I in paper II, summarizes the measurements of H for different devices. We note that the values of H are fairly similar for different devices. Also different measurements on device #1 at 30 mK and at 2000 mK shows rather similar values of H, indicating that the drift is not temperature dependent.

The fact that $Q(t)$ is not temperature dependent, suggests that the charged particle in the TLF is moving between wells by quantum tunneling rather than by the thermal activation : In the case of thermally activated TLFs, the switching time, τ, is determined by Eq. 2.9. We naturally assume that the barrier heights (activation
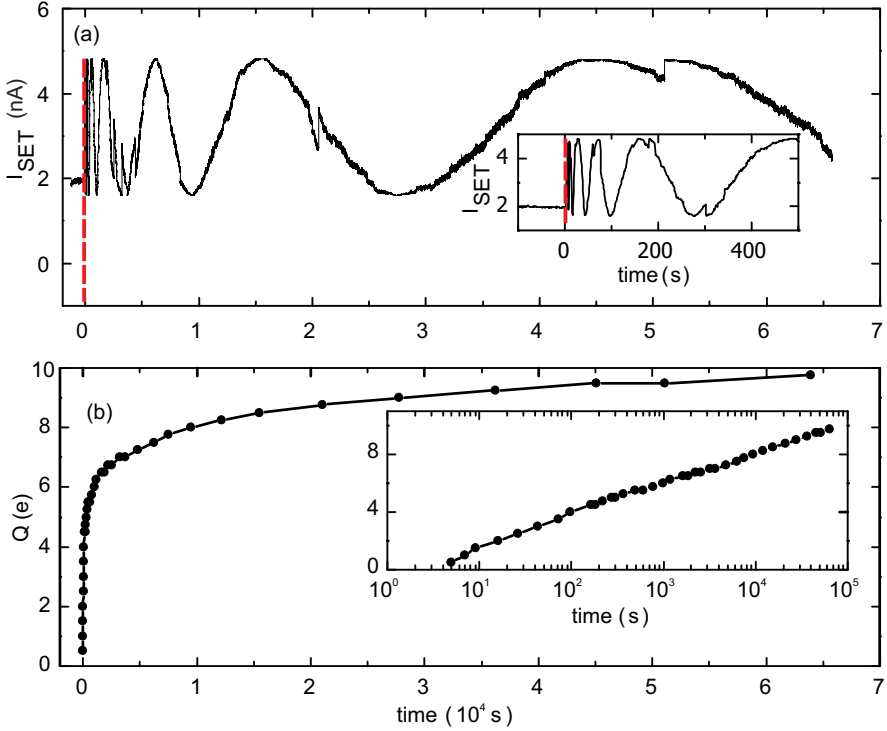
Figure 4.5:   Response of a SET (device #1 in paper II) to a 9.8 V voltage step at 30 mK. (a) I_{SET}(t) is measured for about 20 hours. The voltage step is applied at t = 0 (red dashed line). The inset shows the first 500 seconds after the voltage step. (b) Charge drift extracted from the oscillations of current in (a). The inset shows the same data in the logarithmic time scale. The charge increases logarithmically over four decades of time.

energies) and the attempt rates are temperature independent. Increasing the temperature, for a flat distribution of barrier heights, results in increasing the number of TLFs per decade. So in the case of the thermally activated TLFs the number of TLFs per decade and consequently the $Q(t)$ should increase linearly with increasing the temperate.

To study the drift further, in separate measurements, we applied voltage steps with different ΔV to the gate electrode of a SET made on glass substrate and measured the charge drift. We found that the logarithmic slope of the drift is proportional to ΔV (Figure 4 in paper II). This justifies why we report values of the logarithmic slope normalized to the step height.

Tracing the charge drift due to its logarithmic behaviour, requires very long measurements. On top of that, the system should reach its equilibrium state before starting a new measurement. These factors make these measurements very time consum-
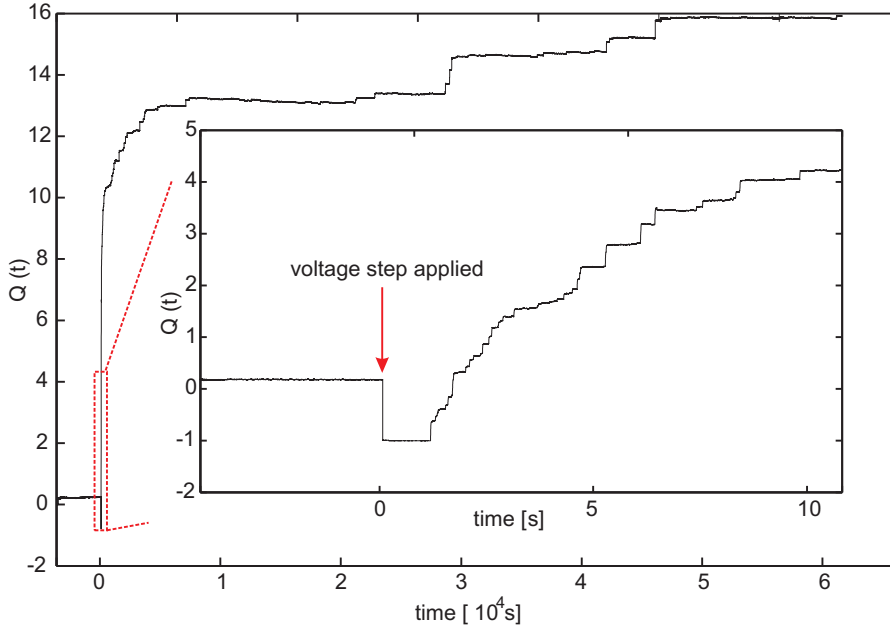
Figure 4.6: Measurement of the charge drift, $Q(t)$, using a PID regulator connected to the gate electrode for a sample on silicon substrate at 30 mK and for a 9 V voltage step. The arrow shows when the voltage step is applied and the drift is started. We measure the charge drift for about 20 hours. The inset shows the first 15 seconds after the voltage step is applied. The PID is perturbed for the first couple of seconds after the voltage step (plateau after the arrow in the inset), and we can not measure the drift during the first seconds.

ing.

To overcome this limitation, we also performed another type of measurements in which, we applied a periodic square-wave voltage signal to the gate and measured $Q(t)$ using the PID regulator as before, for the intervals of one hour (Figure 4.7). Starting from $V_g = 0$, while continuously monitoring the drift, after some waiting time we applied a voltage step of $\Delta V = 4.5$ V to the gate. After one hour, we applied a 9 V step from +4.5 V to -4.5 V and after measuring the drift for another hour we applied another 9 V voltage step from -4.5 V to +4.5 V and so on. We repeated this cycle, for about 20 hours by applying the voltage steps of 9 V in the opposite directions every hour [Figure 4.7(a)]. Afterwards, we treated each of these 9 V voltage steps as an individual measurements of $Q(t)$ for one hour. In this way, we have 20 different step response measurements to study separately or average them together. Figure 4.7(b) shows 8 different traces for voltage steps from -4.5 V to +4.5 V in black and their averaged trace in green (the averaged trace has been offset for clarity). Although these measurement of $Q(t)$ in shorter time scales, also showed the
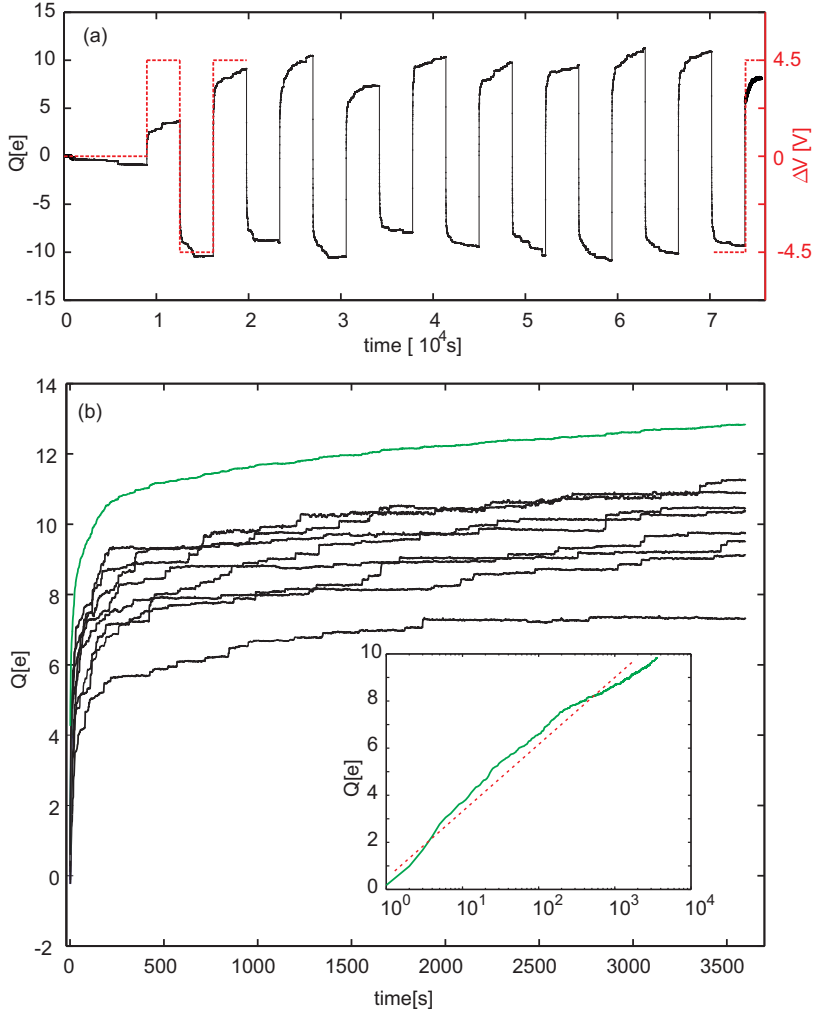
Figure 4.7: Continuous measurements of $Q(t)$ while applying a square-wave voltage signal to the gate electrode for a sample on silicon (device #1 in paper II) at about 1.4 K. (a) A square-wave voltage signal with $\Delta V = 9$ V is applied to the gate electrode with the intervals of one hour. The right (red) axis shows the first and the last cycles of the voltage step. (b) By treating each voltage step in (a) as an individual measurement of $Q(t)$ for one hour (here we have plotted only $Q(t)$ for steps from -4.5 V to +4.5 V), we can average them together (green trace) which has been offset for clarity. The inset shows the averaged trace in the logarithmic time scale. The red dashed line is the linear fit in the logarithmic plot resulting in slope of 2.8 (e/decade of time) which corresponds to $H = 0.29$ when normalized to ΔV.

logarithmic increase of drift but, since the system has not reached the equilibrium state before applying each voltage step, they do not follow our general measurement protocol and hence we decided not to reported them in paper II and use them more as a control experiment.

4.3   Conclusions and outlook

We have performed extensive studies of TLFs using SETs as sensitive electrometers. Measurements of TLFs in equilibrium and non-equilibrium conditions revealed complementary and consistent information about them. In our measurements, we used SETs made on different substrates to study TLFs at different temperatures, different bias values and different external fields. Detailed analysis of our data and comparing it with the theory, allow us to draw the following conclusions regarding the charge noise and the TLFs:

- We have studied the thermal properties of charge noise and TLFs and found that at higher temperatures charge noise increases linearly with temperature but at lower temperatures, it saturates to a level which depends on the bias voltage applied to the SET. The dependence of this saturation level on the power dissipated in the device, suggests that it is due to the self heating of the SET.

- We estimate the TLF ensemble temperature from our measurements and compare it with phonon temperatures underneath the SET and electron gas temperature in the SET island. We find that the TLF ensemble temperature is approximately 2-3 times lower than the electron temperatures on the island and 5-6 times higher than the phonons. We conclude that TLFs have to be in thermal contact with the hot electron gas on the island.

- Our data agrees with the TLF microscopic model where noise is generated by tunneling of electrons between the SET island and the local surface states like MIGs.

- Applying a strong external electric field to the TLFs, drive them far out of equilibrium. Subsequent relaxation of TLFs to a new ground state causes a charge drift, which we have measured using SETs for more than four decades of time. This response is logarithmic in time and in agreement with the response expected from an ensemble of TLFs.

- We observed that the logarithmic slope of the drift increases with increasing the voltage step height, but does not depend significantly on the temperature. Both of these observations indicate that the charged particle in the TLF fluctuates by quantum tunneling rather by thermal activation.

- We extract the logarithmic slope of this drift and by comparing it to the simple theory which we develop, we are able to find the densities of TLFs assuming that they are distributed homogeneously on the surface or in the bulk with

the densities n_s and n_v, respectively. We estimate $n_v \approx 1.5 \times 10^{24}$ (m^3 eV decade)$^{-1}$ and $n_s \approx 1.6 \times 10^{16}$ (m^2 eV decade)$^{-1}$.

In order to find more missing pieces of this puzzle, extensive systematic measurements are required. Non-equilibrium probing of TLFs suggests a new way to study charge noise sources and can be exploited in different systems and for different materials. For example, all of the devices we have measured here, were made of aluminium and it can be beneficial to study devices with different material properties and compare the result. Another interesting experiment will be to observe the step response of a suspended SET [51]. In this case the TLFs in the bulk of the substrate can not affect the SET, and the step response can solely be interpreted as the response of the surface TLFs. Also designing samples with simpler geometries will improve the interpretation of the results. Another aspect is to use advanced microscopic methods to study the tunnel junctions and the interfaces can shed light to the microscopic origin and location of TLFs [152].

Chapter 5

Results: Probing Vacuum Fluctuations

Vacuum fluctuations and their properties were discussed in Chapter 2. We described that the vacuum fluctuations originate from the quantum mechanical nature of the electromagnetic field and have measurable consequences. We have performed experiments in the context of circuit QED, to probe these vacuum fluctuations and their interactions with boundary conditions and artificial atoms made from superconducting circuits.

In the first part of this Chapter, we explain the observation of the dynamical Casimir effect (DCE) in a superconducting circuit. This experiment, is the first experimental observation of the DCE, almost 40 years after its theoretical prediction by Moore [18]. In the second part of this Chapter, we probe the vacuum fluctuations by exploring the relaxation process of an artificial atom in front of a mirror since the spontaneous relaxation process is a consequence of the atom interacting with vacuum fluctuations. Finally, in the last part of this Chapter we present preliminary results for characterization of a system consisting of two atoms in front of a mirror.

5.1 Observation of the dynamical Casimir effect

The theory proposal of Johansson *et al.* to observe the DCE in the circuit QED was already discussed in Section 2.8 [125, 126]. Here, we investigate this proposal experimentally. To do so, two aluminium devices, S1 [Figure 5.1(a)] and S2 [Figure 5.1(b)], were made on silicon substrates covered with 400 nm of thermally grown SiO_2. The fabrication process includes e-beam lithography with two layers of resist and double angle evaporation of the tunnel junctions as was explained in Chapter 3.

The sample design consists of a SQUID at the end of a coplanar waveguide (CPW) transmission line (Figure 5.1). The length of the transmission line was different in S1 (43 mm) and S2 (0.1 mm). The reason to have different length for the transmission lines was to push potential stray resonances, due to the reflection of the
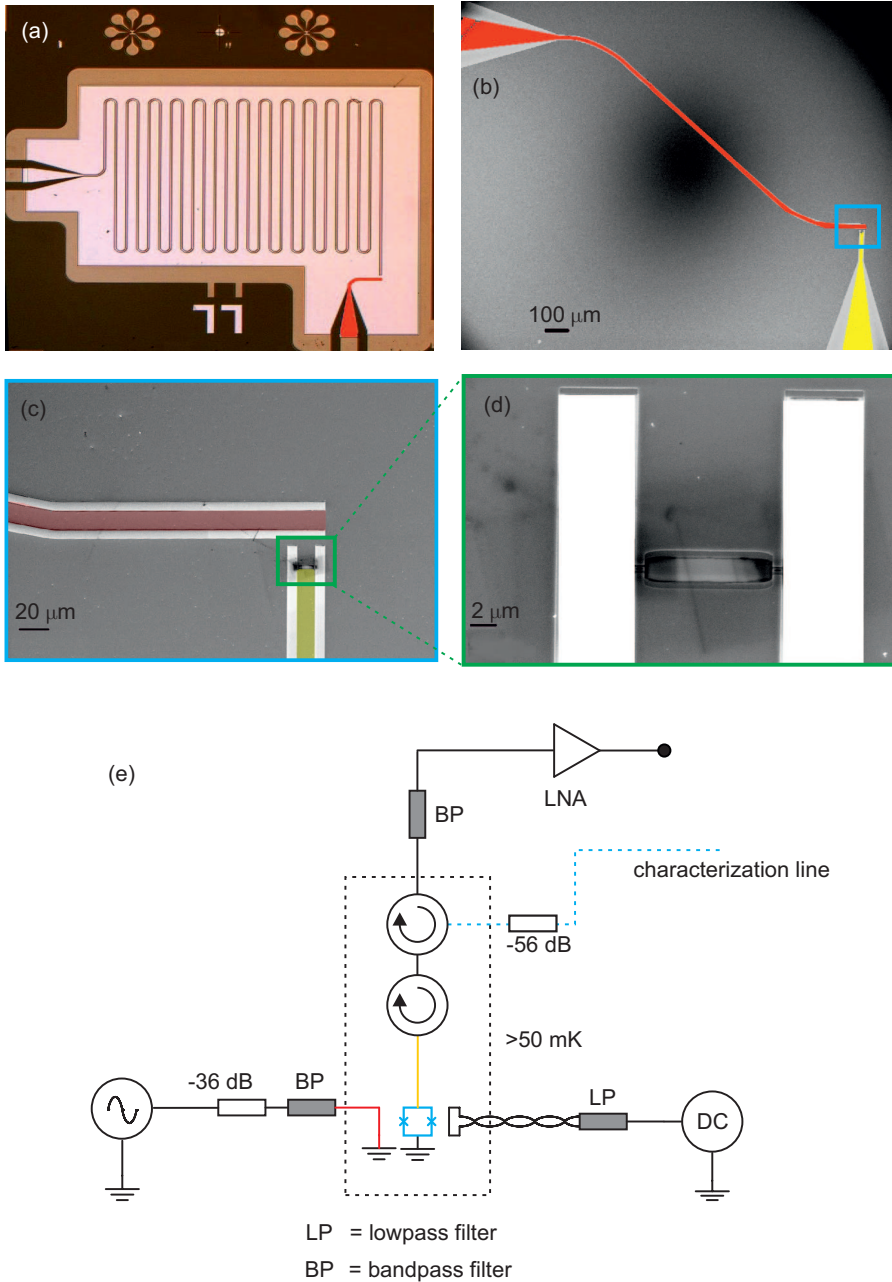
Figure 5.1: DCE samples and the measurement setup. (a) Sample S1 with 43 mm transmission line. The red line represents the drive line. (b) Sample S2 with 0.1 mm transmission line in yellow and again the drive line is in red. (c,d) Zoom-in SEM images for sample S1, showing the SQUID at the end of the transmission line. (e) Simplified measurement setup used in the DCE experiment.

field from the bonding wires (Figure 3.6), out of the measurement band of the experiment. The samples were cooled down in a dilution cryostat (known as ''Juliana'' and described in Chapter 3) with the base temperature of about 30 mK [Figure 3.4(b)].

A simplified measurement setup is shown in Figure 5.1(e). The SQUID (in blue) is connected to the transmission line (measurement line) at one end and is connected to the ground planes of the CPW at the other end. An external superconducting coil was attached to the sample holder, to provide the DC flux. An on-chip transmission line which here is called the drive line [red lines in Figure 5.1(a)-(d)], was short-circuited about 20 μm from the SQUID, and used to apply a sinusoidal oscillating flux signal to the SQUID loop. This drive signal, non-adiabatically changes the boundary condition imposed on the electromagnetic field in the transmission line. The output signal from the measurement line was passing two circulators before reaching the low-noise amplifier (LNA). After this first amplification, the signal was amplified further at room temperature and finally routed to the vector microwave digitizers.

Before starting the main experiment, we characterize the SQUID to find the proper DC flux bias point. We send a continuous microwave signal at a fixed frequency (in this case 5 GHz) through the characterization line [blue dashed line in Figure 5.1(e)] to the SQUID and measure the phase shift of the reflected signal, while sweeping the Φ_{ext} with the coil [blue dots in Figure 5.2 for S1]. It is clear that we can change the reflection from the SQUID by changing the SQUID inductance. The SQUID inductance changes as a function of the external magnetic flux passing through the SQUID loop (see Eq. 2.24). For the fitting [red solid line in Figure 5.2] we have approximated the SQUID with a resistor, capacitor and a tunable inductor in parallel. We choose the flux bias point of $\Phi_{ext} = -0.35\,\Phi_0$ for the rest of the experiment.

We now continue to the main measurement by applying a sinusoidal drive signal with a frequency of f_d to the drive line and measure the output power coming from the measurement line. The result of this measurement is presented in in Figure 2 of the Supplementary information, paper III. Here, we have swept the drive frequency and the drive power while *listening* at half of the drive frequency, $f_d/2$, where we expect to get the maximum DCE radiation (see Section 2.8). To do so, in practice we set the vector microwave digitizers to track the drive frequency at $f_d/2$. We observe the photon generation in both samples and for all the drive frequencies and powers. Next we investigate the signatures of the DCE radiation which were discussed earlier in Chapter 2.

Figure 5.3(a) and (b) show that we have broad band radiation for the full measurement band from 4 GHz to 6 GHz. Here, for sample S1 we set f_d= 10.3 GHz and measure the output flux density, n_{out}, as a function of the drive power and the digitizer detuning from the half of the drive frequency (5.15 GHz). Figure 5.3 (a) shows the positive and Figure 5.3 (b) shows the negative detuning from half of the drive frequency. The positive and the negative detunings were measured simultaneously using two digitizers in bands of 400 MHz. It is clear that the broadband spectrum is symmetric around $f_d/2$, although there are some stray resonances on both sides.

The red circles in Figure 5.3(d) show a line cut from (a) at a detuning of -764
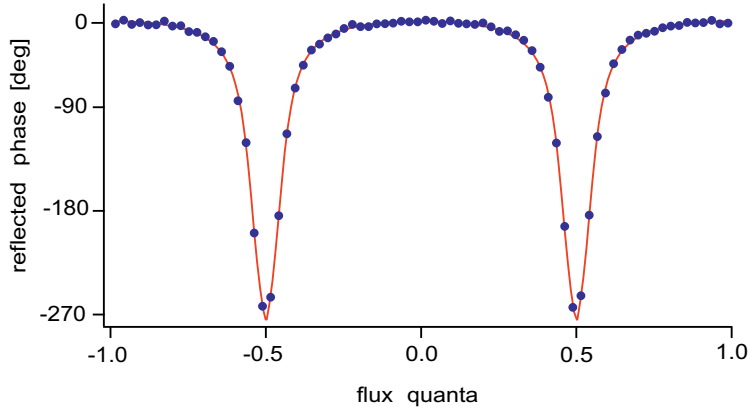
Figure 5.2: Modulation of the reflected phase from the measurement line. The measurement was performed for sample S1 and at probe frequency of 5 GHz. The flux bias point of $\Phi_{ext} = -0.35\,\Phi_0$ was chosen for the main measurement. The red line is a fir to the data considering the SQUID as a combination of a resistor, capacitor and a tunable inductor.

MHz (white dashed line). The blue line represents a fit to the theory described by Johansson *et al.* [125, 126]. We should note that the analytical formula for $n^{out}(\omega)$ [Eq. 2.37], is only valid for small drive amplitudes. Here, we are modulating the flux with amplitude of up to 0.15 Φ_0. In this case the $n^{out}(\omega)$ should be calculated numerically.

Another important signature of DCE too look for is the parabolic spectrum of the generated photons (Figure 2.7). In this setup our measurement band is not broad enough to cover the whole parabola. The drive line has a band pass filter, which limits f_d to 8-12 GHz. Proper filtering of the drive line is crucial since it prevents the leakage of thermal photons in the drive line which can couple to the measurement line. On the other hand, on the measurement line, circulators, LNA and the digitizers each have limited bandwidth which in total limits the measurement bandwidth from 4-6 GHz corresponding to drive frequencies of 8-12 GHz. Figure 5.3(c) shows the predicted DCE photon flux, calculated from Eq. 2.37 with the relevant parameters of our SQUID, for the drive frequency of 10 GHz. The grey zone shows our measurement band, which clearly indicates we need a larger measurement band to detect the parabolic shape of the spectrum.

The next step is to check if the photons are generated in pairs or not. We already discussed in Chapter 2 that this property of the DCE photons manifests itself as two-mode squeezing (TMS). Theory predicts a special structure for the correlations of the voltage field quadratures, due to the pair-wise photon creation of the DCE. In particular it predicts that, $\langle I_+ I_- \rangle = -\langle Q_+ Q_- \rangle$. We have measured the cross-correlations of the quadratures and observed such a relation for the cross-correlations [Figure 3(a) in paper III].
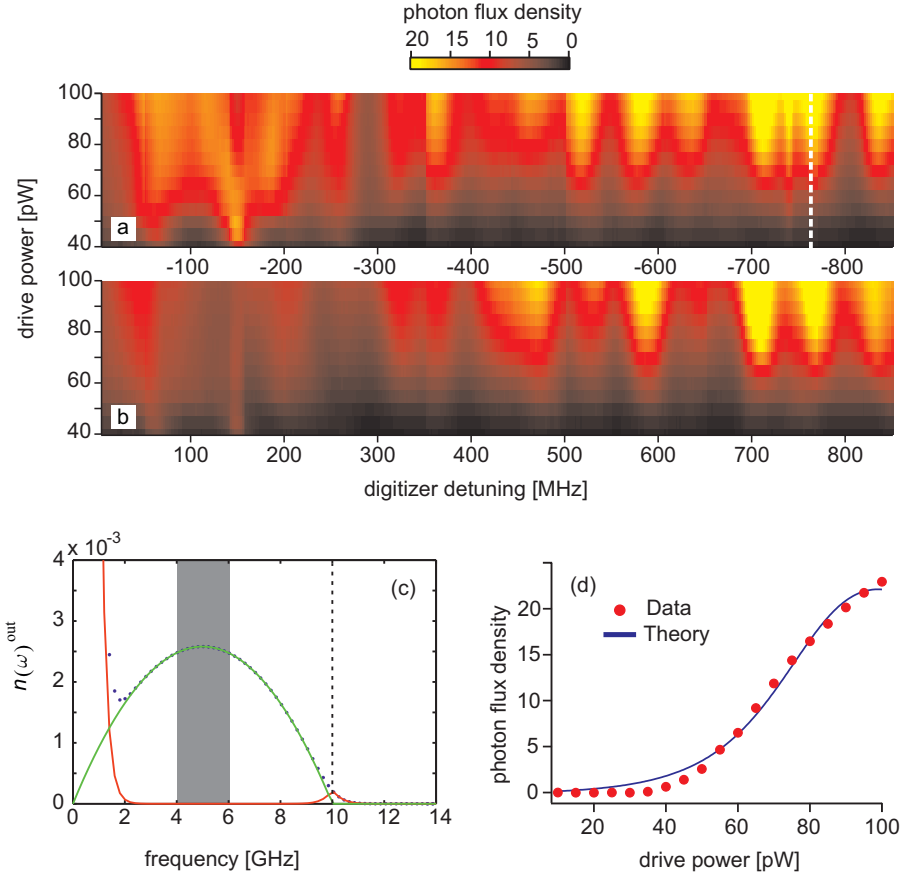
Figure 5.3: DCE photons generation. (a,b) Output flux density normalized to the the photon energy, $\hbar\omega$, for sample S1 and for $f_d = 10.3$ GHz, as a function of the drive power and detuning for negative(a) and for positive detuning(b). (c) Calculated photon flux density from Eq. 2.35, with the parameters of our SQUID and for $f_d = 10$ GHz (dashed line). We have assumed temperature of 10 mK and $\delta L_{eff} = 0.1 L_{eff}$ (see Eq. 2.39). The grey rectangle shows the measurement band. (d) A line cut from (a) at detuning of -764 MHz together with the theory fit (solid blue line) (see text).

Furthermore, theory predicts that the TMS should increase as a function of drive power. Figure 3(b) in paper III, shows the measured TMS for S1 with $f_d = 10.3$ GHz and detuning of ± 833 MHz. It is clear that the TMS increase with drive power while single modes remain unsqueezed, as predicted by the theory (see Chapter 2).

To summarize, we have observed broadband generation of photons over a frequency range of 1.7 GHz. The radiation is symmetric with respect to half the drive frequency and the photon flux rate agrees well with the theory. Furthermore, we observe two-mode squeezing of the radiation which is characteristic for pair production of photons. All these features are indeed expected from DCE radiation.

5.2 Probing the vacuum fluctuations with an artificial atom in front of a mirror

It is not possible to exchange information with a completely isolated artificial (or natural) atom. In order to interact with atoms, they should have a finite coupling to the environment. This coupling at the same time, cause the excited atom to decohere *i.e.* loose phase coherence after some time.

We already discussed the decoherence processes in our artificial atoms in Chapter 2. We discussed that the decoherence rate, γ, is due to two different processes, pure dephasing and relaxation. The decoherence rate is defined as $\gamma = \Gamma_1/2 + \Gamma_\phi$, where Γ_1 is the relaxation rate from the excited state (or equivalently $1/\Gamma_1$ is the excited-state lifetime) and Γ_ϕ is the pure dephasing rate.

These processes have different origins. The pure dephasing rate, Γ_ϕ, is related to the noise at low frequencies. The excited-state lifetime, $1/\Gamma_1$, on the other hand, is related to the fluctuations of the electromagnetic (EM) field at the transition frequency. If the system is cooled down to a temperature $T \ll \hbar\omega_a/k_B$, where ω_a is the atomic transition frequency, then the classical forms of these fluctuations, *i.e.* the thermal fluctuations, will be suppressed substantially. In this situation, the lifetime of the excite state is limited by the vacuum fluctuations.

In paper IV, we probe the vacuum fluctuations by measuring the lifetime of an artificial atom, a transmon qubit, embedded at the distance L from the end of a shorted transmission line. Figure 5.4(a) shows a micrograph of a sample. The sample is made on a silicon substrate with an intrinsic silicon oxide layer. The brown parts are the gold pads and the inner white parts are aluminium. The aluminium transmission line is colored with cyan and the dashed rectangle shows the transmon qubit. The transmission line is connected to the ground planes at this end point which forms a reflecting boundary condition for the EM filed, similar to the DCE experiment described in the previous Section.

We probe this system by sending a coherent field, V_{in}, with the probe frequency of $\omega_p/2\pi$ through the transmission line and measure the reflection coefficient, $r_p = \langle V_r \rangle / \langle V_{in} \rangle$, where $\langle ... \rangle$ denotes the time average [Figure 5.4(c) shows the microwave reflectometry setup]. In this case, due to the interference between the incoming and the reflected signal, a standing wave forms inside the transmission line. The grounded end of the transmission line, imposes a node for the electrical field.
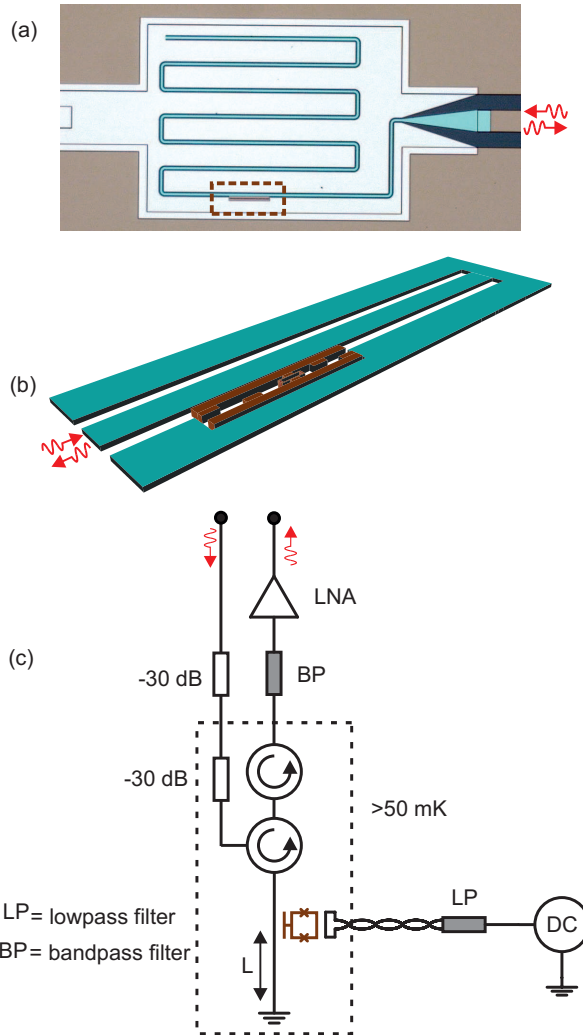
Figure 5.4: Sample description and measurement setup. (a) A false-colored micrograph of the sample. The transmission line in cyan is connected to the ground at the end. The dashed line rectangular shows the transmon position. (b) Schematic image of the sample, where the transmon qubit (brown) is coupled to the transmission line (cyan). (c) The measurement setup: microwave reflectometry is used to send a coherent probe signal to the sample and measure the phase and amplitude of the reflected signal. A superconducting coil attached to the sample box is used to apply the external flux to the SQUID loop of the transmon.

The atomic transition frequency of the transmon, $\omega_a/2\pi$, is a function of its charging energy, E_C, and its tunable Josephson energy, $E_J(\Phi_{ext})$ (Eq. 2.25). This allows us to change the transition wavelength of the atom, λ, by tuning ω_a,

$$\lambda(\Phi_{ext}) = \frac{2\pi c}{\sqrt{\epsilon}\,\omega_a(\Phi_{ext})} \simeq \frac{hc}{\sqrt{\epsilon}\,(\sqrt{8E_C E_J(\Phi_{ext})} - E_C)}, \qquad (5.1)$$

where c is the light velocity in vacuum, ϵ is the dielectric constant of the transmission line and h is Plank's constant. Although the physical distance between the atom and the mirror, L, is constant by tuning λ we can change the normalized distance, L/λ, and consequently change the strength of the EM field at the position of the atom.

Figure 5.5(a) shows the magnitude of the measured reflection coefficient, $|r_p|$, as a function of the probe frequency and the external flux for a weak probe. We note that the weak probe power regime is such that the Rabi frequency, Ω_p, is much smaller than the decoherence rate. The Rabi frequency is the frequency of exchanging energy between the field and the qubit and it depends on the probe power, P_p, and the relaxation rate,

$$\Omega_p = \sqrt{\frac{2\Gamma_1 P_p}{\hbar\omega_a}} = k\sqrt{P_p}, \qquad (5.2)$$

where $k = \sqrt{2\Gamma_1/\hbar\omega_a}$ is the atom-field coupling constant. We observe that $\omega_a/2\pi$ can be tuned from 4.8 GHz to 5.9 GHz by changing Φ_{ext}. It is interesting to note that the response vanishes completely around 5.4 GHz. At this frequencies L/λ value has changed in such way that the qubit is in the node of the electrical field. This effectively hides (decouples) the qubit from the probe field.

Figure 5.5(b) shows two line cuts from (a) around $\sim$4.8 GHz and $\sim$ 5.5 GHz (shown with red and black arrows in (a) respectively). The general formula for the reflection coefficient is derived in Refs [106, 153]. For weak probe power it is simplified to

$$r_p = -1 + \frac{\Gamma_1}{\gamma + i\delta\omega_p}, \qquad (5.3)$$

where $\delta\omega_p$ is the detuning of the probe frequency from ω_a. The solid lines in Figure 5.5(b) are fits to the data using Eq. 5.3 which allows us to directly extract Γ_1 and λ. The extracted values of $\Gamma_1/2\pi$ (11.8 MHz and 1.2 MHz) differ by a factor of 9.8 between two points, indicating that the vacuum fluctuation strength is different between the two flux points.

We extract the Γ_1 and Γ_ϕ in a similar way for all the flux points in Figure 5.5(a). Figure 2(c) in paper IV shows these extracted values as a function of the normalized distance, L/λ. The shaded area is the frequencies when the atom is completely hidden from the probe filed and consequently $|r_p| \simeq 1$. Koshino *et al.* [153] showed that $\Gamma_1(\Phi_{ext})$ should follow

$$\Gamma_1(\Phi_{ext}) = 2\Gamma_{1,b}\cos(\theta(\Phi_{ext}))^2, \qquad (5.4)$$
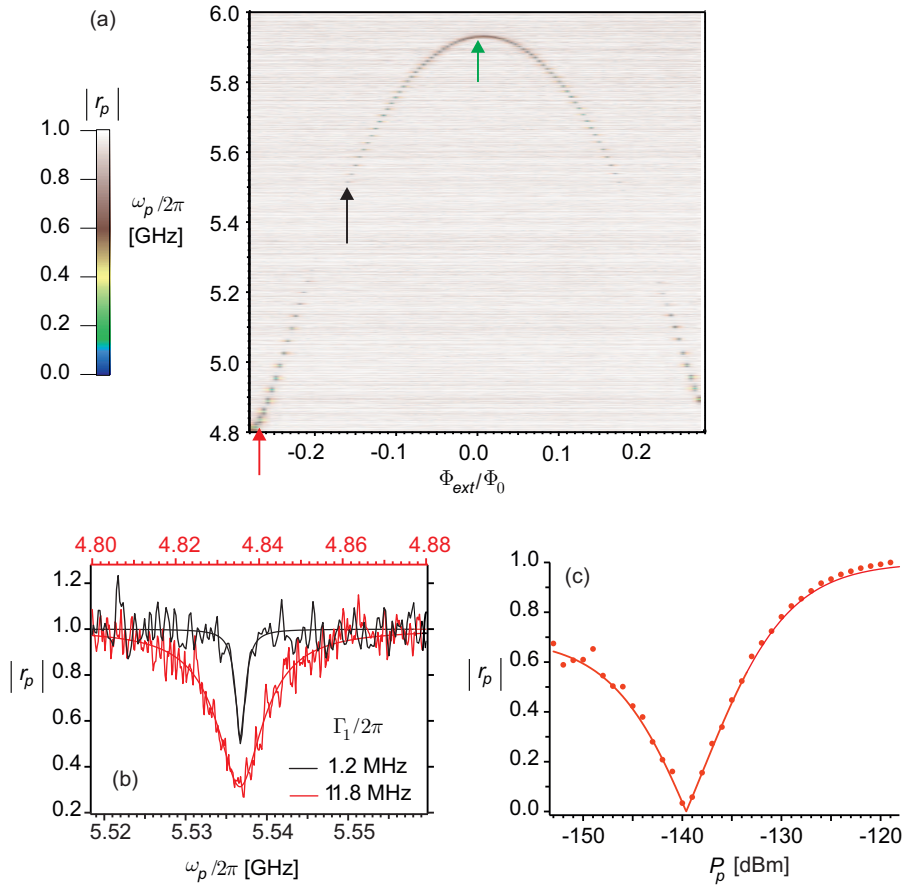
Figure 5.5: Atom in front of a mirror measurements. (a) Magnitude of the reflection coefficient, $|r_p|$, as function of the ω_p and Φ_{ext}. We can tune the transition frequency of the atom by changing $\Phi_e xt$. Around $\Omega_p/2\pi = 5.4$ GHz the response vanishes ($|r_p| \simeq 1$) which indicates that the atom is the node of the field. (b) Two line cuts from (a) for the two different values of Φ_{ext} which are indicated by the red and the black arrows in (a). We have used Eq. 5.3 to fit the data (solid curves) and extract the Γ_1 and Γ_ϕ for each bias point. (c) $|r_p|$ as a function of the resonant field power. The solid line is a fit to Eq. 5.5 which gives k, the atom-field coupling constant (see text).

where $\Gamma_{1,b}$ is the inverse of the bare atomic lifetime and $\theta(\Phi_{ext})$ is the phase factor of the probe field for travelling a round trip from the beginning to the end of the transmission line (Eq. 2 in paper IV). The solid line in Figure 2(c) in paper IV represents the predicted values using Eq. 5.4.

We mentioned in Chapter 2 that the mathematical tool to quantify the random precesses and their fluctuations is the power spectral density. Indeed, the power spectral density is the Fourier transform of the auto-correlation function (Eq. 2.3). Similarly, the strength of the fluctuations of the EM field near the atomic transition frequency, ω_a, are related to the spectral density of the vacuum fluctuations, $S(\omega_a)$.

The effect of these fluctuations on the excited atom lifetime depends on how strongly the atom and the field are coupled to each other. They are simply related to each other through the atom-field coupling constant, $\Gamma_1 = k^2 S(\omega_a)$ [96]. We already extracted Γ_1 for the different values of the normalized distance, so if we can estimate k for our system, we can obtain $S(\omega_a)$.

We can find k in two different ways. Firstly, from the nonlinear power dependence of $|r_p|$ and secondly, from the microwave simulations for our specific geometry.

For the first method, we have measured $|r_p|$ as a function of the probe power for the flux bias of $\Phi_{ext} = 0$ [the green arrow in Figure 5.5(a)]. Circles in Figure 5.5(c) shows $|r_p|$ for this flux bias point and for $\delta\omega_p = 0$. Theory predicts that for $\delta\omega_p = 0$ *i.e.* a resonant probe field,

$$r_p = -1 + \frac{\Gamma_1^2}{\Gamma_1\gamma + \Omega_p^2}. \tag{5.5}$$

The solid line in Figure 5.5(c) is the fit to Eq. 5.5 using the extracted values of Γ_1 and Γ_ϕ for this flux point. Then the only free parameter in the fitting process is Ω_p which directly relates to k using Eq. 5.2. Estimating the overall attenuation in the drive line, we evaluated k from this method to be $k_e \simeq 6.1 \times 10^{15}$ Hz/$\sqrt{W}$. The subscript "e" denotes that it is obtained from the fitting to the experimental data.

For the second method, we have used the fact that the atom-field coupling depends on the designed geometry of the sample. Peropadre *et al.* have shown that $k = e\beta\sqrt{Z_0}(E_J/2E_C)^{1/4}/\hbar$, where $Z_0 = 50\Omega$ and β is the ratio of the coupling capacitance, C_c, to the total capacitance of the transmon, C_Σ, $\beta = C_c/C_\Sigma$ [101]. We have estimated $\beta \simeq 0.4$ using a simulation software package, Microwave Office for the geometry of our sample. This, together with the extracted values of E_C and E_J from fitting Eq. 5.1 to Figure 5.5(a) results in $k_s \simeq 8.8 \times 10^{15}$ Hz/$\sqrt{W}$ where subscript "s" denotes that it is obtained from the simulation.

These methods give slightly different values for k. The uncertainties originate form the exact evaluation of the P_p that reaches the sample and also the exact value of the dielectric constant used in the simulations. We have used the mean of the k values obtained from the two methods, $k_m = 7.45 \times 10^{15}$ Hz/$\sqrt{W}$, to evaluate the spectral density of the vacuum fluctuations.

Figure 4 in paper IV shows the extracted values of the spectral density of the vacuum fluctuations, $S(\omega_a)$, as a function of the normalized distance. The spectral

density is plotted in the unit of the number of energy quanta at frequency ω_a by normalizing it to $\hbar\omega_a$. Further, theory predicts that [154]

$$S(\omega_a) = 2\hbar\omega_a \cos^2[\theta(\Phi_{ext})/2] \tag{5.6}$$

which is shown by the solid black line in Figure 4 in paper IV. This predicts that for the atom in front of the mirror, the vacuum fluctuations strength varies from 0 (node) to $2\hbar\omega_a$ (antinode), in contrast with for the atom in an open transmission line (without the mirror) where $S = 1\hbar\omega_a$ quanta. The fact that the theory prediction falls inside the data error bars indicates a good agreement between the data and the theory. The lowest value of the vacuum fluctuations we are able to measure in this system is 0.02 quanta which is shown with an arrow in Figure 4(a) of paper IV.

To summarize, we have measured the strength of the vacuum fluctuations using a transmon qubit in front of a mirror as our quantum probe. We have demonstrated that by changing the normalized distance between the atom and the mirror we can change the modulation of the vacuum fluctuations by a factor of 9.8. This experiments suggests a simple scheme in circuit QED to probe the vacuum fluctuations.

5.3 Scattering properties of two atoms in front of a mirror

In Chapter 2, we discussed the scattering properties of a transmon qubit embedded at the end of a single-ended transmission line. Such a system is interesting from several aspects and despite the simple geometry is a promising platform to study quantum optics. For example, we already showed in previous section that a transmon qubit at a distance from the end of a transmission line, acts as a quantum probe for vacuum fluctuations.

Another interesting aspect to study is the interaction of two or more qubits in these systems. Thanks to the well-established fabrication and measurement techniques in circuit QED, the number of qubits in these systems is readily scalable. It is possible to design and fabricate such circuits with more qubits, which is a crucial step in realization of future quantum circuits.

Apart from the potential for future applications, these systems with several qubits allows us to explore the photon-mediated interactions between different artificial atoms. Recently, van Loo *et al.* have measured a system consisting of two distant transmon qubits coupled to an open transmission line and observed strong interaction effects between the two qubits [155].

In Paper V, we study these collective atom-photon interactions for two transmons embedded at the end of an *open* transmission line (Figure 5.6). Here we present the *preliminary* results for the scattering properties of such a system. We note that although the preliminary studies show a good agreement between the theory and the experiment, the full interpretation of the results requires more in depth analysis.

The aluminium transmons and CPW were fabricated on a silicon substrate with an intrinsic oxide layer. Two on-chip flux lines were designed to apply a local mag-
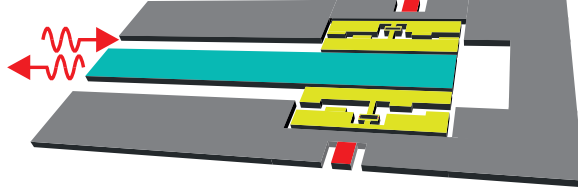
Figure 5.6: Schematic image of two atoms in front of a mirror. Two transmons (in yellow) are embedded at the open end of a transmission line (cyan). Two on-chip flux lines (red) were used to apply a local magnetic flux to each transom and control the transition frequency.

netic flux through the SQUID loop of each transmon (indicated with red in Figure 5.6). This enables us to tune the transition frequency of each transmon, ω_a, separately. A superconducting coil attached to the sample box was used to apply a global magnetic field.

The sample was cooled down to a temperature below 50 mK in a dilution refrigerator ["Juliana" in Figure 3.4(b)]. The microwave reflectometry setup was similar to the measurement setup in Figure 5.4(c). We characterized the system by sending a coherent probe field through the transmission line and measuring the reflected signal with a vector network analyzer (VNA).

Figure 2 in Paper V shows the magnitude of the reflection coefficient, r, as a function of the external flux, Φ_{ext}, applied through the coil. It shows that we can tune ω_a of transmons by changing the global flux applied through the coil. The dashed lines are the fits to Eq. 2.34 which enables us to extract the charging energy, E_C, and the maximum Josephson energy, $E_{J_{max}}$, of each transmon (Table I in Paper V).

We note that the qubits are designed to be nominally identical which results in similar values of E_C, since the charging energy is determined by the geometry of the sample. On the other hand, the maximum Josephson energy is proportional to the critical currents of the SQUID's tunnel junctions and varies with the junction resistance. The resistance of the junctions are determined by their size and their oxide thickness. A small variation in any of these values during the fabrication leads to different resistance and consequently different values of $E_{J_{max}}$ even for transmons with identical design (Table I in Paper V).

We continue by measuring the power dependence of the reflected signal. We choose a global flux point where the two qubits transition frequency are separated

by ~ 290 MHz and measure r for different probe powers, P_p. Figure 3(a) in Paper V shows the magnitude of r as a function of the probe frequency, $\omega_p/2\pi$, and probe power. Similar to the previous experiments the incident power which reaches the qubits is calculated by estimating the overall attenuation in the measurement line (in this case around -125 dB). In Section 2.6.6, we discussed the power dependence of r for a resonant incident field ($\omega_p = \omega_a$). To compare with theory, we plotted the resonant line cuts of this plot in Figure 3(b) in Paper V. We observe that the response of each transmon to the resonant probe is in agreement with the theory prediction (Figure 2.6) and the previous reports on similar systems with one qubit [156].

Sofar, we have treated the two transmons as individual qubits and have not considered the interaction between them. The qubits interact either by the direct coupling, with strength g, or by exchanging photons through the transmission line (photon-mediated coupling). Since we were interested to study the photon-mediated interactions we have designed the sample to have a small direct coupling by placing the transmons on the opposite sides of the transmission line (there is about 80 μm between the center of two SQUIDs). In this way, the qubits interact mainly through the transmission line, and when their transition frequencies are largely detuned (in comparison with the coupling rate of each transmon) they can ba considered as uncoupled transmons.

We continue the measurements by fixing the global flux at a point close to the previous measurement and apply a current through the on-chip flux lines to change the detuning between the transition frequencies of the two transmons, $\delta\omega = \omega_{a,1} - \omega_{a,2}$. Figure 5.7(a) shows the magnitude of r as a function of the probe frequency and the absolute value of the external flux applied by the on-chip lines. We note that in this case, we applied an equal current but in different directions to the on-chip flux lines to change the transition frequencies symmetrically. The reason that the data in Figure 5.7(a) is skewed is due to a finite cross talk between the two on-chip flux lines. In another measurement which is presented in Figure 4.(a) Paper V, we have compensated for this cross talk by sending a current with opposite direction to the other on-chip flux line.

In Figure 5.7(b) we have plotted to line cuts from Figure 5.7(a) corresponding to maximum detuning ($\delta\omega \simeq 240$ MHz for Φ_{ext}=0, blue) and zero detuning ($\delta\omega \simeq 0$ for Φ_{ext}=-0.185, red) *i.e.* when the two qubits have the same resonance frequency and are coupled through the transmission line. It is interesting to observe that the coupled qubits form a collective state with different properties from each individual qubit.

We also tried another approach in tuning $\delta\omega$. Figure 5.7(c) shows a measurement where we only applied a current through one of the on-chip flux lines (qubit 1). In practice, as mentioned before we applied a small current to the other flux line (qubit 2) in opposite direction as well to compensate for the crosstalk. We see that we can change $\delta\omega$ by changing $\omega_{a,1}$ while keeping $\omega_{a,2}$ almost constant. Again, we plot the line cuts for $\delta\omega = 0$ and $\delta\omega = \delta\omega_{max} \simeq 200$ MHz and observe that at zero detuning the qubits show interesting collective effects (Figure 5.7(d)).

To characterize the collective state more, we have measured r as a function of P_p, for the flux point corresponding to $\delta\omega = 0$ in Figure 4(a) in Paper V. The result of this measurement is shown in Figure 4(c) in Paper V. In order to compare this with
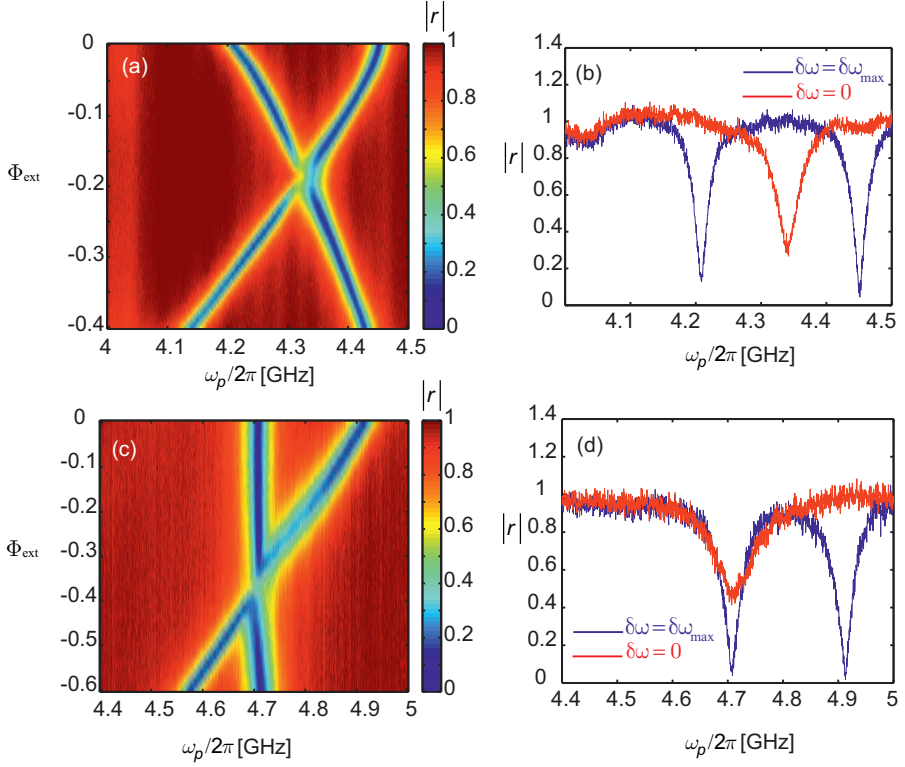
Figure 5.7: Changing the detuning between the transition frequencies of two atoms in front of a mirror. (a) By applying the same current but in different directions to the on-chip flux lines we can symmetrically change the detuning between the transition frequencies of two atoms, $\delta\omega = \omega_{a,1} - \omega_{a,2}$. The external flux applied by the on-chip flux line is in arbitrary unit since we can not pass the sufficient current through the on-chip flux line to sweep one full period and calibrate the flux. (b) Two line cuts from (a) for $\delta\omega = \delta\omega_{max}$ in blue and corresponding to Φ_{ext}=0 and for $\delta\omega = 0$ in red and for Φ_{ext}=-0.185. It shows that two qubits can couple through the transmission line. (c) Changing $\delta\omega$ by changing the transition frequency of qubit 1 while keeping the transition frequency of qubit 2 constant. (d) Two line cuts from (c) for the maximum detuning (Φ_{ext}=0) and zero detuning (Φ_{ext}=-0.36) show the collective state of the two transmons.

the qubits response at large detunings, in Figure 4(d) in Paper V, we have plotted the resonant line cuts for the zero detuning and for the large detunings together. We see that the behaviour of the collective state is different from the single qubits.

As mentioned before, these systems despite the simple geometry contain very rich physics. The full interpretation of the collective state and the photon-mediated coupling between the atoms requires more in depth theory efforts. In Paper V, have shown the preliminary interpretation of the data thanks to the efforts by Sankar Raman Sathyamoorthy and Göran Johansson who developed the theory for this system.

We have presented the preliminary results for characterization of a system consists of two atoms in front of a mirror. We have shown that we have a full control over the system to change the detuning between the transition frequencies of two atoms. We have observed that for large detunings the atoms shows the same behaviour similar to a single atom in front of a mirror but for zero detuning they form a collective state which shows different behaviour from each atom. This system is promising platform to study quantum optics for multiple atoms.

Appendix I

Recipes for sample fabrication

Fabrication of gold pads (large structures)

- Spin-coat HDMS at 3000 RPM for 1 min. Bake for 1 min. at 110°C.

- Spin-coat LOR 3B at 3000 RPM for 1 min. Bake for 5 min. at 200°C.

- Spin-coat S1813 at 3000 RPM for 1 min. Bake for 2 min. at 110°C.

- Expose for 8.5 sec. in "low-vacuum" mode and with gap of 20 μm in MA6 mask aligner.

- Develop the photo resist in MF319 for 30 sec., rinse it in QDR bath and blowdry with N_2.

- Ash for 10 sec. (optional).

- Deposit trilayer of Ti(3-5 nm)-Au(85 nm)-Pd(10 nm) in an evaporator.

- Liftoff can be performed in 1165-remover at 75 °C for about 45 min.

E-beam lithography (two layer resist)

- Spin-coat MMa(8.5)PMMA EL10 in two steps: first at 500 RPM for 5 sec. and then at 2000 RPM for 45 sec.

- Bake for 5 min. at 170°C.

- Spin-coat ZEP 520A 1:2 Anisole at 1500 RPM for 45 sec.

- Bake for 5 min. at 150°C.

- Expose with JEOL at 100 kV.

- Develop the top layer in O-xylene for about 1-2 min (usually performed for the whole wafer). Develop the top layer in O-xylene for about 1-2 min.

- Develop the bottom layer in H_2O/IPA (1:4) for about 10 min (separately performed for different chips to tune the undercut profile)

- Rinse it in IPA and blowdry with N_2.

- Ash for 10 sec. (optional).

E-beam lithography (trilayer resist)

- Spin-coat MMA(8.5)PMMA EL10 at 6000 RPM for 1 min. (resist thickness of about 320 nm).

- Bake for 15 min. at 170°C.

- Evaporate 15-30 nm of germanium in a *thermal* evaporator.

- Spin-coat ZEP 520A 1:2 Anisole at 2000 RPM for 1 min. (resist thickness of about 100 nm)

- Bake for 5 min. at 170°C.

- Expose with JEOL at 100 kV (for SETs with doses about $\sim$350 μC/cm^2).

- Develop the top layer in Hexyl acetate for for 1 min.

- Etch with a low-pressure CF$_4$ plasma for about 30 sec. in 404 Oxford Plasmalab.

- For the undercut profile, ash for about 20 min. in Batchtop.

- After this, the chip is ready for shadow evaporation in Plassys aluminum evaporator.

Charge dissipation layer for insulating substrates

- Spin-coat Espacer 300 Z at 2000 RPM for 1 min.

- Bake for 1 min. at 90°C.

- Directly after the e-beam develop (dissolve) in water for 30 sec.

Shadow evaporation of aluminium

The majority of the samples in this thesis were made in Plassys aluminum evaporator. The evaporation angle and the oxidation time vary with the resist thickness and the intended resistance of the junctions. We normally used 30 nm and 50 nm of aluminium in each evaporation step and oxidize around 40 min in pressure of 0.2 mbar.

For the liftoff of excess aluminum after the evaporation, we used 1165 remover at 70°C and rinsed afterwards in IPA and Methanol.

Acknowledgements

First and foremost, I would like to express my gratitude to my supervisor professor Per Delsing for giving me the opportunity to work in his group. Thank you for all the guidance, encouragements, and your significant contribution in all the research presented in this thesis. Secondly, I would like to thank Martin Gustafsson for being such a nice friend and supervisor. I learned a lot from you and enjoyed spending hours and hours with you looking for logarithmic charge drifts.

Special thanks goes to John Clarke for sharing his knowledge. Thanks for your significant contribution in my research. From all of your red inks in my manuscripts, I learned to pay more attention to details.

I would like to thank Chris Wilson and Jonas Bylander for supervising me in the lab. Thank you both for your advices and your patience with my stupid questions. I also thank Thilo Bauch for helping me with the measurements in Mr. Freeze.

Special acknowledgment goes to people at the Applied Quantum Physics Laboratory: Sankar Raman Sathyamoorthy, Anton Frisk Kockum, Joel Lindkvist, Lars Tornberg, and specially Göran Johansson. Göran is not only a great physicist but also a very good teacher. I really appreciate all the time you spent showing me how to interpret my results. Special acknowledgments goes to Sankar for his theory support and his contribution to my research.

Special thanks to Philip Krantz and Michael Simoen with whom I shared my office for all these years. Thank you guys for being my best friends. I really enjoyed all the moments we spent together inside and outside the lab.

I would like to thank former members of our group Simon Abay and IoChun Hoi for their support. Thank you IoChun for helping me with the qubit projects.

I am grateful to Jan Jacobsson for taking care of the helium liquefier and to Lars Jönsson and Staffan Pehrson for all the support in the workshop. Special thanks go to Susannah Carlsson, Maria Tremblay, Marie Fredriksson and Ann-Marie Frykestig for all the administrative supports during these years.

I also want to thank all the present and past members of the QDP lab. Thanks for making QDP such a nice place to work.

I would also like to thank the staff of the Nanofabrication laboratory, for all the support and help in the cleanroom, especially Henrik Frederiksen and Bengt Nilsson.

Finally, I would like to use this opportunity to thank my family and my friends for their support during all these years. Thank you Hengameh, for all these years and your endless support in my life and sorry for all the weekends and holidays you spent alone, while I was working. I am sure I couldn't make it without you

Bibliography

[1] R. A. Millikan. On the elementary electrical charge and the Avogadro constant. *Physical Review*, 2:109, 1913.

[2] C. J. Gorter. A possible explanation of the increase of the electrical resistance of thin metal films at low temperatures and small field strengths. *Physica*, 17:777, 1951.

[3] I. Giaever and H. R. Zeller. Superconductivity of small tin particles measured by tunneling. *Physical Review Letters*, 20:1504, 1968.

[4] H. R. Zeller and I. Giaever. Tunneling, zero-bias anomalies, and small superconductors. *Physical Review*, 181:789, 1969.

[5] C. A. Neugebauer and M. B. Webb. Electrical conduction mechanism in ultrathin, evaporated metal films. *Journal of Applied Physics*, 33:74, 1962.

[6] J. Lambe and R. C. Jaklevic. Charge-quantization studies using a tunnel capacitor. *Physical Review Letters*, 22:1371, 1969.

[7] T. A. Fulton and G. J. Dolan. Observation of single-electron charging effects in small tunnel junctions. *Physical Review Letters*, 59:109, 1987.

[8] M. H. Devoret, D. Esteve, and C. Urbina. Single-electron transfer in metallic nanostructures. *Nature*, 360:547, 1992.

[9] C. Wasshuber. Single-electronics - how it works. how it's used. how it's simulated. In *Quality Electronic Design, 2002. Proceedings. International Symposium on*, page 502, 2002.

[10] K.K. Likharev. Correlated discrete transfer of single electrons in ultrasmall tunnel junctions. *IBM Journal of Research and Development*, 32:144, 1988.

[11] J. J. Sakurai. *Modern Quantum Mechanics*. Addison Wesley, 1993.

[12] M. Razavy. *Quantum Theory of Tunneling*. World Scientific Pub Co Inc, 2003.

[13] S. Kogan. *Electronic Noise and Fluctuations in Solids*. Cambridge University Press, 1996.

[14] H. W. Ott. *Noise Reduction Techniques in Electronic Systems*. Wiley-Interscience, 1988.

[15] E. Paladino, Y. M. Galperin, G. Falci, and B. L. Altshuler. 1/f noise: Implications for solid-state quantum information. *Reviews of Modern Phyisics*, 86:361, 2014.

[16] K.K. Likharev. Single-electron transistors: Electrostatic analogs of the dc squids. *Magnetics, IEEE Transactions on*, 23:1142, 1987.

[17] B. S. DeWitt. Quantum field theory in curved spacetime. *Physics Reports*, 19:295, 1975.

[18] G. T. Moore. Quantum theory of the electromagnetic field in a variable-length one-dimensional cavity. *Journal of Mathematical Physics*, 11:2679, 1970.

[19] S. A. Fulling and P. C. W. Davies. Radiation from a moving mirror in two dimensional space-time: Conformal anomaly. *Proceedings of the Royal Society of London. A. Mathematical and Physical Sciences*, 348:393, 1976.

[20] V. V. Dodonov. Current status of the dynamical casimir effect. *Physica Scripta*, 82:038105, 2010.

[21] M. A. Nielsen and I. L. Chuang. *Quantum Computation and Quantum Information*. Cambridge University Press, 2000.

[22] G. Ithier, E. Collin, P. Joyez, P. J. Meeson, D. Vion, D. Esteve, F. Chiarello, A. Shnirman, Y. Makhlin, J. Schriefl, and G. Schön. Decoherence in a superconducting quantum bit circuit. *Physical Review B*, 72:134519, 2005.

[23] A. A. Houck, J. A. Schreier, B. R. Johnson, J. M. Chow, Jens Koch, J. M. Gambetta, D. I. Schuster, L. Frunzio, M. H. Devoret, S. M. Girvin, and R. J. Schoelkopf. Controlling the spontaneous emission of a superconducting transmon qubit. *Physical Review Letters*, 101:080502, 2008.

[24] A. Lambrecht. The Casimir effect: a force from nothing. *Physics World*, 2002.

[25] H. Pothier, P. Lafarge, C. Urbina, D. Esteve, and M. H. Devoret. Single-electron pump based on charging effects. *Europhysics Letters*, 17:249, 1992.

[26] J. R. Petta, A. C. Johnson, C. M. Marcus, M. P. Hanson, and A. C. Gossard. Manipulation of a single charge in a double quantum dot. *Physical Review Letters*, 93:186802, 2004.

[27] Yu. A. Pashkin, Y. Nakamura, and J. S. Tsai. Room-temperature Al single-electron transistor made by electron-beam lithography. *Applied Physics Letters*, 76:2256, 2000.

[28] A. Aassime, D. Gunnarsson, K. Bladh, P. Delsing, and R. J. Schoelkopf. Radio-frequency single-electron transistor: Toward the shot-noise limit. *Applied Physics Letters*, 79:4031, 2001.

[29] H. Brenning, S. Kafanov, T. Duty, S. Kubatkin, and P. Delsing. An ultrasensitive radio-frequency single-electron transistor working up to 4.2 k. *Journal of Applied Physics*, 100:114321, 2006.

[30] N. Wiener. Generalized harmonic analysis. *Acta Mathematica*, 55:117, 1930.

[31] J. Johnson. Thermal agitation of electricity in conductors. *Physical Review*, 32:97, 1928.

[32] H. Nyquist. Thermal agitation of electric charge in conductors. *Physical Review*, 32:110, 1928.

[33] Ya.M. Blanter and M. Büttiker. Shot noise in mesoscopic conductors. *Physics Reports*, 336:1, 2000.

[34] R. J. Schoelkopf, P. Wahlgren, A. A. Kozhevnikov, P. Delsing, and D. E. Prober. The radio-frequency single-electron transistor (rf-set): A fast and ultrasensitive electrometer. *Science*, 280:1238, 1998.

[35] A. N. Korotkov. Intrinsic noise of the single-electron transistor. *Physical Review B*, 49:10381, 1994.

[36] S. Kafanov and P. Delsing. Measurement of the shot noise in a single-electron transistor. *Physical Review B*, 80:155320, 2009.

[37] S. Abay. *PhD thesis: Charge transport in InAs nanowire devices*. Chalmers University of Technology, 2013.

[38] M. Furlan and S. Lotkhov. Electrometry on charge traps with a single-electron transistor. *Physical Review B*, 67:1, 2003.

[39] U. Hanke, Y. Galperin, and K. A. Chao. Charge sensitivity of a single electron transistor. *Applied Physics Letters*, 65:1847, 1994.

[40] A. N. Tavkhelidze and J. Mygind. Low-frequency noise in single electron tunneling transistor. *Journal of Applied Physics*, 83:310, 1998.

[41] T. Henning, B. Starmark, T. Claeson, and P. Delsing. Bias and temperature dependence of the noise in a single electron transistor. *The European Physical Journal B*, 8:627, 1999.

[42] V. A. Krupenin, D. E. Presnov, M. N. Savvateev, H. Scherer, a. B. Zorin, and J. Niemeyer. Noise in Al single electron transistors of stacked design. *Journal of Applied Physics*, 84:3212, 1998.

[43] H. A. Nilsson, T. Duty, S. Abay, C. M. Wilson, J. B. Wagner, C. Thelander, P. Delsing, and L. Samuelson. A radio frequency single-electron transistor based on an InAs/InP heterostructure nanowire. *Nano Letters*, 8:872, 2008.

[44] A. Balandin. Low-frequency 1/f noise in graphene devices. *Nature nanotechnology*, 8:549, 2013.

[45] S. Machlup. Noise in semiconductors: Spectrum of a two-parameter random signal. *Journal of Applied Physics*, 25:341, 1954.

[46] F.N. Hooge and P.A. Bobbert. On the correlation function of 1/f noise. *Physica B: Condensed Matter*, 239:223, 1997.

[47] K. Bladh, D. Gunnarsson, A. Aassime, M. Taslakov, R. Schoelkopf, and P. Delsing. Noise performance of the radio-frequency single-electron transistor. *Physica E: Low-dimensional Systems and Nanostructures*, 18:91, 2003.

[48] A. B. Zorin, F.-J. Ahlers, J. Niemeyer, T. Weimann, H. Wolf, V. A. Krupenin, and S. V. Lotkhov. Background charge noise in metallic single-electron tunneling devices. *Physical Review B*, 53:13682, 1996.

[49] D. Song, A. Amar, C.J. Lobb, and F.C. Wellstood. Advantages of superconducting coulomb-blockade electrometers. *IEEE Trans. Appl. Supercond.*, 5:3085, 1995.

[50] N. Zimmerman, J. Cobb, and A. Clark. Modulation of the charge of a single-electron transistor by distant defects. *Physical Review B*, 56:7675, 1997.

[51] T. F. Li, Yu. A. Pashkin, O. Astafiev, Y. Nakamura, J. S. Tsai, and H. Im. Low-frequency charge noise in suspended aluminum single-electron transistors. *Applied Physics Letters*, 91:033107, 2007.

[52] P. J. Hakonen, J. M. Ikonen, Ü. Parts, J. S. Penttilä, L. R. Roschier, and M. a. Paalanen. Noise of a single electron transistor on a Si_3N_4 membrane. *Journal of Applied Physics*, 86:2684, 1999.

[53] S. Kafanov, H. Brenning, T. Duty, and P. Delsing. Charge noise in single-electron transistors and charge qubits may be caused by metallic grains. *Physical Review B*, 78:125411, 2008.

[54] K. R. Brown, L. Sun, and B. E. Kane. Electric-field-dependent spectroscopy of charge motion using a single-electron transistor. *Applied Physics Letters*, 88:213118, 2006.

[55] P. Dutta and P. M. Horn. Low-frequency fluctuations in solids: 1/f noise. *Reviews of Modern Physics*, 53:497, 1981.

[56] M. Kenyon, C. J. Lobb, and F. C. Wellstood. Temperature dependence of low-frequency noise in Al-Al_2O_3-Al single-electron transistors. *Journal of Applied Physics*, 88:6536, 2000.

[57] O. Astafiev, Yu. A. Pashkin, Y. Nakamura, T. Yamamoto, and J. S. Tsai. Temperature square dependence of the low frequency 1/f charge noise in the josephson junction qubits. *Physical Review Letters*, 96:137001, 2006.

[58] William R. Smythe. *Static and dynamic electricity*. McGraw-Hill, 1939.

[59] E. Mathieson. *Induced charge distributions in proportional detectors*. Brookhaven National Laboratory, 1939.

[60] R. P. Feynman. *Quantum Electrodynamics*. Westview Press, 1998.

[61] R. P. Feynman. *QED: The Strange Theory of Light and Matter*. Princeton University Press, 2006.

[62] S. Haroche and D. Kleppner. Cavity Quantum Electrodynamics. *Physics Today*, 42:24, 1989.

[63] S. Haroche and J. M. Raimond. *Exploring the Quantum: Atoms, Cavities, and Photons*. Oxford University Press, 2006.

[64] J. M. Raimond, M. Brune, and S. Haroche. Manipulating quantum entanglement with atoms and photons in a cavity. *Reviews of Modern Physics*, 73:565, 2001.

[65] H. Walther, B. Varcoe, B. G. Englert, and T. Becker. Cavity quantum electrodynamics. *Reports on Progress in Physics*, 69:1325, 2006.

[66] H. J. Kimble. Strong interactions of single atoms and photons in cavity QED. *Physica Scripta*, 1998:127, 1998.

[67] R. J. Thompson, G. Rempe, and H. J. Kimble. Observation of normal-mode splitting for an atom in an optical cavity. *Physical Review Letters*, 68:1132, 1992.

[68] D. Meschede, H. Walther, and G. Müller. One-atom maser. *Physical Review Letters*, 54:551, 1985.

[69] M. Brune, F. Schmidt-Kaler, A. Maali, J. Dreyer, E. Hagley, J. M. Raimond, and S. Haroche. Quantum rabi oscillation: A direct test of field quantization in a cavity. *Physical Review Letters*, 76:1800, 1996.

[70] A. Blais, R. Huang, A.s Wallraff, S. M. Girvin, and R. J. Schoelkopf. Cavity quantum electrodynamics for superconducting electrical circuits: An architecture for quantum computation. *Physical Review A*, 69:062320, 2004.

[71] R. J. Schoelkopf and S. M. Girvin. Wiring up quantum systems. *Nature*, 451:664, 2008.

[72] A. Wallraff, D. I. Schuster, A. Blais, L. Frunzio, J. Majer, S. Kumar, S. M. Girvin, and R. J. Schoelkopf. Strong coupling of a single photon to a superconducting qubit using circuit quantum electrodynamics. *Nature*, 431:162, 2004.

[73] M. Göppl, A. Fragner, M. Baur, R. Bianchetti, S. Filipp, J. M. Fink, P. J. Leek, G. Puebla, L. Steffen, and A. Wallraff. Coplanar waveguide resonators for circuit quantum electrodynamics. *Journal of Applied Physics*, 104:113904, 2008.

[74] D. M. Pozar. *Microwave Engineering*. Wiley, 2011.

[75] J. Clarke and F. K. Wilhelm. Superconducting quantum bits. *Nature*, 453:1031, 2008.

[76] C. H. van der Wal, A. C. J. ter Haar, F. K. Wilhelm, R. N. Schouten, C. J. P. M. Harmans, T. P. Orlando, S. Lloyd, and J. E. Mooij. Quantum superposition of macroscopic persistent-current states. *Science*, 290:773, 2000.

[77] J. R. Friedman, V. Patel, W. Chen, S. K. Tolpygo, and J. E. Lukens. Quantum superposition of distinct macroscopic states. *Nature*, 406:43, 2000.

[78] J. M. Martinis, S. Nam, J. Aumentado, and C. Urbina. Rabi oscillations in a large josephson-junction qubit. *Physical Review Letters*, 89:117901, 2002.

[79] Y. Nakamura, Yu. A. Pashkin, and J. S. Tsai. Coherent control of macroscopic quantum states in a single-Cooper-pair box. *Nature*, 398:786, 1999.

[80] K. W. Lehnert, K. Bladh, L. F. Spietz, D. Gunnarsson, D. I. Schuster, P. Delsing, and R. J. Schoelkopf. Measurement of the excited-state lifetime of a microelectronic circuit. *Physical Review Letters*, 90:027002, 2003.

[81] Yu. A. Pashkin, O. Astafiev, T. Yamamoto, Y. Nakamura, and J. S. Tsai. Josephson charge qubits: a brief review. *Quantum Information Processing*, 8:55, 2009.

[82] T. Duty, D. Gunnarsson, K. Bladh, and P. Delsing. Coherent dynamics of a josephson charge qubit. *Physical Review B*, 69:140503, 2004.

[83] K. Bladh, T. Duty, D. Gunnarsson, and P. Delsing. The single Cooper-pair box as a charge qubit. *New Journal of Physics*, 7:180, 2005.

[84] M. Büttiker. Zero-current persistent potential drop across small-capacitance josephson junctions. *Physical Review B*, 36:3548, 1987.

[85] V. Bouchiat, D. Vion, P. Joyez, D. Esteve, and M. H. Devoret. Quantum coherence with a single cooper pair. *Physica Scripta*, 1998:165, 1998.

[86] J. Koch, T. M. Yu, J. Gambetta, A. A. Houck, D. I. Schuster, J. Majer, A. Blais, M. H. Devoret, S. M. Girvin, and R. J. Schoelkopf. Charge-insensitive qubit design derived from the cooper pair box. *Physical Review A*, 76:042319, 2007.

[87] V. E. Manucharyan, J. Koch, L. I. Glazman, and M. H. Devoret. Fluxonium: Single cooper-pair circuit free of charge offsets. *Science*, 326:113, 2009.

[88] H. K. Onnes. *Leiden Comm*, 120b,122b,124c, 1911.

[89] M. Tinkham. *Introduction to Superconductivity: Second Edition*. Dover Publications, 2004.

[90] J. Bardeen, L. N. Cooper, and J. R. Schrieffer. Theory of superconductivity. *Physical Review*, 108:1175, 1957.

[91] L. N. Cooper. Bound electron pairs in a degenerate fermi gas. *Physical Review*, 104:1189, 1956.

[92] B. D. Josephson. Possible new effects in superconductive tunnelling. *Physics Letters*, 1:251, 1962.

[93] B. D. Josephson. Coupled superconductors. *Reviews of Modern Physics*, 36:216, 1964.

[94] T. Van Duzer. *Principles of Superconductive Devices and Circuits (2nd Edition)*. Prentice Hall, 1998.

[95] J. Q. You and F. Nori. Atomic physics and quantum optics using superconducting circuits. *Nature*, 474:589, 2011.

[96] G. Wendin and V. S. Shumeiko. Quantum bits with Josephson junctions. *Low Temperature Physics*, 33:724, 2007.

[97] M. H. Devoret, A. Wallraff, and J. M. Martinis. Superconducting Qubits: A Short Review. 2004.

[98] J. Clarke and A. I. Braginski. *The SQUID Handbook: Fundamentals and Technology of SQUIDs and SQUID Systems, Volume I*. Wiley, 2006.

[99] Y. Makhlin, G. Schön, and A. Shnirman. Quantum-state engineering with josephson-junction devices. *Reviews of Modern Physics*, 73:357, 2001.

[100] A. Zagoskin and A. Blais. Superconducting qubits. *Physics in Canada*, 63:215, 2008.

[101] B. Peropadre, J. Lindkvist, I.C. Hoi, C. M. Wilson, J. J. Garcia-Ripoll, P. Delsing, and G. Johansson. Scattering of coherent states on a single artificial atom. *New Journal of Physics*, 15:035009, 2013.

[102] O. Astafiev, A. M. Zagoskin, A. A. Abdumalikov, Yu. A. Pashkin, T. Yamamoto, K. Inomata, Y. Nakamura, and J. S. Tsai. Resonance fluorescence of a single artificial atom. *Science*, 327:840, 2010.

[103] I.-C. Hoi, C. M. Wilson, G. Johansson, J. Lindkvist, B. Peropadre, T. Palomaki, and P. Delsing. Microwave quantum optics with an artificial atom in one-dimensional open space. *New Journal of Physics*, 15:025011, 2013.

[104] I.-C. Hoi, C. M. Wilson, G. Johansson, T. Palomaki, B. Peropadre, and P. Delsing. Demonstration of a single-photon router in the microwave regime. *Physical Review Letters*, 107:073601, 2011.

[105] I. C. Hoi, J. Palomaki, T.and Lindkvist, G. Johansson, P. Delsing, and C. M. Wilson. Generation of nonclassical microwave states using an artificial atom in 1d open space. *Physical Review Letters*, 108:263601, 2012.

[106] I.-C. Hoi, A. F. Kockum, T. Palomaki, T. M. Stace, B. Fan, L. Tornberg, S. R. Sathyamoorthy, G. Johansson, P. Delsing, and C. M. Wilson. Giant cross-kerr effect for propagating microwaves induced by an artificial atom. *Physical Review Letters*, 111:053601, 2013.

[107] P. W. Milonni. *The Quantum Vacuum: An Introduction to Quantum Electrodynamics*. Academic Press, 1993.

[108] W. E. Lamb and R. C. Retherford. Fine structure of the hydrogen atom by a microwave method. *Physical Review*, 72:241, 1947.

[109] H. A. Bethe. The electromagnetic shift of energy levels. *Physical Review*, 72:339, 1947.

[110] C. Gerry and P. Knight. *Introductory Quantum Optics*. Cambridge University Press, 2004.

[111] M. O. Scully and M. S. Zubairy. *Quantum Optics*. Cambridge University Press, 1997.

[112] H. B. G. Casimir. On the attraction between two perfectly conducting plates. *Proceedings of the Royal Netherlands Academy of Arts and Sciences*, 51:793, 1948.

[113] A. Fragner, M. Göppl, J. M. Fink, M. Baur, R. Bianchetti, P. J. Leek, A. Blais, and A. Wallraff. Resolving vacuum fluctuations in an electrical circuit by measuring the lamb shift. *Science*, 322:1357, 2008.

[114] K. A. Milton. *The Casimir Effect: Physical Manifestations of Zero-point Energy*. World Scientific Publishing Co Pte Ltd, 2001.

[115] U. Mohideen and A. Roy. Precision measurement of the casimir force from 0.1 to 0.9 μm. *Physical Review Letters*, 81:4549, 1998.

[116] S. K. Lamoreaux. Demonstration of the casimir force in the 0.6 to 6μm range. *Physical Review Letters*, 78:5, 1997.

[117] C. Denardo, J. Puda, and A. Larraza. A water wave analog of the casimir effect. *American Journal of Physics*, 77, 2009.

[118] G. Barton and C. Eberlein. On quantum radiation from a moving body with finite refractive index. *Annals of Physics*, 227:222, 1993.

[119] M. Dykman. *Fluctuating Nonlinear Oscillators: From Nanomechanics to Quantum Superconducting Circuits*. Oxford University Press, 2012.

[120] A. Lambrecht, M. Jaekel, and S. Reynaud. Motion induced radiation from a vibrating cavity. *Physical Review Letters*, 77:615, 1996.

[121] M. Crocce, D. A. R. Dalvit, F. C. Lombardo, and F. D. Mazzitelli. Model for resonant photon creation in a cavity with time-dependent conductivity. *Physical Review A*, 70:033811, 2004.

[122] C. Braggio, G. Bressi, G. Carugno, C. Del Noce, G. Galeazzi, A. Lombardi, A. Palmieri, G. Ruoso, and D. Zanello. A novel experimental approach for the detection of the dynamical casimir effect. *Europhysics Letters*, 70:754, 2005.

[123] E. Yablonovitch. Accelerating reference frame for electromagnetic waves in a rapidly growing plasma: Unruh-davies-fulling-dewitt radiation and the nonadiabatic casimir effect. *Physical Review Letters*, 62:1742, 1989.

[124] S. De Liberato, D. Gerace, I. Carusotto, and C. Ciuti. Extracavity quantum vacuum radiation from a single qubit. *Physical Review A*, 80:053810, 2009.

[125] J. R. Johansson, G. Johansson, C. M. Wilson, and F. Nori. Dynamical casimir effect in a superconducting coplanar waveguide. *Physical Review Letters*, 103:147003, 2009.

[126] J. R. Johansson, G. Johansson, C. M. Wilson, and F. Nori. Dynamical casimir effect in superconducting microwave circuits. *Physical Review A*, 82:052509, 2010.

[127] D. Bozyigit, C. Lang, L. Steffen, J. M. Fink, C. Eichler, M. Baur, R. Bianchetti, P. J. Leek, S. Filipp, M. P. da Silva, A. Blais, and A. Wallraff. Antibunching of microwave-frequency photons observed in correlation measurements using linear detectors. *Nature Physics*, 7:154, 2010.

[128] R. Al Maruf. *Master thesis: Studies the Effect of Electron Beam Lithography on Charge Noise*. Chalmers University of Technology, 2013.

[129] S. Nik. *PhD thesis: The Functional Microstructure of Al/AlOx/Al Tunnel Junctions*. Chalmers University of Technology, 2013.

[130] G. J. Dolan. Offset masks for lift-off photoprocessing. *Applied Physics Letters*, 31:337, 1977.

[131]

[132] T. Greibe, M. P. V. Stenberg, C. M. Wilson, T. Bauch, V. S. Shumeiko, and P. Delsing. Are "pinholes" the cause of excess current in superconducting tunnel junctions? a study of andreev current in highly resistive junctions. *Physical Review Letters*, 106:097001, 2011.

[133] J. M. Martinis, M. H. Devoret, and J. Clarke. Experimental tests for the quantum behavior of a macroscopic degree of freedom: The phase difference across a josephson junction. *Physical Review B*, 35:4682, 1987.

[134] K. Bladh, D. Gunnarsson, E. Hurfeld, S. Devi, C. Kristoffersson, B. Smålander, S. Pehrson, T. Claeson, P. Delsing, and M. Taslakov. Comparison of cryogenic filters for use in single electronics experiments. *Review of Scientific Instruments*, 74:1323, 2003.

[135] J. Lublin. *Master thesis: Studies the Effect of Electron Beam Lithography on Charge Noise*. Chalmers University of Technology, 2013.

[136] L. Spietz, K. W. Lehnert, I. Siddiqi, and R. J. Schoelkopf. Primary electronic thermometry using the shot noise of a tunnel junction. *Science*, 300:1929, 2003.

[137] H. Wolf, F.J. Ahlers, J. Niemeyer, H. Scherer, T. Weimann, A.B. Zorin, V.A. Krupenin, S.V. Lotkhov, and D.E. Presnov. Investigation of the offset charge noise in single electron tunneling devices. *IEEE Transactions Instrumentation Measurement*, 46:303, 1997.

[138] B. Starmark, T. Henning, T. Claeson, P. Delsing, and A. N. Korotkov. Gain dependence of the noise in the single electron transistor. *Journal of Applied Physics*, 86:2132, 1999.

[139] R. L. Kautz, G. Zimmerli, and J. M. Martinis. Self-heating in the Coulomb-blockade electrometer. *Journal of Applied Physics*, 73:2386, 1993.

[140] S. M. Verbrugh, M. L. Benhamadi, E. H. Visscher, and J. E. Mooij. Optimization of island size in single electron tunneling devices: Experiment and theory. *Journal of Applied Physics*, 78:2830, 1995.

[141] M. Meschke, J. P. Pekola, F. Gay, R. E. Rapp, and H. Godfrin. Electron thermalization in metallic islands probed by coulomb blockade thermometry. *Journal of Low Temperature Physics*, 134:1119, 2004.

[142] A. M. Savin, J. P. Pekola, D. V. Averin, and V. K. Semenov. Thermal budget of superconducting digital circuits at subkelvin temperatures. *Journal of Applied Physics*, 99:084501, 2006.

[143] J. M. Underwood, P. J. Lowell, Galen C. ÓNeil, and J. N. Ullom. Insensitivity of sub-kelvin electron-phonon coupling to substrate properties. *Physical Review Letters*, 107:255504, 2011.

[144] F. C. Wellstood, C. Urbina, and J. Clarke. Hot-electron effects in metals. *Physical Review B*, 49:5942, 1994.

[145] D.V. Averin and K.K. Likharev. In B.L. Altshuler, P.A. Lee, and R.A. Webb, editors, *Mesoscopic Phenomena in Solids*, page 173. North-Holland, Amsterdam, 1991.

[146] M. Gustafsson. *PhD thesis: Studies of acoustic waves, noise and charge pumping using single-electron devices*. Chalmers University of Technology, 2012.

[147] R. O. Pohl, X. Liu, and E. Thompson. Low-temperature thermal conductivity and acoustic attenuation in amorphous solids. *Reviews of Modern Physics*, 74:991, 2002.

[148] G. S. Kumar, J. W. Vandersande, T. Klitsner, R. O. Pohl, and G. A. Slack. Low-temperature heat transport by charge carriers in doped semiconductors. *Physical Review B*, 31:2157, 1985.

[149] S. G. Louie and M. L. Cohen. Electronic structure of a metal-semiconductor interface. *Physical Review B*, 13:2461, 1976.

[150] M. Kiguchi and K. Saiki. *e-Journal of Surface Science and Nanotechnology*, 2:191, 2004.

[151] S. K. Choi, D. Lee, S. G. Louie, and J. Clarke. Localization of metal-induced gap states at the metal-insulator interface: Origin of flux noise in squids and superconducting qubits. *Physical Review Letters*, 103:197001, 2009.

[152] L. J. Zeng, T. Greibe, S. Nik, C. M. Wilson, P. Delsing, and E. Olsson. Nanoscale interaction layer at the interface between al films and SiO_2 substrates of Al/AlOx/Al josephson tunnel junctions. *Journal of Applied Physics*, 113:143905, 2013.

[153] K. Koshino and Y. Nakamura. Control of the radiative level shift and linewidth of a superconducting artificial atom through a variable boundary condition. *New Journal of Physics*, 14:043005, 2012.

[154] A. A. Clerk, M. H. Devoret, S. M. Girvin, F. Marquardt, and R. J. Schoelkopf. Introduction to quantum noise, measurement, and amplification. *Reviews of Modern Physics*, 82:1155, 2010.

[155] A. F. van Loo, A. Fedorov, K. Lalumière, B. C. Sanders, A. Blais, and A. Wallraff. Photon-mediated interactions between distant artificial atoms. *Science*, 342:1494, 2013.

[156] I.-C. Hoi, A. F. Kockum, T. Palomaki, T. M. Stace, B. Fan, L. Tornberg, S. R. Sathyamoorthy, G. Johansson, P. Delsing, and C. M. Wilson. Giant cross-kerr effect for propagating microwaves induced by an artificial atom. *Physical Review Letters*, 111:053601, 2013.